

**POLITECNICO DI TORINO**  
**Area dell'Ingegneria**  
**Corso di Laurea Magistrale in Ingegneria Meccanica**

**Tesi di Laurea Magistrale**

**"COMBUSTION AND EXHAUST-TEMPERATURE  
CHARACTERIZATION IN A HD NG ENGINE BY MEANS OF A  
FRACTAL-BASED MODEL"**



**Relatori: Prof. Daniela Misul**  
**Prof. Mirko Baratta**

**Candidato:**  
**Laura Muscedra**

**Aprile 2018**

# Acknowledgements

---

A special thank to the Doctor of Philosophy Yifei Tong, who wisely has guided me through the science of modelization and the implementation of theory in computational tools. Remarkable patience and prompt carefulness have been shown to my uncertain trials and steady achievements until the experiments completion.

# Index

---

|  |              |
|--|--------------|
| Acknowledgements.....  | p.1          |
| Index.....   | p.2          |
| Abstract.....  | p.3          |
| <b>1. Introduction</b> .....   | <b>p.4</b>   |
| 1.1 European public transport bus services overview.....             | p.4          |
| 1.2 Heavy-duty engines features.....                                 | p.6          |
| 1.3 Contemporary research on HD engines: CNG.....                    | p.10         |
| 1.4 Variable Valve Actuation(VVA) in HD engines.....                 | p.14         |
| 1.5 CNG combustion strategies in HD engines .....                    | p.18         |
| 1.6 HD CNG engine aftertreatment systems.....                        | p.20         |
| 1.6 CNG engine alternative ignition systems.....                     | p.24         |
| <b>2. Reference engine</b> .....                                     | <b>p.26</b>  |
| 2.1 GT-Power software.....   | p.27         |
| 2.2 GT-Power tested engine model.....                                | p.29         |
| <b>3. Predictive engine combustion model</b> .....                   | <b>p.35</b>  |
| 3.1 In-cylinder gases thermodynamic state.....                       | p.35         |
| 3.2 Burned mass fraction evolution.....                              | p.37         |
| 3.3 In-cylinder turbulence model.....                                | p.37         |
| 3.4 Turbulent flame speed model.....                                 | p.40         |
| 3.5 Laminar flame speed submodel.....                                | p.42         |
| 3.6 Flame kernel growth.....   | p.42         |
| 3.7 Combustion termination phase.....                                | p.43         |
| <b>4. Numerical engine combustion model calibration.</b> .....       | <b>p.44</b>  |
| 4.1 Calibration first phase (simulation phase).....                  | p.45         |
| 4.2 Calibration second phase(correlation phase).....                 | p.58         |
| <b>5. Numerical prediction for exhaust temperature control</b> ..... | <b>p.70</b>  |
| 5.1 CORE Collaborative Project.....                                  | p.70         |
| 5.2 Numerical prediction for exhaust temperature control.....        | p.71         |
| 5.3 Results for other HD NG engines for combustion retardation.....  | p.75         |
| <b>6. Conclusions</b> .....  | <b>p.80</b>  |
| <b>7. Bibliography</b> .....   | <b>p.82</b>  |
| <b>8. Annex A</b> .....  | <b>p.86</b>  |
| <b>9. Annex B</b> .....  | <b>p.102</b> |

# Abstract

---

The present thesis is concerned with the investigation of advanced concepts for internal combustion engine design related to combustion modelization via numerical simulation; the analysis is accomplished on a heavy-duty engine fuelled by Compressed Natural Gas (CNG).

Heavy duty engines featured by singular own parameters are correlated to contemporary research efforts regarding alternative fuels (CNG), Variable Valve Actuation (VVA), specific innovative combustion concepts related to dedicated aftertreatment systems and alternative ignition strategies .

Cursor 8, name of the tested engine, has been carefully reproduced into GT-Power computational model. The software has allowed to integrate into the virtual project a dedicated novel predictive combustion model based on laminar flamelets concept. According to this assumption, turbulent burning velocity can be derived from the wrinkled flamelets surface area. The fractal geometry concept has been adopted to describe the flamelets surface. Model calibration has followed the theoretical definition.

Applying dedicated strategy, combustion management has been implemented related to EIVC actuation in order to enhance aftertreatment system conversion efficiency.

# 1. Introduction

---

The present work is mainly focused on a heavy-duty vehicle CNG engine intended for public transport with urban buses produced by IVECO and FIAT Powertrain Technologies FPT, manufactured in Italy. Widest CNG Iveco Bus is Urbanway Bus, which reaches the length of 18m and it has a technically permissible maximum laden mass of 30000kg (three axes vehicle). It is designed for up to 51 passengers and it is illustrated in Figure 1[1]. In Italy urban buses are classified as International Category M3[2].



*Figure 1. IVECO Urbanway bus, 18 m length.[1]*

## 1.1 European public transport bus services overview

Passenger transport on land in Europe is made for about 9.2% by buses and coaches(2017)[3]; this mobility share has quite increased from 2011 when it was about 7.8%[4].Today circulating buses in Europe are more than 800000 and they are average aged 9 years[3].In Figure 2 it is reported the passenger transport share in EU28 in 2013, with the reference to passenger-kms in % [5].

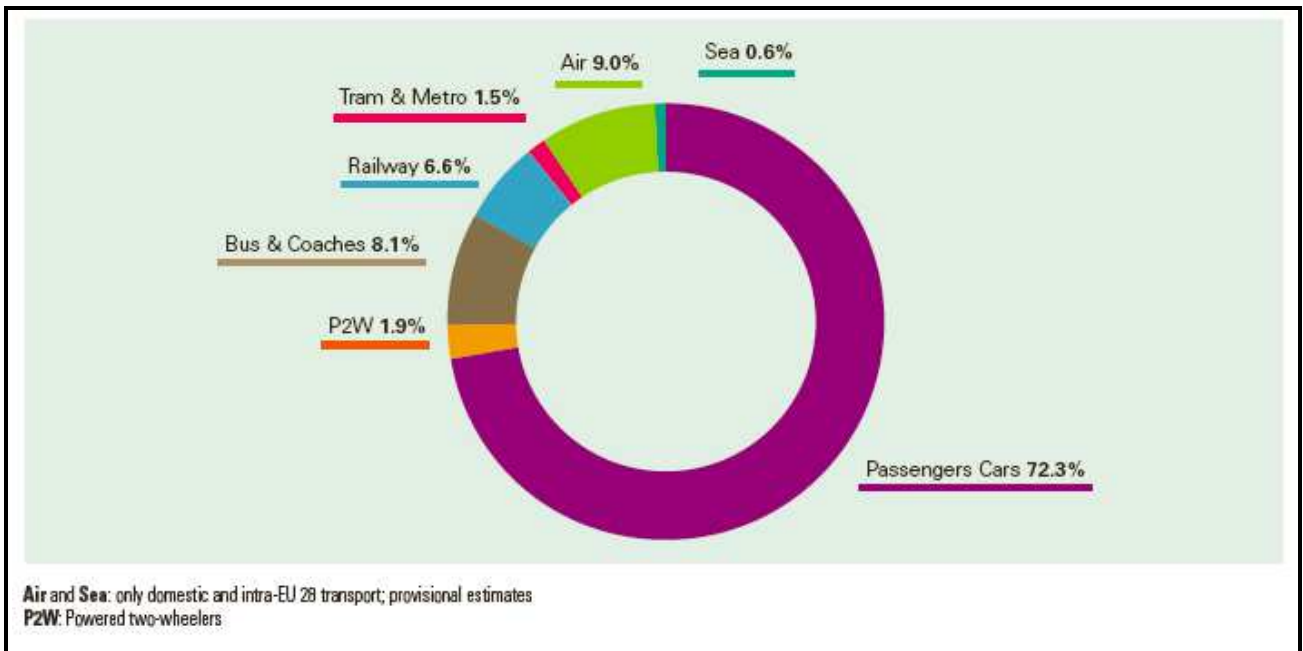


Figure 2. Passenger transport modal split in EU 28, 2013, source:EC [6]

European buses running on alternative fuels are about 20% of the total fleet[6]. The typical layout of vehicle CNG powertrain is shown in Figure 3[4]; the European CNG filling stations widespread in 2016 is reported in Figure 4[7].

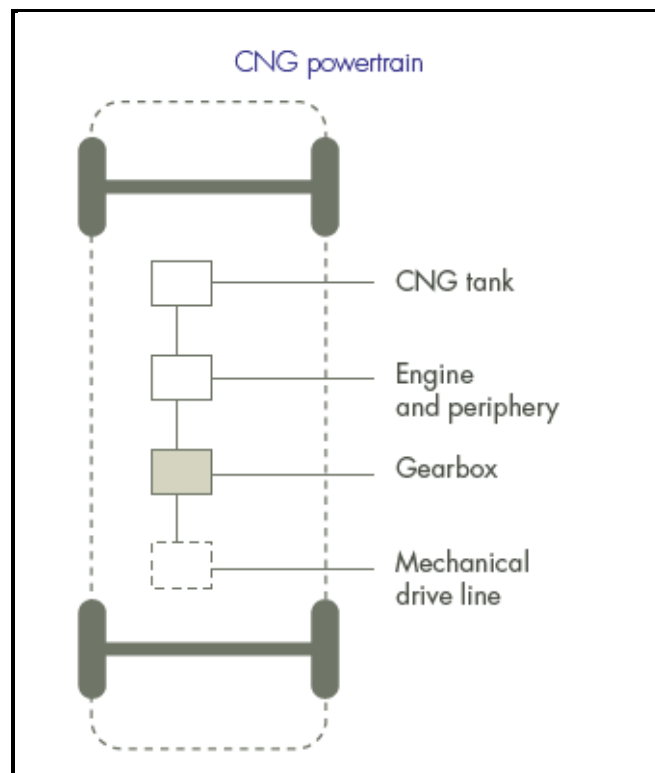


Figure 3. CNG powertrain layout for urban buses.[4]

Some facts about the CNG / LNG infrastructure in Europe

|   |                |  |  |
|---|----------------|--|---|
|  | Austria        | 173  | 0   |
|  | Belgium        | 55   | 2   |
|  | Bulgaria       | 105  | 0   |
|  | Czech Republic | 108  | 0   |
|  | France         | 43   | 2   |
|  | Germany        | 913  | 1   |
|  | Italy          | 1101   | 3   |
|  | Netherlands    | 147  | 17  |
|  | Spain          | 45   | 17  |
|  | Sweden         | 163  | 6   |
|  | Switzerland    | 136  | 1   |
|  | U.K.           | 8  | 9   |

Public stations

Figure 4. 2016 European CNG/LNG filling stations widespread.[7]

## 1.2 Heavy-duty engines features

Heavy-duty engine refers to any engine used for (or which the engine manufacturer could reasonably expect to be used for) motive power in a heavy-duty vehicle[8].

Main characteristics of heavy-duty vehicles can be compared with the corresponding ones of light-duty transportations. Referring to their applications, heavy-duty solutions are intended to allow the owner in performing a business or a specific dedicated task, while light-duty vehicles are purchased to help the driver and passengers to reach a destination[9]. Due to job application-specific motivation in heavy-duty vehicles, designers search for a solution as efficient as possible with the lowest total cost of ownership; then fuel consumption becomes a determining factor in the project and purchase decision. In Table 1 further comparison between light-duty and heavy-duty vehicles is reported[9].

|  | Light-Duty Vehicles   | Heavy-Duty Vehicles   |
|--|---|---|
| <b>Application or Use</b>  | Consumer goods typically purchased for delivering the driver and passengers to a destination.                               | Capital goods to help owner conduct business or perform a specific, dedicated task. Designed for application-specific uses to conduct a job as efficiently as possible with the lowest total cost of ownership. |
| <b>Purchase Decision</b>   | Influenced by a range of variables other than cost, such as interior passenger and cargo volume index and personal choice.* | Cost trade-offs explicitly considered. Fuel economy tends to be a major determining factor.   |
| <b>Vehicle Turnover</b>  | Analysis of AEO vehicle survival as a function of age indicates the average lifetime of cars and light trucks is 17 years.† | Sophisticated, first owner fleets turn over vehicles twice as fast as light-duty automotive, with Class 8 long haul turning over in about 3 years.†   |
| <b>Lifetime Fuel Cost</b>  | Lifetime fuel cost for an average passenger car is similar to the vehicle's original purchase price.†                       | Fuel cost is typically the second highest operating cost, which provides an incentive to increase fuel economy. Lifetime fuel costs are nearly five times that of the original purchase price of the vehicle.†  |
| <b>Fuel</b>  | Majority powered by gasoline.   | Majority powered by diesel.   |
| <small>* The interior volume index ranges from 85 to 160 cubic feet.<br/> † U.S. Department of Energy, <i>Research and Development Opportunities for Heavy Trucks</i>, June 2009, <a href="http://www1.eere.energy.gov/vehiclesandfuels/pdfs/truck_efficiency_paper_v2.pdf">http://www1.eere.energy.gov/vehiclesandfuels/pdfs/truck_efficiency_paper_v2.pdf</a>.</small> |   |   |

Table 1. Comparison between light-duty and heavy-duty vehicles[9].

Heavy duty engines exhibit singular values of geometrical variables and they show unique functional features. In fact they are characterized by large displacements and high reciprocating masses values with respect to light-duty ones.

In order to make a comparison between two identical engines which only differ in size, one can denote as  $s$  their scale ratio. It can be shown that the gas velocity  $w'$  in the minimum flow area at the inlet valve of the bigger engine is  $s$  times the velocity  $w$  in the smaller one. Then the volumetric efficiency  $\lambda_v'$  of the heavy-duty engine is lower than  $\lambda_v$  of the light-duty one[10].

Besides, equal other conditions (temperature, pressure, turbulence, air-to-fuel ratio) and by supposing in first approximation that combustion velocity is independent from cylinder bore, it results that for the heavy-duty engine the combustion duration is  $s$  times the duration of the light-duty one. This fact is due to the longer path the flame has to go through. As a consequence, the rotational engine speed for heavy-duty engines is lower than for light-duty ones[10].

The mean piston speed value is low also because of its relation with resistance to gas flow into the engine or stresses due to the inertia of the moving parts (reciprocating masses)[11].

In fact in both heavy duty diesel engines and CNG ones, the structure is more robust and this fact makes reciprocating masses value higher than light duty ones. Such robustness is due to the high in-cylinder pressures reached during combustion (up to 200 bar)[12,13], which have to be faced by the cylinder structure. Therefore, if in heavy duty engines masses are relatively important, their mean piston speed is limited to a lower value than in light-duty ones[12]. Moreover, the shaft speed is kept moderate in order to contain the cyclic loads acting over main bearings and to reduce noise [10]. As a consequence, the specific power output expressed by the ratio between output power  $P_u$  and total engine displacement  $V_{tot}$  is quite low.

Referring to heavy-duty engine fuel economy, the wider engine dimensions with respect to light-duty engines have the great consequence that a higher amount of available chemical energy is disposed in friction losses. In fact the fuel energy is only partially converted into useful work; about 30% of the energy is lost in exhaust gases enthalpy, while about 20% is transferred to the cooling system. The remaining energy (about 50%) is available for mechanical work. In order to move the vehicle it is necessary to overcome the rolling resistance and the air drag and in addition you must also provide the acceleration power, but the energy available for the vehicle propulsion is only about 34% of the total energy, because about 16% is disposed in auxiliaries operation, internal engine and transmission friction. Based on average values, the total engine energy losses are summarized in Figure 5[14].

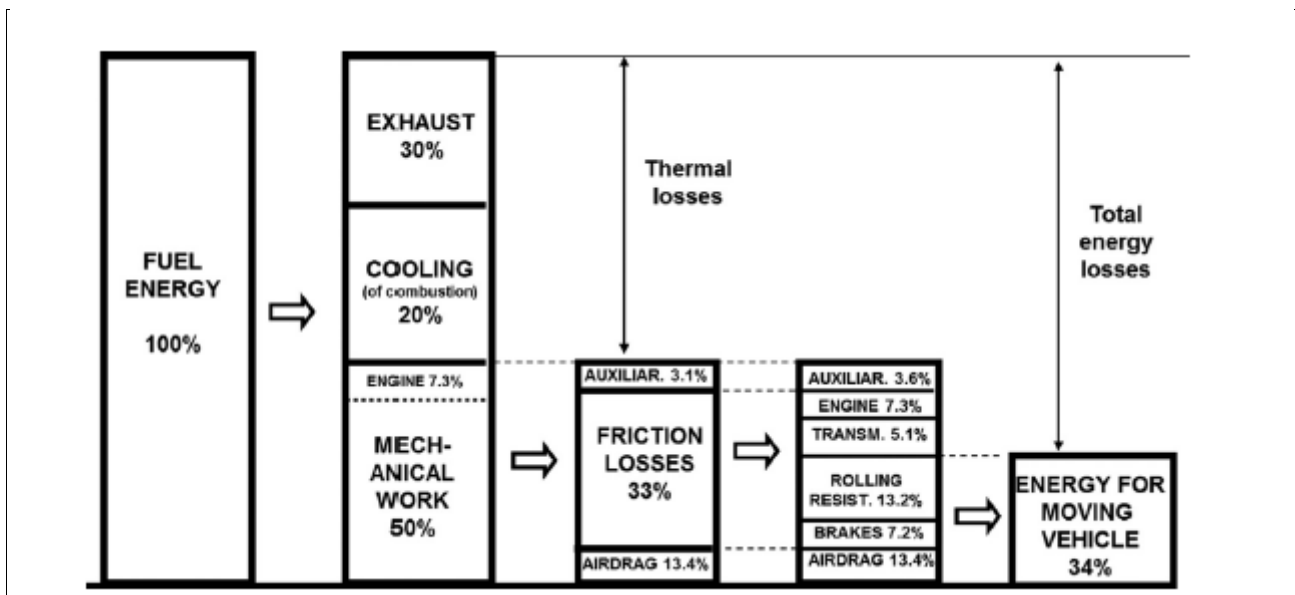


Figure 5. Breakdown of the average energy consumption in heavy duty vehicles based on average values from various categories of trucks and buses[14]

The relations between this types of energy losses can vary significantly, depending on how the vehicle is operated[14]. Actually, in the highly transient low-speed operation

of city buses, the energy necessary to accelerate the vehicle dominates the energy use and most of the kinetic energy accumulated in the vehicle during the acceleration is lost by conversion in thermal energy by brakes.

The internal engine friction losses can be divided into piston assembly losses (45%), bearings and seals (30%, with hydrodynamic lubrication), valve train (15%, with mixed lubrication), pumping and hydraulic viscous losses (10%). Referring to transmission friction, a urban bus is usually equipped with an automatic gearbox with planetary gears and torque converter; for them the efficiency ranges between 90% to 95% under optimal conditions of operation. Regarding auxiliaries losses, they are mainly due to cooling fan of the radiator, air compressor of the pneumatic system, air-condition compressor, hydraulic oil pump for the power steering[14].

In heavy duty vehicles the aerodynamic drag and the rolling resistance are the major sources of energy losses. Referring to air drag, the projected frontal area and the drag coefficient  $C_D$  linearly influence the aerodynamic resistance; for urban buses the average frontal area is about  $7m^2$  and the drag coefficient ranges from 0.58 to 0.66[14]. With reference to rolling resistance, it depends linearly from the vehicle weight and the coefficient of tire rolling friction  $\mu$ , which under usual non optimized conditions is about 0.01[14].

In detail referring to urban buses, due to multiple stop-start situations their friction losses are the highest among other heavy duty vehicles, as it is shown in Figure 6[14].

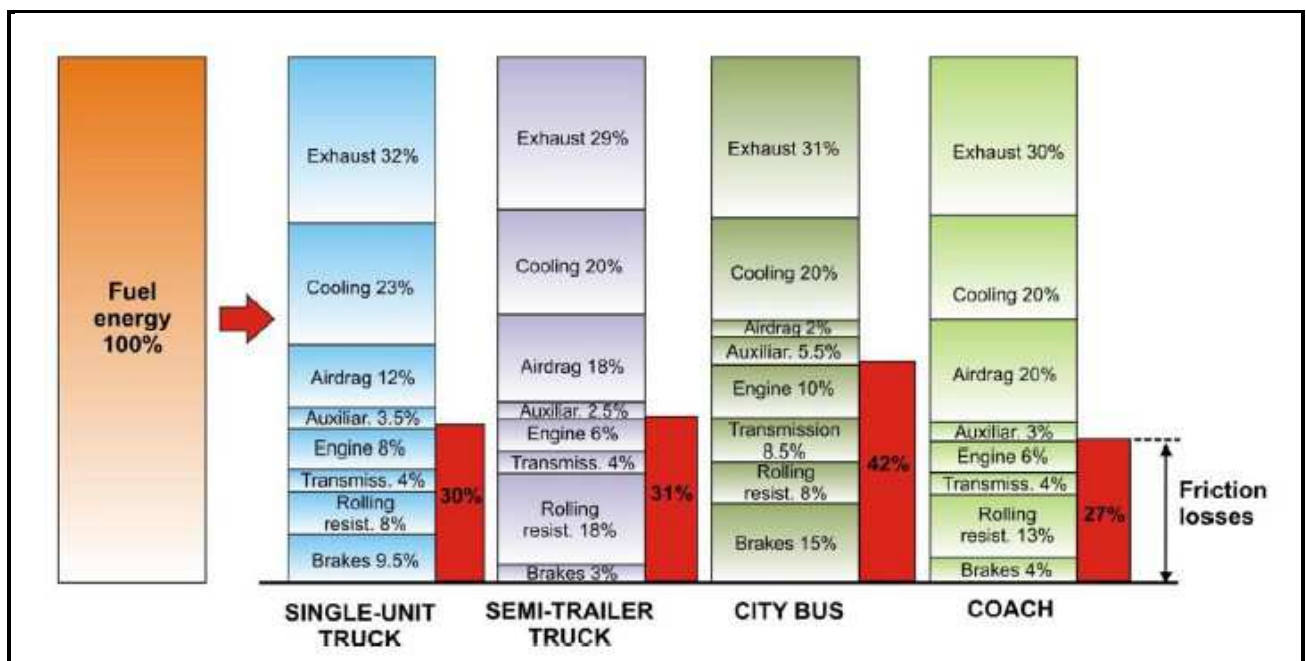


Figure 6. Breakdown of the global energy average consumption in detail for heavy duty vehicles[14]

Moreover, referring to the necessity of multiple gears shifts, in urban buses engines it is required brake torque trend in function of engine speed quite flat for a wide range of speeds[15]. In particular one can define the *Torque Rise* as:

$$Torque\ Rise = \frac{Peak\ Torque - Rated\ Torque}{Rated\ Torque} \cdot 100 \quad (1)$$

where *Rated Torque* is related to brake torque produced at rated speed[15]; in urban buses a low torque rise is ideal. In Figure 7 the comparison between engine performance curves with high and low torque rise is shown.

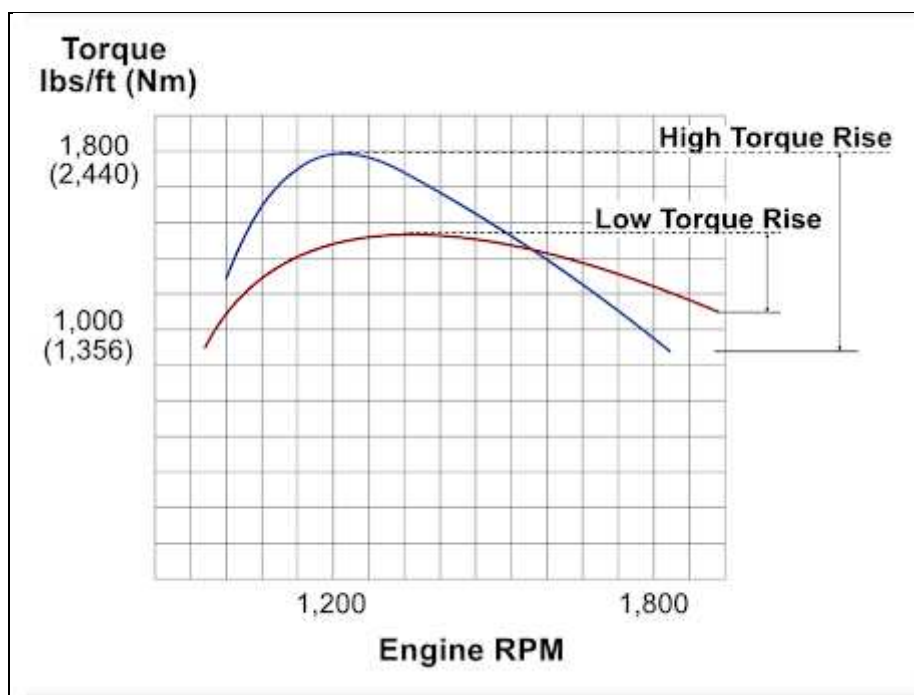


Figure 7. Engine high and low torque rise trends[15].

### 1.3 Contemporary research on HD engines:CNG

An overall sustainable alternative to conventional fuels, namely gasoline and diesel fuel, has been proved to be the Natural Gas (NG), which is a large available form of fossil energy, thus non-renewable one, produced by gas wells or in conjunction with the crude-oil derivation[16,17]. It can be used as a fuel essentially in the form in which it is extracted, although some processing is carried out before the gas is distributed. Referring to gas supply network, NG has the advantage that a comprehensive distribution system is already in place for residential and commercial uses, thus substantially reducing the cost of adopting it as an alternative fuel.

However, the refueling infrastructure still needs to be established [17,18]. In Table 2, it is reported the Natural Gas composition [19].

| Composition    | Formula                                     | Typical Analysis [mole %] | Range [mole %] |
|----------------|---|---------------------------|----------------|
| Methane        | CH <sub>4</sub>                             | 93.9                      | 87.0 ÷ 97.0    |
| Ethane         | C <sub>2</sub> H <sub>6</sub>               | 4.2                       | 1.5 ÷ 9        |
| Propane        | C <sub>3</sub> H <sub>8</sub>               | 0.3                       | 0.1 ÷ 1.5      |
| iso-Butane     | i-C <sub>4</sub> H <sub>10</sub>            | 0.03                      | 0.01 ÷ 0.3     |
| normal-Butane  | n-C <sub>4</sub> H <sub>10</sub>            | 0.03                      | 0.01 ÷ 0.3     |
| iso-Pentane    | i-C <sub>5</sub> H <sub>12</sub>            | 0.01                      | trace ÷ 0.04   |
| normal-Pentane | n-C <sub>5</sub> H <sub>12</sub>            | 0.01                      | trace ÷ 0.04   |
| Hexanes plus   | C <sub>6</sub> H <sub>14</sub> <sup>+</sup> | 0.01                      | trace ÷ 0.06   |
| Nitrogen       | N <sub>2</sub>                              | 1                         | 0.2 ÷ 5.5      |
| Carbon Dioxide | CO <sub>2</sub>                             | 0.5                       | 0.05 ÷ 1       |
| Oxygen         | O <sub>2</sub>                              | 0.01                      | trace ÷ 0.1    |
| Hydrogen       | H <sub>2</sub>                              | trace                     | trace ÷ 0.02   |

Table 2. Natural Gas composition [19,20]

Natural Gas can be compressed and it can be stored and used as Compressed Natural Gas (CNG); it requires the use of very high pressure on about 200 bar (20 MPa), because of its low energy density at atmospheric pressure and room temperature.

The legal maximum operative pressure for a vehicle storage cylinder is 260 bar according to ISO11439, with a nominal pressure of 200 bar at 15°C and a maximum CNG temperature at the end of refueling of 65°C. Cylinders are tested before installation to a pressure of 300 bar; they can tolerate pressures up to 730 bar, in the case they are made of glass fibre. An alternative storage method is in liquid form at a temperature of -162°C (LNG, Liquefied Natural Gas) [17,21].

CNG has long been used in stationary engines; in last decades, by the development of lightweight high-pressure storage vessels, CNG application as a transport engines fuel has been considerably advanced [17].

The main CNG advantage over conventional fuels is an environmental benefit; in fact, pollutants emissions are lower with respect to both gasoline and diesel fuel engines. CNG allows non-methane hydrocarbons to be reduced by about 50%, NO<sub>x</sub> by 50÷87%, CO by 70÷95% with respect to a petroleum powered engine. In addition neither particulate matter (PM) or benzene are produced. HC diminishes because CNG is injected in the gaseous form; then, the cylinder wall oil layer doesn't adsorb its molecules. Moreover during the cold start or during periods at low atmospheric temperatures, unburned hydrocarbons quantities don't increase due to the fact that the

charge enrichment is not necessary. Methane and CO emissions reach their peak at light loads. CNG doesn't cause deposits in the combustion chamber and on the spark plug, thus generally extending piston ring and spark plug life[17,22,23].

The methane molecule structure is relatively simple and its H/C ratio is higher than gasoline and diesel fuel molecules (about 4 in comparison to about 1.85); the lower quantity of carbon atoms reduces the amounts of CO<sub>2</sub> of about 20÷ 30% in comparison to petroleum engines. Although the Greenhouse Gases (GHGs) emission in the form of CO<sub>2</sub> diminishes, significant fraction of unburned hydrocarbons is constituted by methane, which has a global warming potential (GWP) 25 times higher than CO<sub>2</sub> as GHG[16,17,22].

From a strategic point of view, the Research Octane Number (RON) of natural gas is high; in fact it reaches about 130. This allows for the realization of high compression ratios up to 16:1 and for the thermal efficiency increment of about 10% with respect to petrol engines. Knocking resistance is less relevant at high loads[17]. CNG provides engine operations in a wide range of air-fuel ratios, working with stoichiometric mixtures as well as with lean or extremely lean ones. Optimum efficiency from natural gas is obtained when burnt in a lean charge with relative air/fuel ratio  $\lambda$  of about 1.3÷1.5, although this leads to a loss in performance. Output power is maximized running on a slightly rich mixture with respect to stoichiometric one[17,22].

In Table 3 main NG characteristics as fuel are reported at 25°C and 1 atm[17].

| <b>NG Properties</b>                    | <b>Value</b>             |
|---|--------------------------|
| Formula                                 | $C_nH_{3.8n}N_{0.1n}$    |
| Density                                 | 0.72 kg/m <sup>3</sup>   |
| Flammability limits(volume % in air)    | 4.3 ÷ 15%                |
| Flammability limits( $\emptyset$ )      | 0.4 ÷ 1.6%               |
| Autoignition temperature in air         | 723 °C                   |
| Minimum ignition energy                 | 0.28 mJ                  |
| Flame velocity                          | 0.38 m/s                 |
| Adiabatic flame temperature             | 2214 K                   |
| Quenching distance                      | 2.1 mm                   |
| Stoichiometric air/fuel mass ratio      | 14.5                     |
| Stoichiometric fuel/air volume fraction | 9.48 %                   |
| Lower Heating Value                     | 45.8 MJ/kg               |
| Heat of combustion                      | 2.9 MJ/kg <sub>air</sub> |

Table 3. NG fuel characteristics [11,17].

NG is lighter than air and in case of a rupture it will dissipate upward rapidly avoiding the danger of fire; therefore it is safer than gasoline and diesel fuel that

would pool on the ground. Moreover NG ignition in the vehicle surroundings is unlikely because its flammability concentration in air is between 5% and 15%[17]. From an economical point of view, CNG prices are more stable than petroleum ones, as shown in Figure 8, in which the fuels costs per GGE (Gasoline Gallon Equivalent) are reported from 2000 to 2016 for diesel fuel, gasoline, CNG and other alternative fuels in U.S[24]. It can also be noted that CNG is cheaper than conventional fuels.

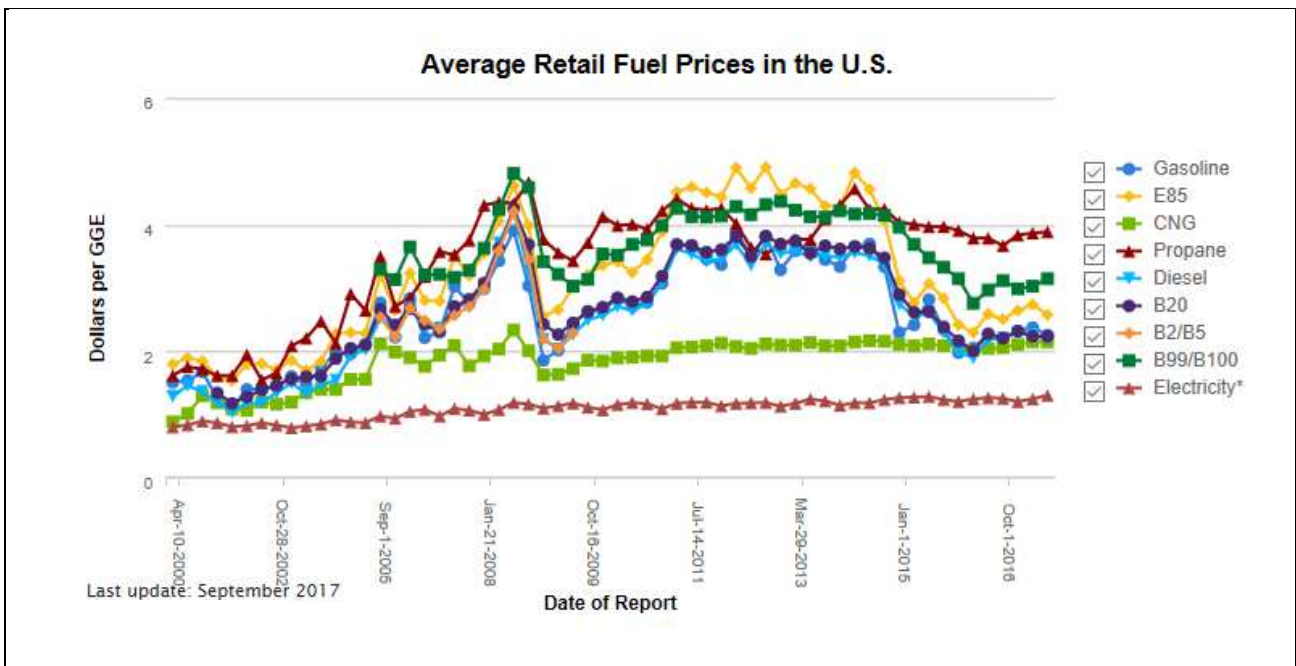


Figure 8. Conventional fuels and CNG costs comparison in the period 2000-2016 [24].

Among primary CNG disadvantages, it can be noticed that it has lower energy density with respect to gasoline and diesel fuel. Moreover the volumetric efficiency of CNG engine is diminished in comparison to conventional fuel engines, because NG is in the gaseous form; in detail, the induced airflow is reduced by about 10% being replaced by fuel gas[17,25]. As a drawback, NG provides less lubrication in comparison to gasoline and diesel fuels that are in the liquid form; thus, the CNG engine friction torque is higher than conventional fuel engines[25].

Therefore CNG engine performance is lower in brake power and mean effective pressure if compared to gasoline and diesel engines[25].

Further, CNG vehicle refuelling is a slow process and it is necessary two or three times as often as a similar petrol or diesel-fuelled vehicle, because of the limited capacity of on-board CNG storage system[17].

In order to overcome CNG penalties, it can be worth of notice to study the possibility of supercharging or turbocharging and to enhance the charge motion by

turbulent effects, as illustrated in Figure 9, which lists ideal NG engine operating conditions[25].

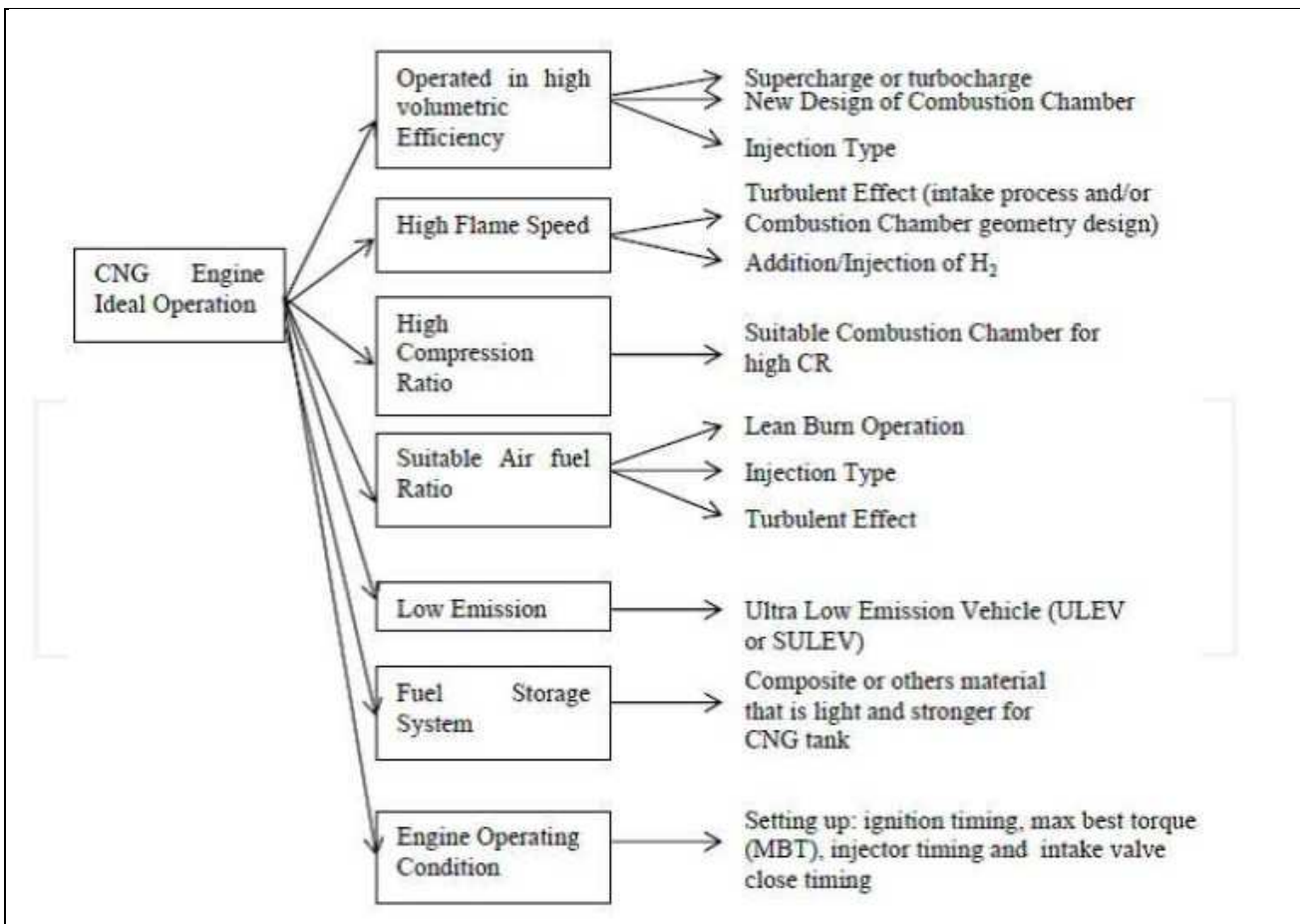


Figure 9. Ideal NG engine operating conditions [25]

## 1.4 Variable Valve Actuation (VVA) in HD engines

Variable Valve Actuation (VVA) refers to a range of technologies which add flexibility to engine valve's train; they enable variable valve event timing, duration and/or lift [26]. Then, they avoid the restrictions created by a fixed valve timing and lift[27].

VVA systems can be divided into camshaft based and camless ones[26]. Moreover a distinction can be made between actuations which adjust valve event timing (phase adjustment) and those which enable variable valve lift [28]. BMW's Vanos is an example of phase adjustment unit which operates in continuous actuation, while Honda's VTEC unit represents a solution which enables cam switching with discrete variation in valve lift [28,29]. Continuous actuation in valve lift change is mechanically operated by BMW's Valvetronic, while Uniair/Multiair units enable

fully-variable valve lift by electrohydraulic system. In Figure 10 main valve trains classification is shown; in Figure 11 a selection of developed VVA systems is reported [28,29].

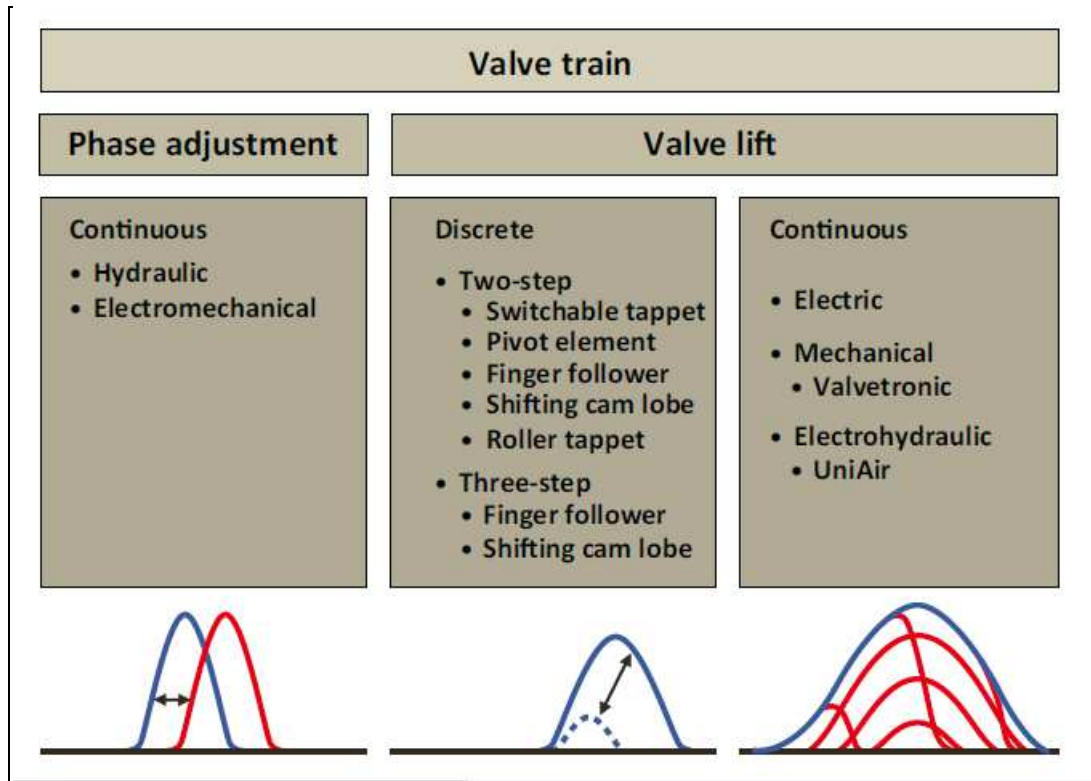


Figure 10. Valve train variability and main classification [28].

| Fully-variable valve train systems |                        |  |   |
|------------------------------------|------------------------|--|---|
| Development                        | Mechanical systems     | 3D cam   | Electro-hydraulic   |
|                                    |                        | INA Eco Valve<br>Toyota Valvematic<br>Nissan VVEL<br>Hilite Univalve<br>BMW Valvetronic II<br>Mahle VLD<br>Meta VVH<br>Presta DeltaValveControl<br>Delphi VVA<br>Mitsubishi MIVEC<br>Honda A-VTEC<br>Yamaha CVVT | Suzuki SNVT<br>INA 3CAM<br>Fiat 3D CAM  |
| Systems in volume production       |                        |  |   |
|                                    | Toyota Valvematic 2008 | BMW Valvetronic II 2001  | Nissan VVEL 2007/2008   |
|                                    |                        |  |  MultiAir 2009 |

Figure 11. Selection of developed VVA units [28].

Referring to camless systems, they can be divided into electro-mechanical, electro-hydraulic and electro-pneumatic VVA units, but their volume production doesn't reach a relevant level because of some control drawbacks [28,29].

On the other hand, fully-variable mechanical valve lift actuations have as disadvantages the low level of variability, slow response times and the circumstance that the individual control of the cylinders is not possible or highly complicated. The best compromise between camless units and continuous mechanical variable valve lift systems is represented by Uniair/Multiair technology, which is electro-hydraulically operated. In fact the system comprises an actuator activated by a camshaft with an integrated fast-acting solenoid valve and valve control software [28]. The cam lift is transmitted hydraulically to the valve and as a consequence the closing of the valve can be triggered prematurely by redirecting the hydraulic pressure [30]. In Figure 12 the Uniair/Multiair system scheme is reported[28].

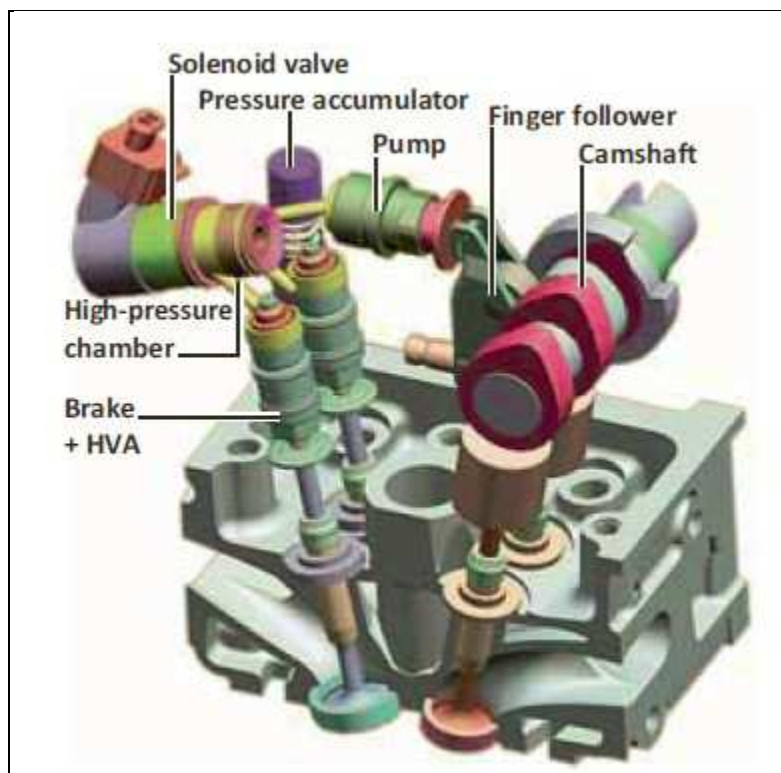


Figure 12. Uniair system main components[28]

Primarily, VVA technology enables to achieve optimal volumetric efficiency over the whole engine map working points by changing valve event timing [31].

In conventional SI engines, as a second VVA advantage, it is possible to operate at partial load by controlling correct air volume that will be drawn in directly in the intake valve ports; thus, the pumping work is reduced, because the throttle valve can

remain completely open or even be omitted [28,31]. The so called Miller cycle which results from the use of the VVA technology basically consists in the early closure of the inlet valve during the intake stroke ahead of the BDC point[32]. The charge trapped within the cylinder is then reduced and subsequently it is also cooled by the further expansion down to BDC [32]. The strategy which is correlated to this described operation is called EIVC, Early Intake Valve Closure. Also Late Intake Valve Closure, LIVC, strategy leads to reduced and cooled trapped mass [32].

In Figure 13 the comparison between full-lift and EIVC indicated cycles for CNG HD engine tested in the present work, at 1200rpm at partial load (25% of full load) is reported[32]. The estimated reduction range in fuel consumption deriving from pumping work decrease amounts in 7÷13% [32].

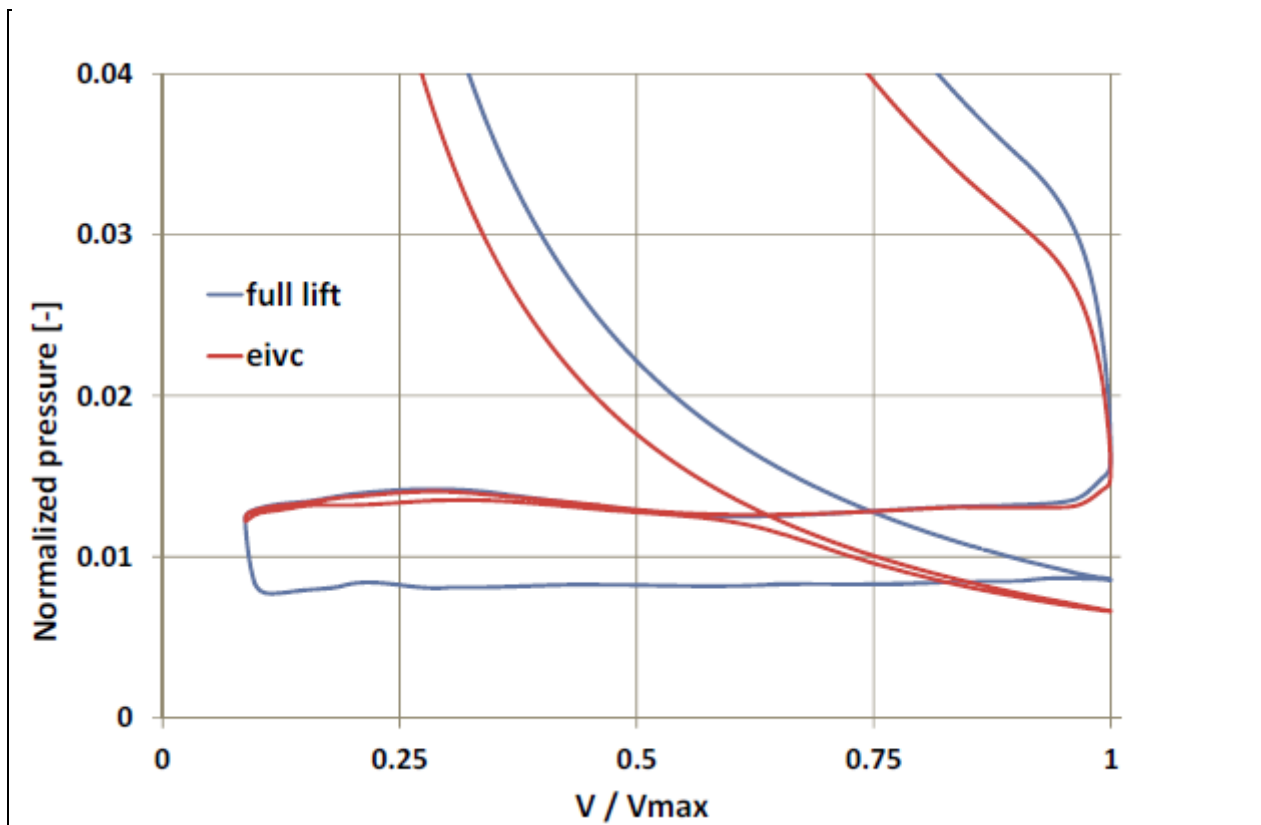


Figure 13. Comparison between full-lift and EIVC indicated cycles at partial load (CNG HD engine, 1200rpm, 25% of full load) [32].

A third VVA benefit could be reached in turbocharged engines at full load operation [32]. In fact, thanks to the lower turbine inlet temperature achieved with the EIVC mode and to the lower in-cylinder temperatures, the boost pressure could be correspondingly increased to a greater extent and the engine performance could be improved [32]. In Figure 14 the predicted comparison between normalized torque as

a function of engine speed at full load operation in the tested CNG HD engine for the full-lift and EIVC strategies is shown [32].

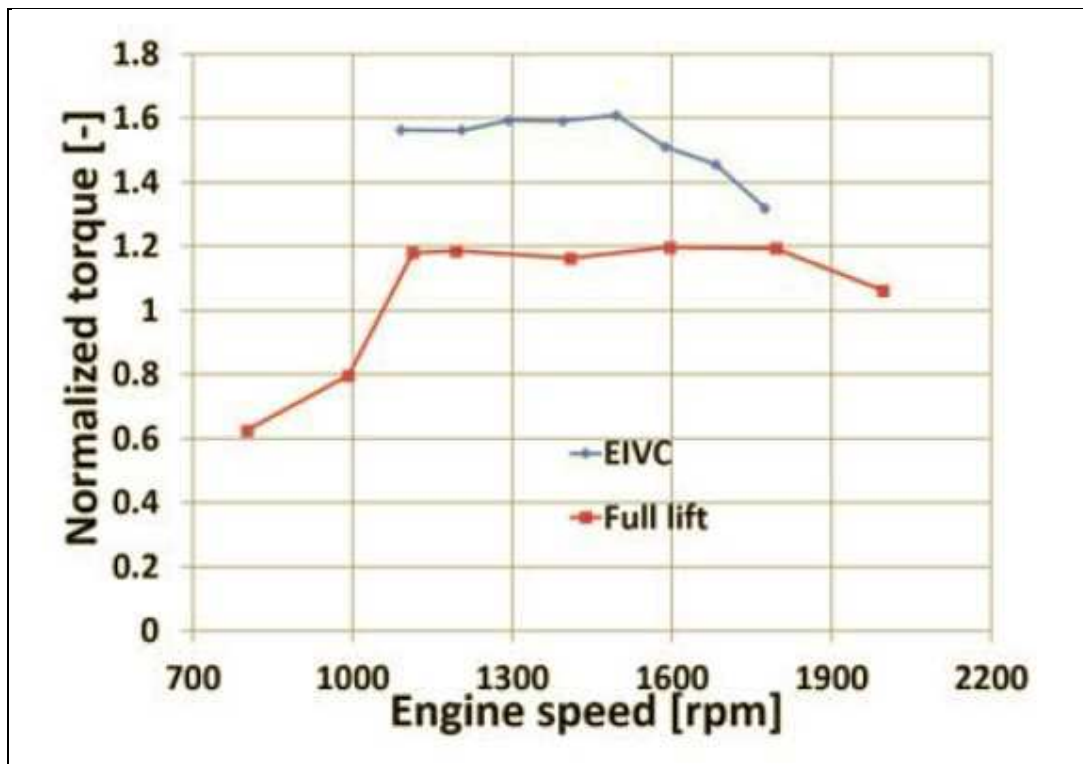


Figure 14. Predicted normalized torque at full load operation with full-lift and EIVC strategies in considered CNG HD turbocharged engine[32].

As a drawback, the adoption of the VVA device can lead to significant limitations in the catalytic converter efficiency along a driving cycle, due to low overall exhaust temperatures [33].

## 1.5 CNG combustion strategies in HD engines

Natural gas engines medium and long term strategy comprises CNG innovative combustion concepts [34,35]. Heavy Duty CNG combustion research deals with four main combustion projects[34].

The first strategy involves the combustion of stoichiometric air-NG mixture; cooled EGR can be added in the intake flow. The charge ignition is provided by the spark plug. CNG can be supplied in the intake port (PFI, Port Fuel Injection) or directly in the cylinder (DI, Direct Injection) at low pressures (up to 100 bar) [34]. An example of low pressure DI CNG spark ignited engine is IVECO Cursor13[36,37].

The second strategy refers to lean combustion of air-NG mixtures ignited by the spark plug in the main chamber or in a pre-chamber, in which the spark ignites a rich air-fuel mixture containing about up to 3% of the total fuel energy (Turbulent Jet

Ignition); the flame then is ejected out of the pre-chamber and propagates into the lean charge of the main chamber [34,38]. Fuel supply can be provided as PFI or DI system. Also in this strategy low injection pressures are adopted [34]. In Figure 15 spark ignition NG combustion strategies schemes are reported; on the left stoichiometric operation and on the right lean mixture combustions are shown[34].

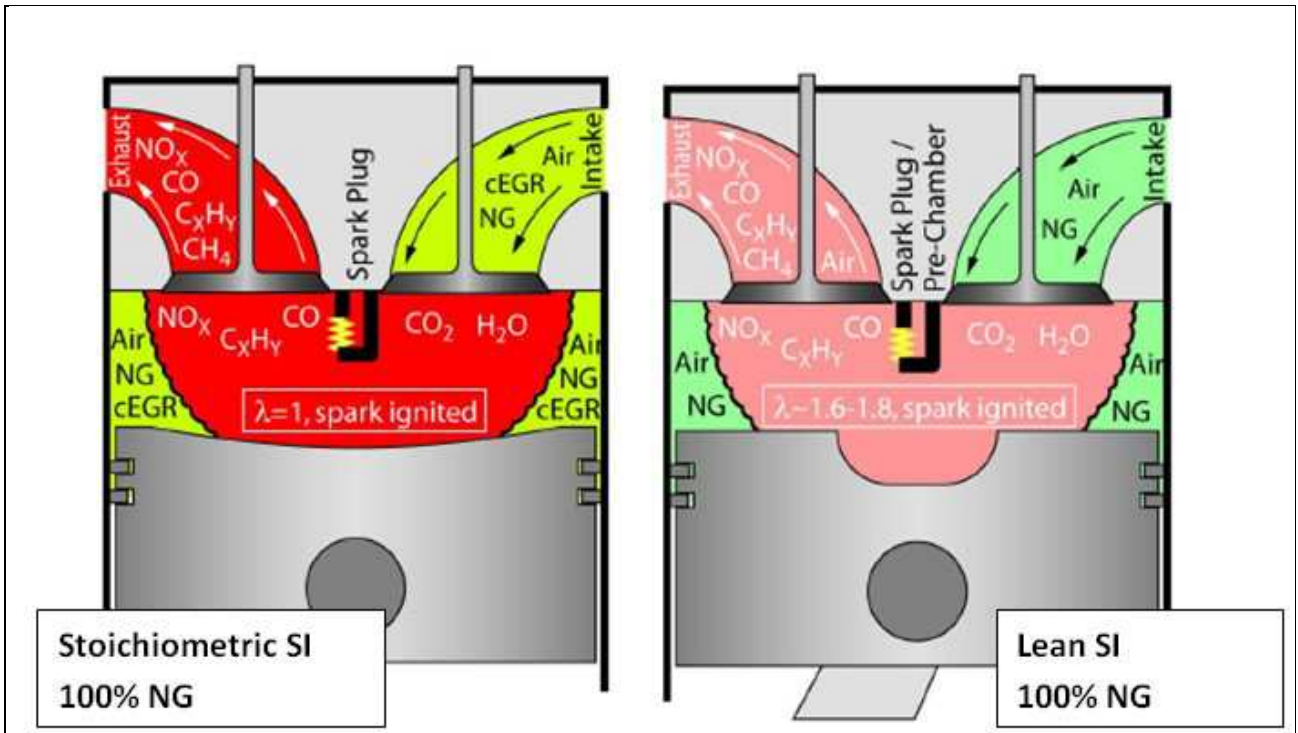


Figure 15. Spark ignition CNG combustion strategies schemes [34].

Other CNG combustion designs are ignited by a diesel pilot injection and then they are called dual fuel strategies. In case of low NG injection pressure, lean combustion develops in the main chamber and the NG fraction reaches about 95% of the total fuel; alternatively, this engine can run totally on diesel fuel[34]. In case of CNG HPDI engine (High Pressure Direct Injection), NG injection pressure can increase up to 600 bar; in initial implementations both fuels injection pressures reached about 300 bar. Pilot diesel fuel fraction is about 10% of total fuel amount and this engine can not run completely as compression ignited[34,39]. In Figure 16 dual fuel CNG combustion designs are illustrated; on the left low pressure strategy and on the right HPDI combustion schemes are shown[34].

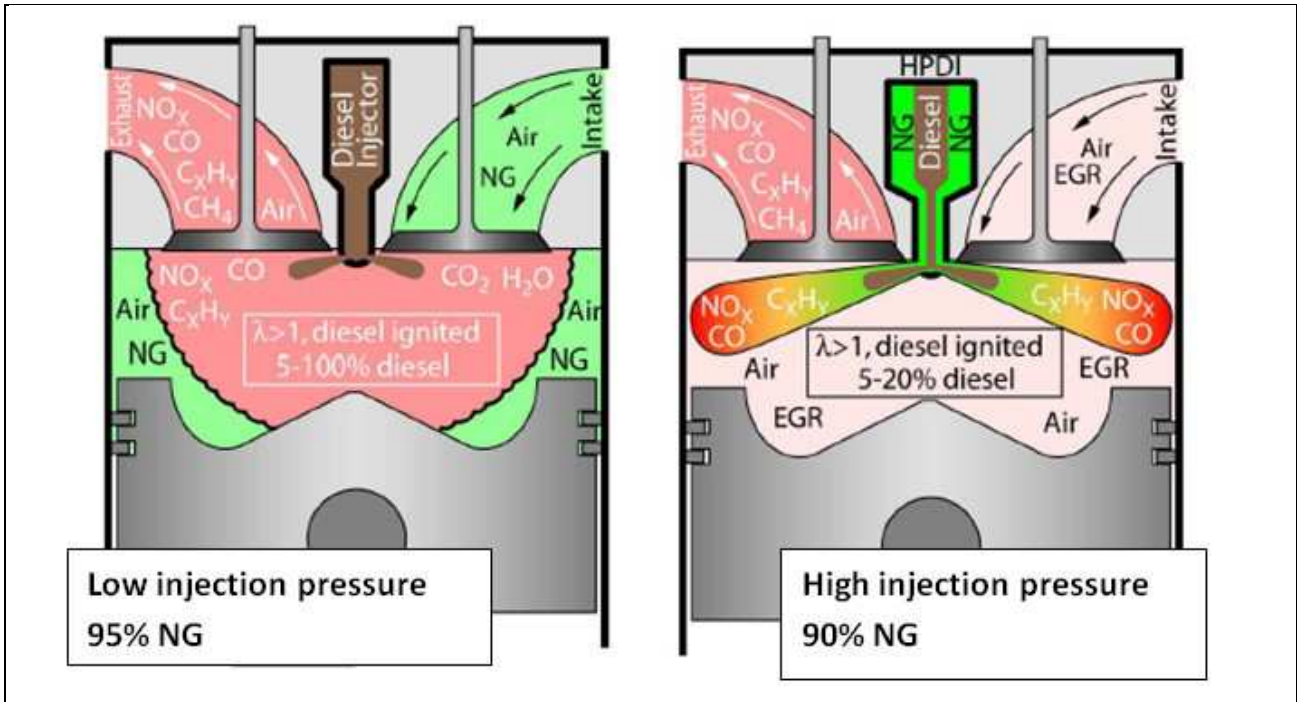


Figure 16. Dual fuel CNG combustion strategies schemes [34].

## 1.6 HD CNG engine aftertreatment systems

Natural gas chemical composition can influence tailpipe emissions. Chemistry variations, that are functions of time and region, can be characterized by following composition parameters. Firstly, *Methane Number (MN)*, which is a scale intended to rate knock resistance. Its reference fuels are methane, with MN of 100, and hydrogen, with MN of 0 [40,41]. Methane Number is related to Motor Octane Number (MON) by the expression:

$$MN = 1,624MON - 119,1 \quad (2)$$

It ranges from 89,5 and 103; higher value means more CH<sub>4</sub> content[40,41].

The second parameter is *Moisture Content* which is due to handling and compression at end distribution infrastructure; it can span from 0 to 11 lb<sub>m</sub>/MM<sub>scf</sub> (that corresponds to 0÷0,176 g<sub>H2O</sub>/Nm<sup>3</sup>)[41].

Third composition measure is provided by *Wobbe Index*, which is expressed by the relation:

$$I_w = \frac{HHV}{\sqrt{G_s}} \quad (3)$$

where  $HHV$  is Higher Heating Value and  $G_s$  is the specific gravity[41].

Lastly, two indicators are represented by *Heavy HC Content* (compounds with more than 12 carbon atoms, that can vary from site to site and also that can derive from compressor oil) and *Sulfur Content* (in the measure of  $0\div 8$  ppmw)[41].

When these composition measures have variations that cause engine control issues, pollutants emissions can change and affect aftertreatment system.

In Figure 18 main aftertreatment systems are illustrated in relation to their corresponding NG combustion strategies[41]. Referring to stoichiometric operation, the commercial Three-Way Catalyst has washcoat composed primarily of  $\gamma$ - $Al_2O_3$  with Pd noble metal. It differs from gasoline engine TWC in the fact that noble metal load is about three times higher than gasoline device[42]. Moreover, in NG TWC when the mixture is slightly rich, the NO reduction process can lead to  $NH_3$  formation which is a poisonous and corrosive gas; on the other hand, when the mixture is slightly lean, NO molecule can react to form  $N_2O$ , which is a greenhouse gas with GWP of about 300 times higher than  $CO_2$ [43].

In relation to lean combustion strategies operations,  $NO_x$  aftertreatment system can be constituted by Lean  $NO_x$  Trap (LNT) subsequent to a Methane Oxidation Catalyst (MOC), as it is shown in Figure 17, in which the possibility of heat recovery (HX) is also proposed[41].



Figure 17. NG lean combustion aftertreatment system[41].

An alternative to LNT device can be represented by the SCR, Selective Catalytic Reductor, which operates by means of urea injection just before the catalyst[41].

With NG lean mixtures, the Particulate Matter (PM) emissions have also to be specifically controlled.

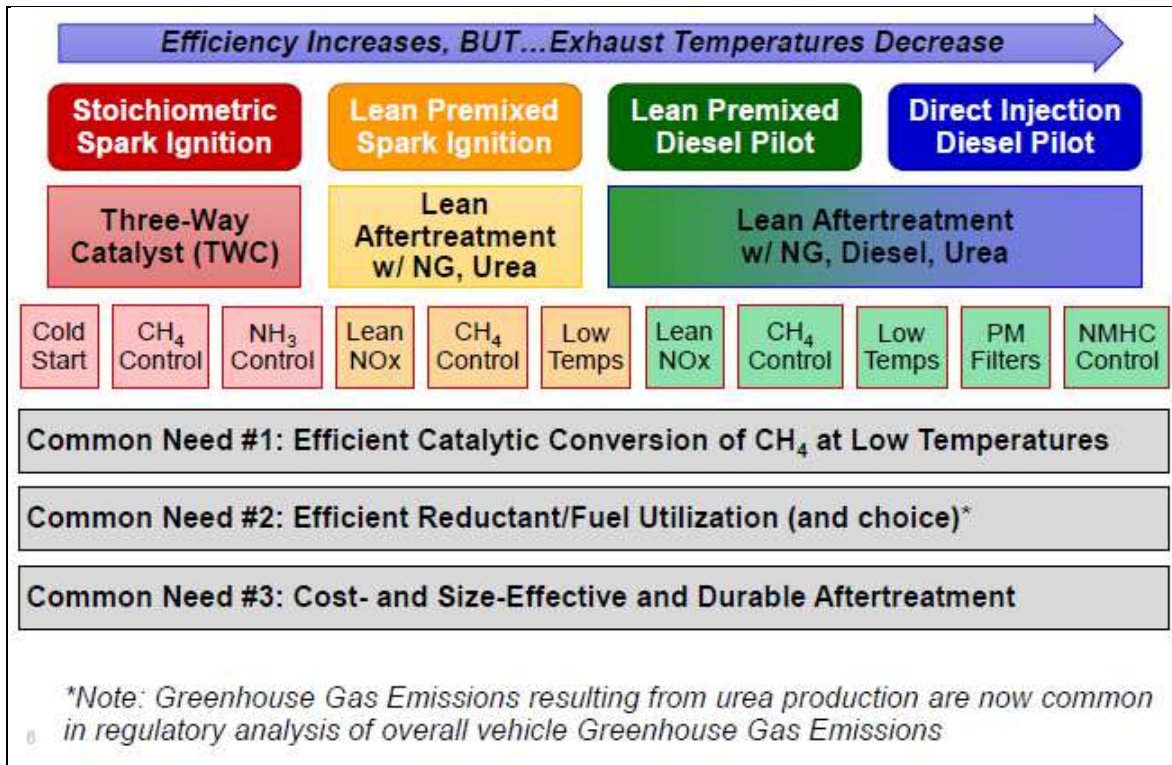


Figure 18. Main aftertreatment systems in heavy-duty NG engines[41]

Further, common issue to all combustion strategies is the efficient catalytic conversion of CH<sub>4</sub> at low temperatures and in the case of short-term thermal exposure histories. In Figures 19 and 20 the HC conversion efficiencies as function of temperature for stoichiometric and lean combustion strategies are reported[41].

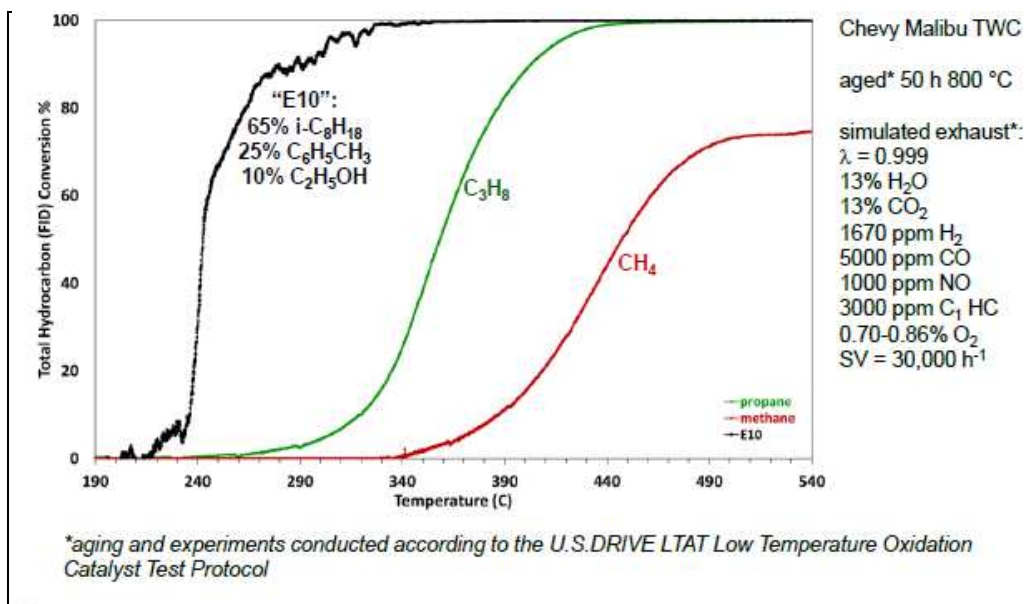


Figure 19. HC conversion efficiency for stoichiometric combustion operation[41].

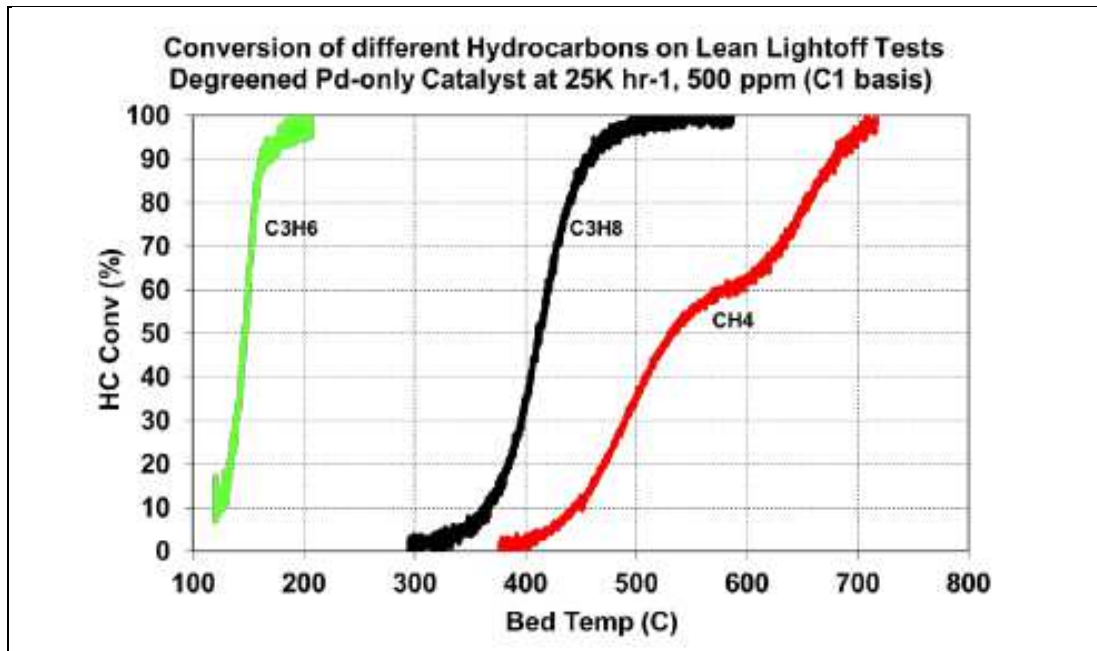


Figure 20. HC conversion efficiency for lean combustion operation[41].

For catalytic CH<sub>4</sub> oxidation, Platinum Group Metals (PGM) are needed; in particular, best performance is provided by palladium. As a Pd drawback, this noble metal has a oxidative state of its own active site, which could cause conversion efficiency control issues due to the PdO formation. Moreover, methane oxidation catalysts are sensitive to water vapor, sulfur poisoning and other impurities; methane light-off curves show unusual hysteresis that can influence control strategies, as it is illustrated in Figure 21 for a Pt/Al<sub>2</sub>O<sub>3</sub> catalyst, in which water vapor presence influence is also shown[41,44].

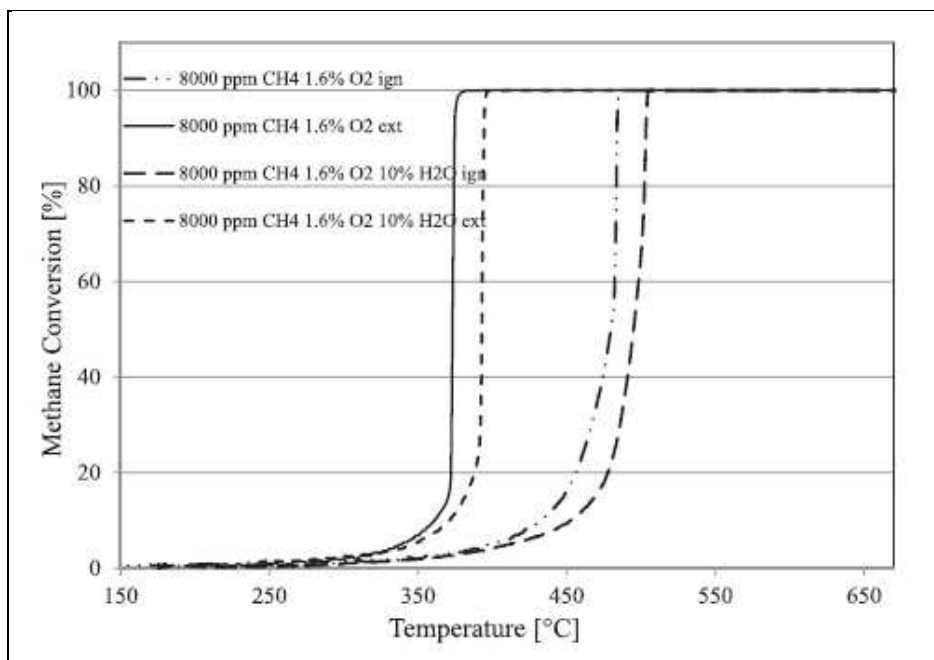


Figure 21. Methane light-off curves during experimental ignition/extinction of 8000ppm CH<sub>4</sub> and 10%O<sub>2</sub>; heating/cooling rate of 7°C/min[44].

## 1.7 CNG engine alternative ignition systems

In CNG engines, the ignition system must deliver a slightly higher voltage to ignite the gaseous mixture versus the liquid droplets that make up the normal charge of gasoline for spark ignition engines[45]. First, alternative solution to spark plug can be the *corona ignition*, which consists of controlled charge ionization produced by high-energy, high frequency electrical field; it creates multiple streams of ions which ignite the fuel mixture throughout the combustion chamber, whereas spark ignition creates only a small arc between the electrodes region[46]. This technology can enable advanced combustion strategies like lean burn and high exhaust gas recirculation (EGR). In Figure 22 the corona igniter is illustrated[46].

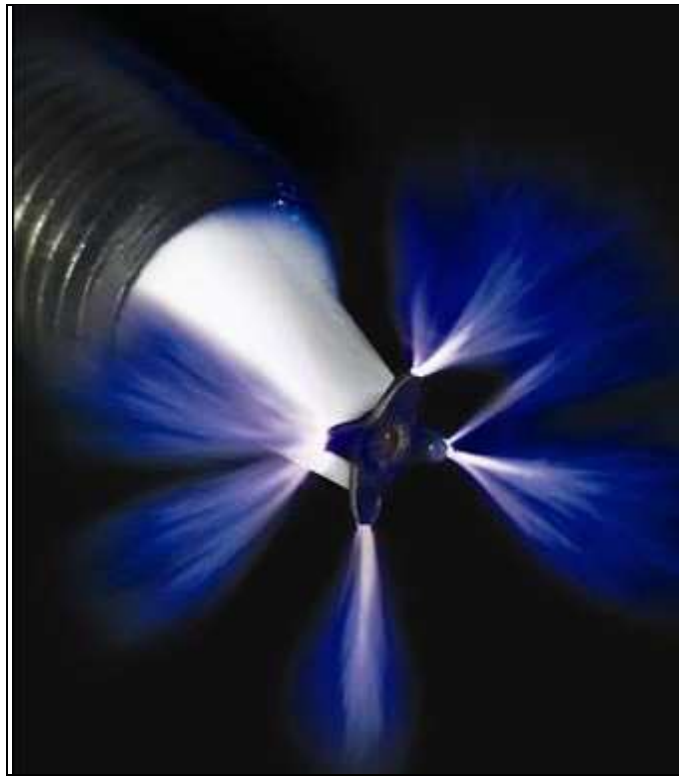


Figure 22. Corona charge igniter illustration [46]

Other ignition techniques are the *Plasma Jet Ignition* (PJI) and *Flame Jet Ignition* (FJI), which both require a combustion pre-chamber[47]. PJI solution operates upon a discharge of about 1 kV associated with a relatively high current to generate plasma from any gas contained in a cavity of about  $10\text{mm}^3$  in volume; on the other hand, FJI needs a discharge of about 20kV relative to a negligible current, to ignite an extra rich air/fuel mixture ( $\lambda$  about 0.5) in a cavity of about  $0.15\div 0.5\text{ cm}^3$  in volume[47]. PJI technique creates a supersonic plasma jet, developing a plume of extremely high

temperature and relatively small mass, which enters the main chamber with insignificant effect on turbulent mixing; on the contrary, FJI solution generates a subsonic turbulent flame jet of sufficiently large mass to induce turbulent mixing, which is significantly slower in charge ignition than PJI operation[47].

The combustion pre-chamber presence is also required in *Hydrogen Assisted Jet Ignition* (HAJI); in this solution pre-chamber volume is 1÷2% of the clearance volume and it is separately fuelled with a small quantity of H<sub>2</sub> (1÷2% by mass). Hydrogen is ignited by a minimum of spark plug energy, due to its wide flammability limit, its high specific energy and low ignition energy; then the flame propagates into the main chamber[48].

Alternative ignition to spark plug is provided also from *Laser Ignition Systems*. Laser ignition is optical breakdown of gas molecules. A powerful short pulse laser beam is focused by a lens into a combustion chamber and near the focal spot a hot plasma is generated[49]. The schematic diagram of laser ignition operation is reported in Figure 23[49].

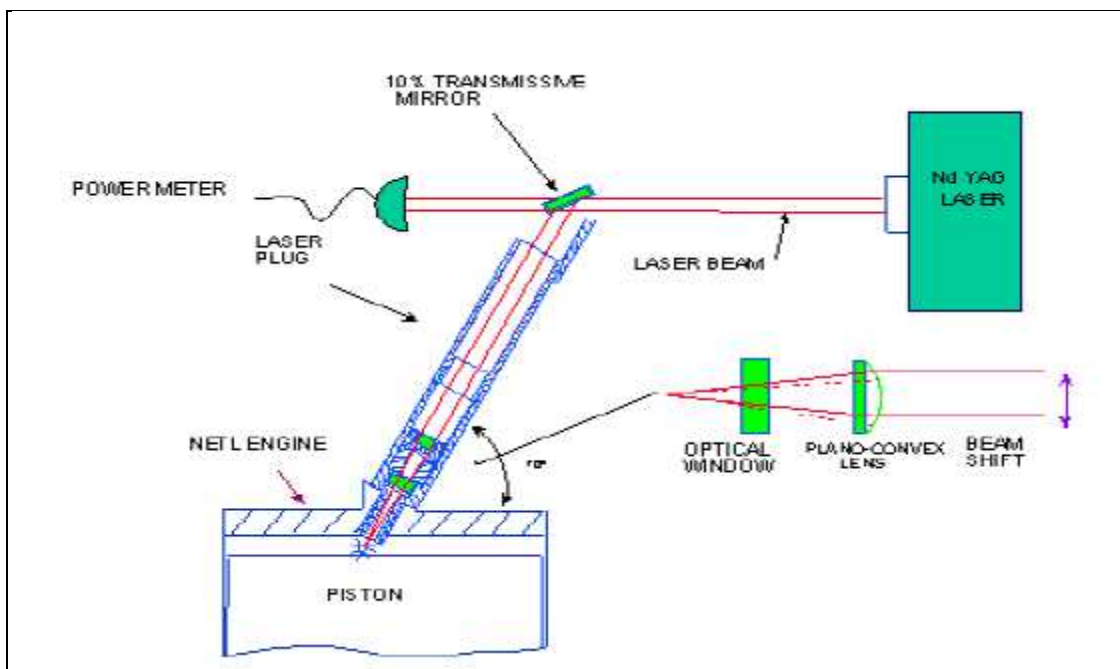


Figure 23. Laser charge ignition system scheme[49].

## 2. Reference engine

The engine studied in the present thesis contest is a 6-in line cylinders, four stroke, turbocharged CNG spark ignition engine prototype called Cursor 8. It operates in stoichiometric charge conditions and it is developed at Fiat Research Center for application to urban buses[32,50]. In Table 4 main functional prototype parameters are reported[32].

| <b>Cursor 8 prototype engine</b> |                     |
|----------------------------------|---------------------|
| <b>Bore</b>                      | 115 mm              |
| <b>Stroke</b>                    | 125 mm              |
| <b>Compression ratio</b>         | 11.5                |
| <b>Turbocharging system</b>      | WG                  |
| <b>Total displacement</b>        | 7.8 dm <sup>3</sup> |
| <b>Power</b>                     | 270 kW @1600÷2000   |
| <b>Torque</b>                    | 1600 Nm @1200÷1700  |

Table 4. Main engine parameters [32].

Engine features an intake manifold with a central entry and it is boosted by a turbocharger provided with twin-entry and fixed geometry. The turbine is waste-gate controlled. An intercooler is placed downstream from the compressor for the inlet air cooling[32]. The prototype engine development has involved the analysis of a Variable Valve Actuation (VVA) system based on a electro-hydraulic operation (Multiair)[33]. In Figure 24 the current available FPT Cursor 8 and the tested prototype engine at the test rig are shown[32,50].

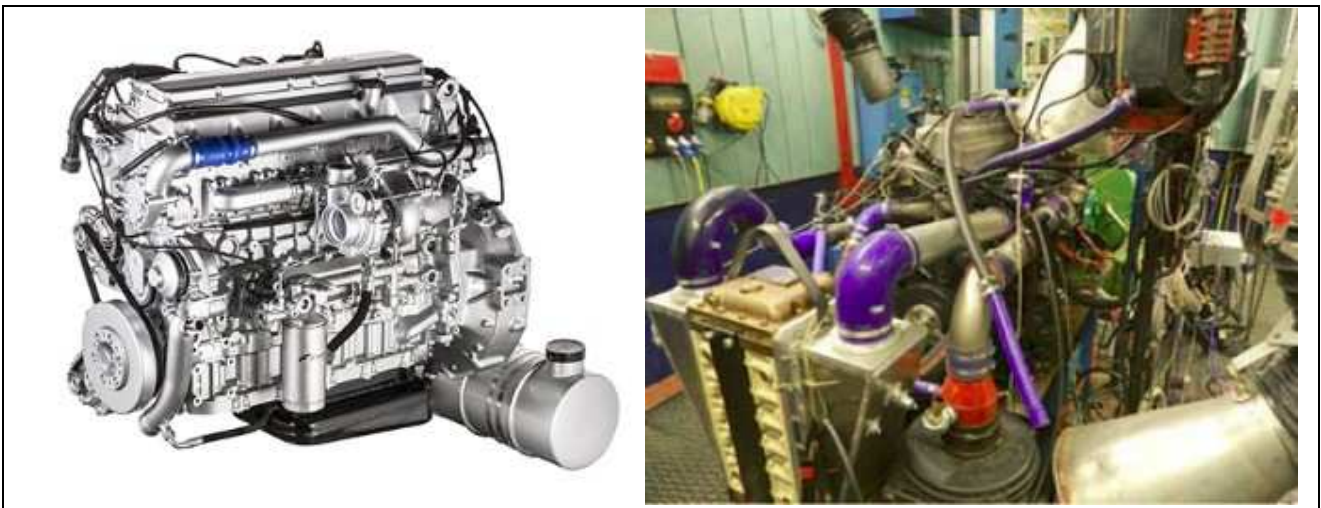


Figure 24. Currently available(on the left) and prototype version(on the right, test rig) FPT Cursor 8[32,50]

## 2.1 GT-Power software

GT-Power (Gamma Technologies, Inc.) is the industry-standard engine and powertrain simulation tool, used by leading engine and vehicle makers and their suppliers. Its ease of use and good integration with the rest of GT-Suite give GT-Power a "virtual engine" perspective[51].

This software is a mathematical tool that simulates with advanced methodology the thermodynamic, fluid-mechanic and chemical processes that define real engine behavior[43]. Models are built by a highly versatile graphical user interface; in fact the heart of the software is design around a series of icons and connectors that define engine components and a logical interface for their use[52,53]. These are shown in a schematic of what is referred to by GT-Power as Project Map. Icons in the Project Map can be energized to reveal related information such as assigned values and formulas and to reveal methodology to edit input data as needed[52]. In the software there are two operating domains called GT-ISE (Integrated Simulation Environment) and GT-POST. GT-ISE builds, executes and manages the simulation process, while GT-POST as a post-processing tool provides access to computed results and plots. In Figure 25 the logic scheme of GT-Power Project Map is illustrated[52].

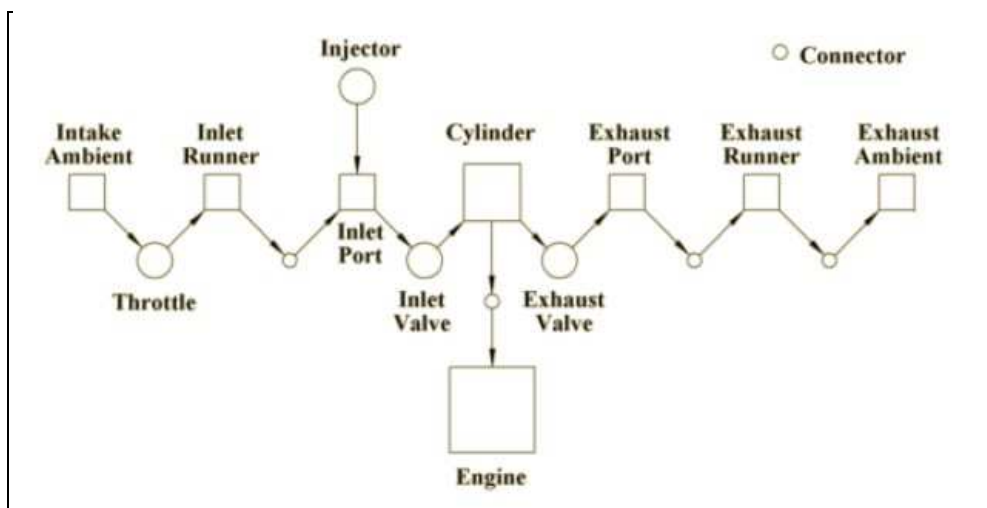


Figure 25. Schematic of GT-Power Project Map[43].

This software is applicable to all types of internal combustion engines, whose performance is designed for steady-state and transient simulations[53].

From the fluid-dynamic point of view, the software solver involves the Navier-Stokes equations, namely the conservation of continuity, momentum and energy equations[53]. The solution is computed in one dimension: all quantities are averaged across the flow direction. The whole system is discretized into many volumes for

which the scalar variables ( pressure, temperature, density, internal energy, etc.) are assumed to be uniform, while the vector variables (mass flux, velocity, etc.) are calculated for each boundary[53]. A schematic of the volumes discretization is shown in Figure 26[53].

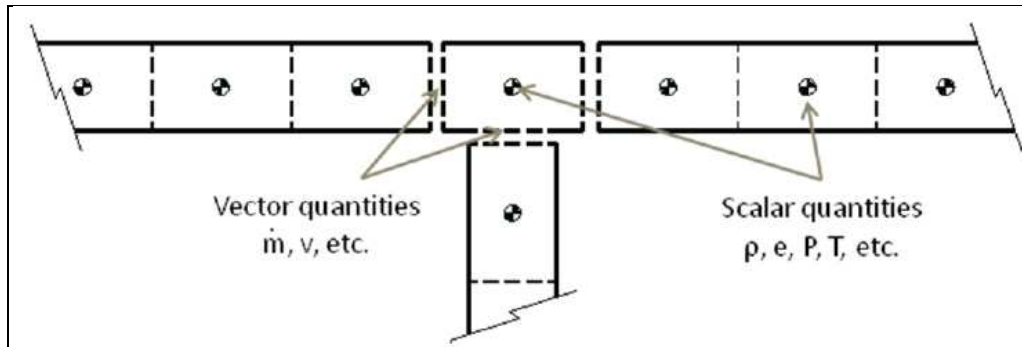


Figure 26. Schematic of volumes discretization approach [53].

The heat transfer from combustion chamber to cylinder walls involves many available sub-models, most of which are developed according to Woschni correlation with or without swirl[11,53,54].

Referring to turbochargers, turbine and compressor performances are modeled using performance maps that are provided by the user as look-up tables[53,54]. The data are organized as several "speed lines", each of which consists of mass flow rate, pressure ratio and thermodynamic efficiency triplets [54]. Raw data tables are then pre-processed by GT-Power so as to create final internal maps over a wide range of operating condition, including the extrapolated range. Turbocharger maps are lumped-parameter models, which are fluid-dynamically coupled to the surrounding 1D pipe elements. Map values can be adjusted by means of a mass-flow and efficiency multiplier (MFM and EM)[54].

For what concerns engine combustion, GT-Power handles its analysis as the transferring of unburned fuel and air masses along with the associated enthalpy from an unburned zone to a burned zone in the cylinder and the release of the chemical energy in the fuel-air mixture[53]. Combustion modeling alternatives are non-predictive or predictive approaches. In non-predictive models, burn rate is simply imposed as a function of crank-angle and it does not depend on variables such as residual fraction or cylinder pressure. Burn rate profile can be imposed directly or by using for SI engines the Wiebe function, which approximates the "typical" shape of burn rate[53]. Wiebe function parameters are adopted in the cylinder object. The GT-Power Wiebe function expression is[53]:

$$Combustion = CE \left[ 1 - e^{-(WC)(\theta - SOC)^{(E+1)}} \right] \quad (4)$$

where CE is combustion efficiency, WC is Wiebe constant, SOC is Start of combustion, E is Wiebe exponent. Each parameter has specific relative GT-Power expression[53]. The independent parameters are usually extracted from the heat-release analysis of experimental in-cylinder pressure-time histories[32].

In predictive models the burn rate is predicted from appropriate variables such as in-cylinder pressure, temperature, cylinder geometry, spark-timing or injection timing. Predictive models typically require calibration to measurement data in order to provide accurate results[53].

Certain physical processes (combustion model, heat transfer model, etc.) can be modeled in order to meet user-specified requirements; in fact their models can be incorporated into GT-SUITE by means of one or more user-defined routines called *User Models* or *User Routines*. These subroutines are specifically invoked in the GT-SUITE model at each computational time step; they can be compiled in Fortran[53].

## 2.2 GT-Power tested engine model

The engine geometric features have been carefully reproduced within the GT-Power model[32]. In Figures 27, 28 and 29 different project map parts representing the complete GT-Power model are illustrated[32].

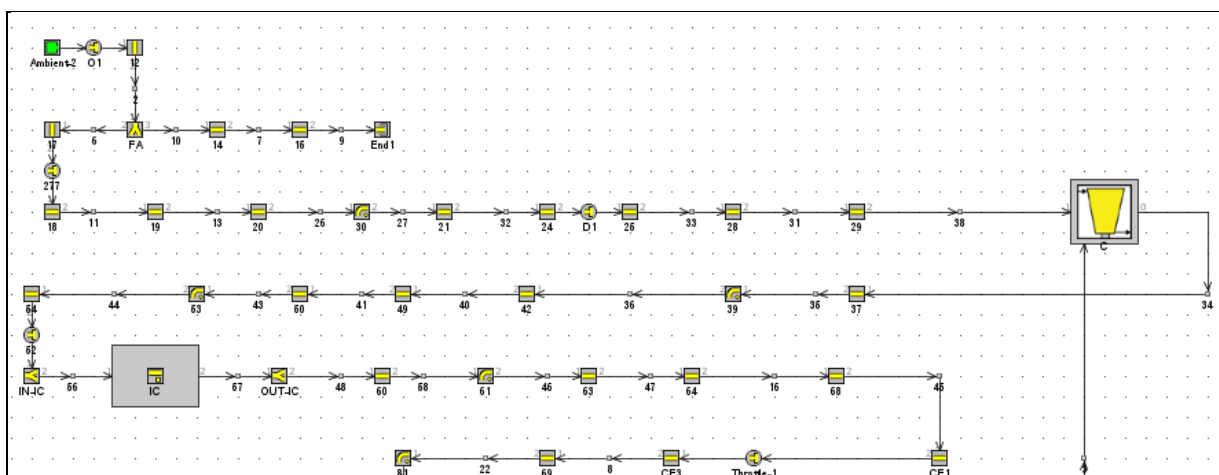


Figure 27. Engine compressor, intercooler and intake manifold [32]

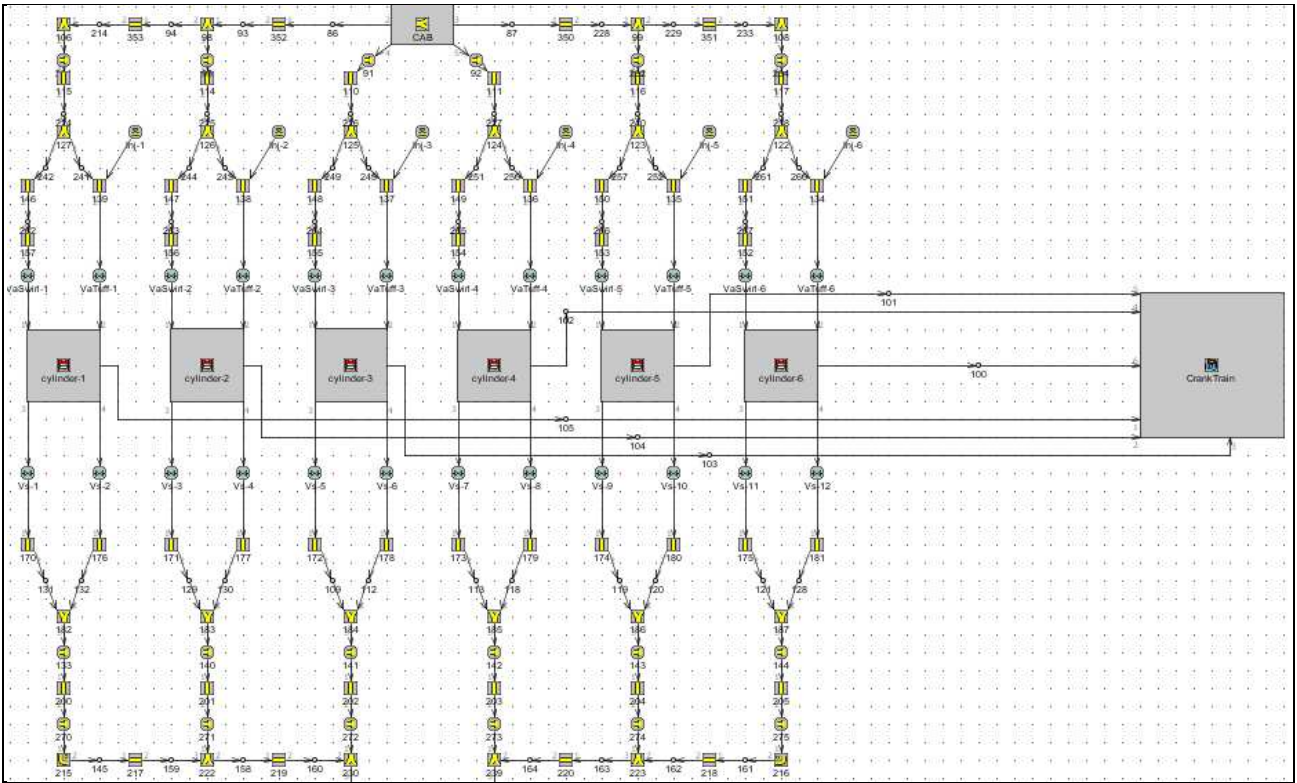


Figure 28. Engine cylinders, intake and exhaust systems [32].

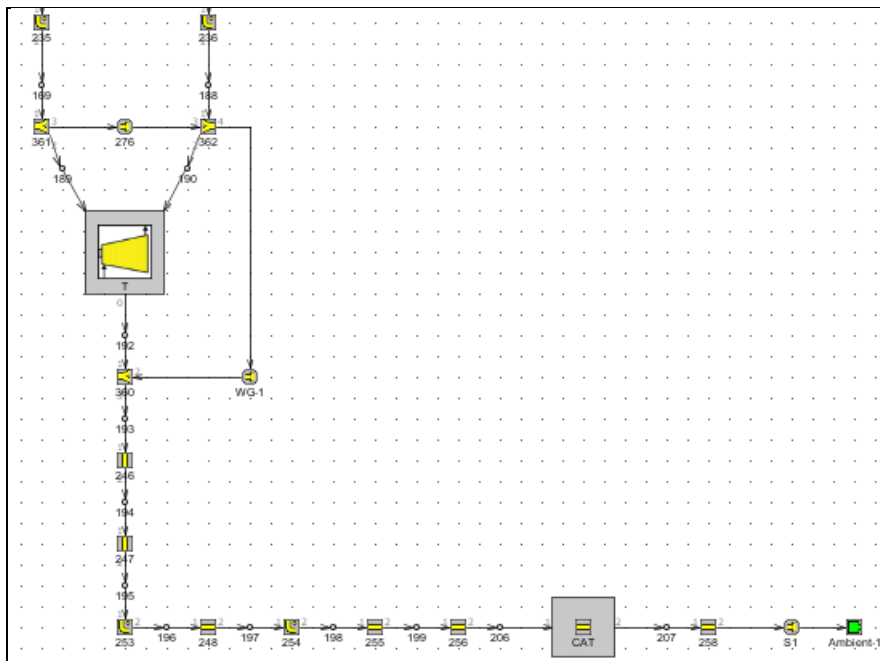


Figure 29. Engine twin-entry turbine and waste gate [32].

As far as the turbocharger is concerned, performance data have been arranged in lookup tables and introduced into the turbocharger object[32]. In particular in Figure

30 the raw turbine mass flow rate map is reported, while in Figure 31 the final GT-Power processed mass flow rate map is shown[54].

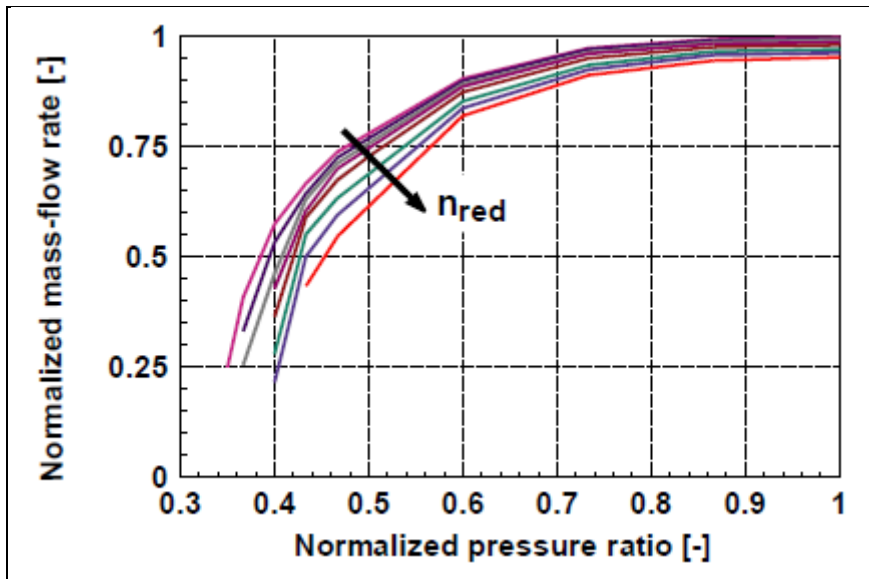


Figure 30. Raw turbine mass flow rate map. Each quantity is normalized to a specific value[54]

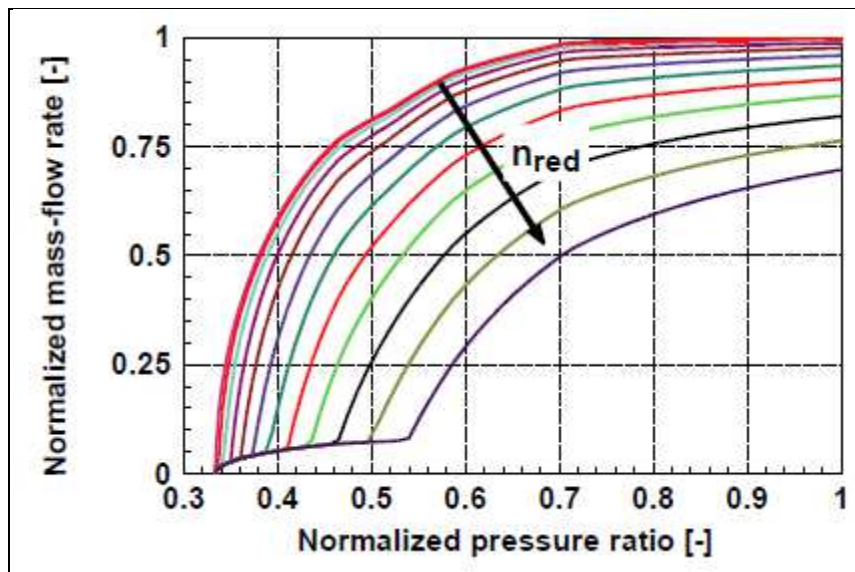


Figure 31. Final mass flow map including the extrapolated range of reduced speed and pressure ratio[54]

As far as it concerns heat transfer exchange between in-cylinder gases and chamber walls, Woschni model without swirl has been assumed, according to which the convective heat-transfer coefficient  $h_c$  is provided by the relation:

$$h_c \left( \frac{W}{m^2K} \right) = 3,26B(m)^{-0,2}p(kPa)^{0,8}T(K)^{-0,55}w \left( \frac{m}{s} \right)^{0,8} \quad (5)$$

where  $B$  is the cylinder bore,  $p$  is the in-cylinder pressure,  $T$  is the temperature and  $w$  is the average cylinder gas velocity[11,53].

Mechanical friction losses have been modeled by Chen-Flynn relation, which allows to compute the friction mean effective pressure  $FMEP$  as:

$$FMEP = A + Bp_{max} + Cu + Du^2 \quad (6)$$

where  $p_{max}$  is maximum cylinder pressure,  $u$  is mean piston speed,  $A$  is constant part of  $FMEP$ ,  $B$  is peak cylinder pressure factor,  $C$  is mean piston speed factor,  $D$  is mean piston speed squared factor[53].

With reference to engine combustion model, an advanced predictive model has been embedded into GT-Power code as it will be discussed in successive Chapter 3; it has been codified in Fortran language and it has been re-called by the software at each work cycle simulation as user model. Each engine cylinder has been entered with its own specific user routine in order to take into account for the residual gases masses.

### Optimizer interface adoption

This feature is supported only for steady-state simulations. It is activated by referring to a specific dropdown menu and it works by running a series of steady-state simulations, in each of which it varies the value of the independent variable and checks the value of the optimization target[55].

The optimizer can properly find a solution if the target variable has a monotonic trend with respect to the selected independent variable as it is shown in Figure 32.

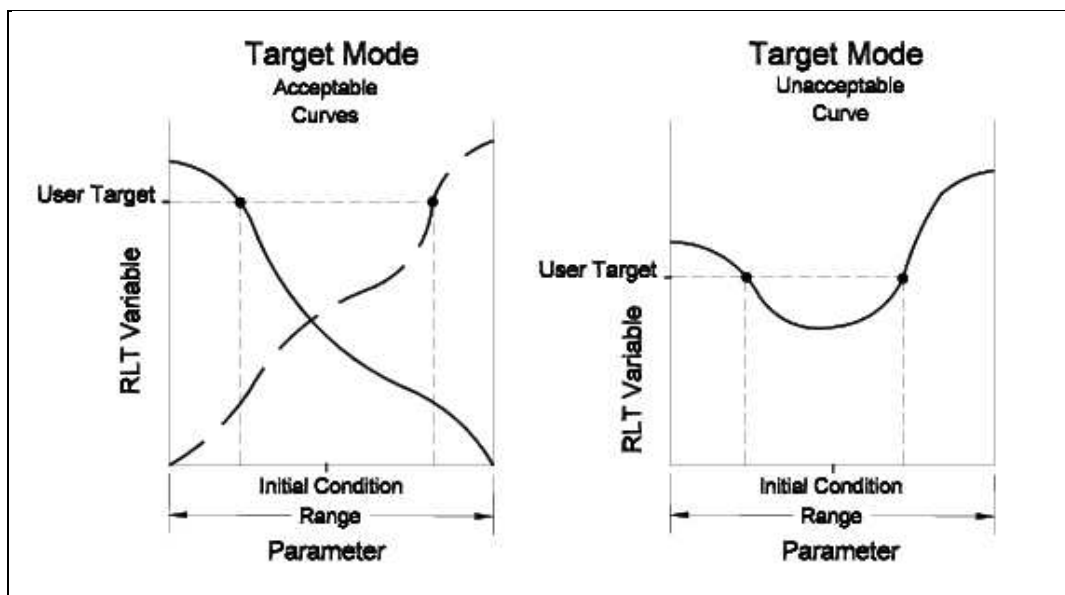


Figure 32. Unacceptable and acceptable initial criteria for a unique optimization solution[55].

In Figure 33 the main setup folder for the Optimizer is illustrated, in which the process goal (solution for Target value or for Optimal value) can be selected and the dependent variable options can be defined[55].

| Attribute                      | Unit | Object Value                        |
|--------------------------------|------|-------------------------------------|
| Goal of Optimization           |      | Target                              |
| Optimization Algorithm Method  |      | discrete-grid                       |
| RLT Variable to be Optimized   |      | btq:CrankTrain                      |
| Target Value of RLT Variable   |      | 610                                 |
| Maximum Number of Iterations   |      | def                                 |
| Iteration Initialization State |      | global_init                         |
| Optimization Plot Request      |      | <input checked="" type="checkbox"/> |
| Run-time Monitor Request       |      | <input checked="" type="checkbox"/> |

Figure 33. Optimizer main setup folder[55].

### PID-Controller adoption

In the case of a study for achieving engine iso-torque evaluations, the PID (Proportional, Integrative, Derivative) Controller tool can be used. It has the purpose to reach and maintain a target value of a sensible quantity from the system (by means of a sensor that measures its cyclic changes ) by controlling some input to the plant. The solution is found in only one simulation run. In Figure 34 the PID controller strategy is illustrated[55].

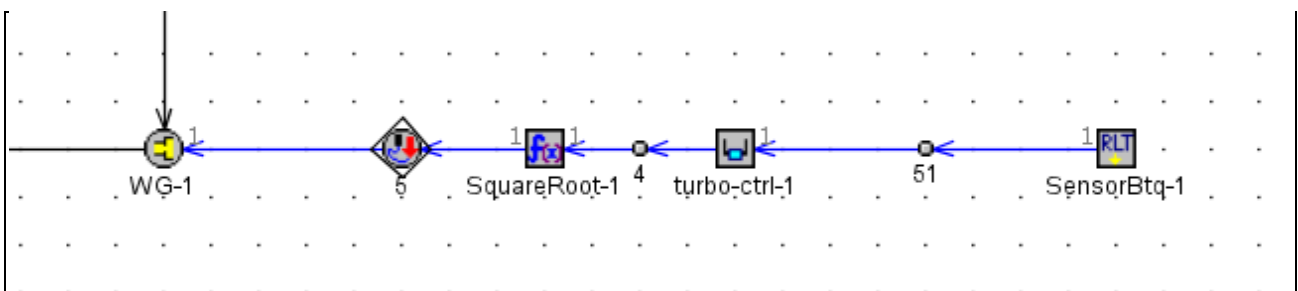


Figure 34. PID controller tool operation.

Three values characterize a PID controller: Proportional gain, Integral gain and Derivative gain. The primary goal when configuring the PID object in Project Map is to find gains that would force the plant to the target value as quickly as possible; the most common approach is usually "trial-and-error" method[53].

A PI controller is perfectly complementary to a system which has a first-order linear response (target parameter) to the actuator behavior(input parameter), as it can be schematized in Figure 35[53].

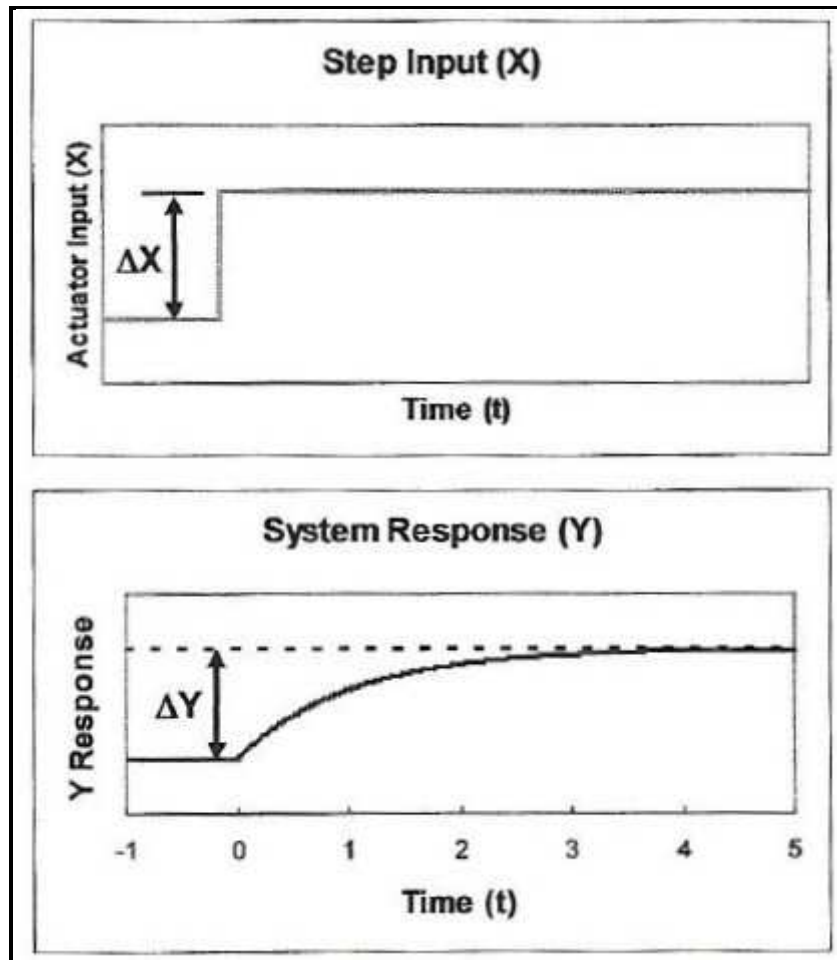


Figure 35. System behavior with first-order linear response[53]

The relation between output response Y and actuator input X can be expressed by:

$$Y = Y_{initial} + K\Delta X(1 - e^{-t/\tau}) \quad (7)$$

where  $K = \Delta Y / \Delta X$  (output ratio), t is time and  $\tau$  is the plant time constant[53].

# 3. Predictive engine combustion model

Predictive engine combustion model applies dedicated concepts for predicting the rate of mixture burning through the consideration of physical principles; it can account for changes of in-cylinder flow, combustion chamber geometry, mixture properties and spark timing. It can also provide spatial resolution about the instantaneous flame location required for the calculation of heat transfer[56].

## 3.1 In-cylinder gases thermodynamic state

The gas charge is split into the unburned zone and burned region, which is in turn divided into additional zones. Each of the burned zones is generated at a specified crank angle during combustion; no mixing is allowed between the burned zones so that temperature gradients take place across the chamber. In Figure 36 a schematic of the combustion chamber divided into different zones is shown[56].

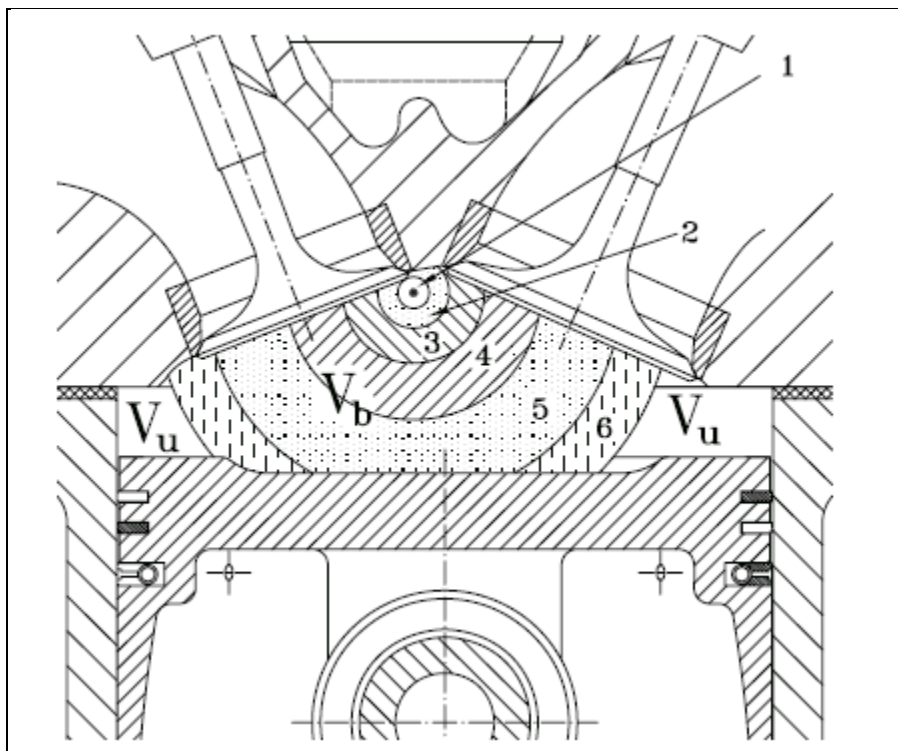


Figure 36. Combustion chamber schematic with illustration of different gases zones[56]

The model applies the energy and mass conservation laws as well as the perfect gas principle to unburned and burned zones. Laws are written in the differential form with reference to the interval of time  $dt = d\theta/\omega$ .

As far as regards unburned and burned zones *volumes*, one can impose their sum to be equal to the instantaneous cylinder volume  $V$  according to[56]:

$$dV_u + \sum_{i=1}^{n-1} dV_{b,i} + dV_{b,n} = dV \quad (8)$$

where  $V_u$  refers to unburned zone volume and  $V_b$  to the burned zone one. The subscript  $i$  refers to the generation order of each burned zone; it range from 1 to  $n$ , this latter indicating the latest generated burned zone[56].

The *mass conservation law* applied to in-cylinder charge yields:

$$dm = d(m_f + m_a + m_r) = dm_u + dm_{b,n} = 0 \quad (9)$$

where  $m$  refers to in-cylinder mass,  $m_f$  is fuel mass,  $m_a$  is air mass and  $m_r$  is residual gases mass[56]. Denoting unburned gases mass with  $m_u$  and burned gasmass with  $m_b$ , their amounts can be expressed in function of burned mass fraction  $x_b$ as follows:

$$x_b = \frac{m_b}{m} \quad (10)$$

$$m_b = x_b m \quad m_u = (1 - x_b)m \quad (11)$$

$$x_b = \sum_{i=1}^n x_{b,i} m_{b,i} = m x_{b,i} \quad (12)$$

The *energy conservation law* for the unburned zone and for each burned zone  $i$  can be written in a suitable form as[54,56]:

$$-q_u A_u \frac{d\theta}{\omega} + V_u dp = (1 - x_b) m di_u \quad (13)$$

$$-q_{b,i} A_{b,i} \frac{d\theta}{\omega} + V_{b,i} dp = m x_{b,i} di_{b,i} \quad (14)$$

where  $i_u$  and  $i_b$  denote unburned and burned gases enthalpies, which are expressed by means of polinomial functions of gas temperature and they can be derived from JANAF thermochemical tables[54].  $Q_u A_u$  and  $q_{b,i} A_{b,i}$  are the heat transfer rates from

the considered charge regions to both the combustion chamber walls and to gas zones that are adjacent to them. Nevertheless, in order to take into account the thermodynamic overall effects rather than local ones, the local heat transfer between adjacent gas zones can be neglected in the evaluation of the average temperature of the unburned and burned gases[56].

Applying the energy conservation equation to the cylinder content, one has[48]:

$$-(q_u A_u + q_b A_b) \frac{d\theta}{\omega} + V dp = (i_{b,n} - i_u) m dx_{b,n} + (1 - x_b) m di_u + m \sum_{i=1}^n x_{b,i} di_{b,i} \quad (15)$$

where  $q_b A_b$  expresses the global heat transfer rate from the burned zone to the walls. The equation that links the *in-cylinder pressure* at a given crank angle to unburned and burned gas temperatures and burned mass fraction  $x_b$  can be written as[46,48]:

$$p = \frac{m}{V} [(1 - x_b) R_u T_u + \sum_{i=1}^n x_{b,i} R_{b,i} T_{b,i}] \quad (16)$$

### 3.2 Burned mass fraction evolution

In present predictive engine combustion model, the evolution equation for the burned-gas mass fraction  $x_b$  can be derived in conformity with the "prompt burning" approach, which implies that the entrained mixture through the flame front promptly burns. In fact the model takes implicitly into account of the global effects of pre-reactions and laminar burn-out past the flame front, directly calculating the burning gas speed, as it will be dealt with further on[56].

Therefore the rate of mixture burning can be expressed by the following relation:

$$dx_b = dx_{b,n} = \frac{1}{m} \rho_u A_{bf} S_b \frac{d\theta}{\omega} \quad (17)$$

where  $\rho_u$  is the density of unburned mixture ahead of the flame,  $A_{bf}$  is the flame front area (unwrinkled) and  $S_b$  is the turbulent flame speed[54,56].

### 3.3 In-cylinder turbulence model

The in-cylinder turbulence generation is analysed by a zero-dimensional model, which is based on the energy cascade concept from mean in-cylinder flow to viscous

dissipation eddies[57]. First flow energy quantity is mean-flow kinetic energy  $K$ , that can be defined as:

$$K = \frac{1}{2}mU^2 \quad (18)$$

in which  $U$  is the mass averaged mean flow velocity and  $m$  is the mass in the cylinder. Second energy quantity is turbulent kinetic energy  $k$ , that is expressed by:

$$k = \frac{3}{2}mu'^2 \quad (19)$$

in which  $u'$  is the turbulence intensity[57].

According to the model, the rates of change of  $K$  and  $k$  can be studied by following expressions[57,58]:

$$\frac{dK}{dt} = \frac{1}{2}\dot{m}_i v_i^2 - P - K \frac{\dot{m}_e}{m} \quad (20)$$

$$\frac{dk}{dt} = P - m\varepsilon - k \frac{\dot{m}_e}{m} \quad (21)$$

where:  $\dot{m}_i$  is the mass flow rate into the cylinder,  $\dot{m}_e$  is the mass flow rate out of the cylinder,  $v_i$  is the jet velocity entering the chamber,  $\varepsilon$  is the rate of turbulent kinetic energy dissipation per unit mass and  $P$  is the rate of turbulent kinetic energy production. The dissipation rate term  $\varepsilon$  is defined as:

$$\varepsilon \cong \frac{u'^3}{L_I} \quad (22)$$

where  $L_I$  is the characteristic large-scale eddy size[57]. This latter term can be related to instantaneous volume of the combustion chamber  $V$  by the expression:

$$L_I = \frac{V}{\frac{\pi}{4}B^2} \quad (23)$$

where  $B$  is the cylinder bore; this definition has the restriction for  $L_I \leq \frac{B}{2}$  [57].

The rate of turbulent kinetic energy production  $P$  can be estimated by the empirical relation:

$$P = 0.3307c_{\beta} \frac{K}{L_I} \sqrt{\frac{k}{m}} \quad (24)$$

where  $c_{\beta}$  is the turbulent dissipation constant adjusted to give the expected profiles of  $u'$  and  $U$  throughout the whole cycle[57,58].

Then, isotropic and homogeneous turbulence intensity values are evaluated at the combustion start by the application of the model to the induction and compression stroked (from IVC to spark timing) by means of numerical integration[57,58].

As soon as the combustion starts, the evolution of turbulence intensity and macroscale are estimated by assuming the conservation of angular momentum of large-scale eddies[57,58]. Therefore, after ignition the following relations hold:

$$\frac{L_I}{L_{I0}} = \sqrt[3]{\frac{\rho_{u0}}{\rho_u}} \quad (25)$$

$$\frac{u'}{u'_{0}} = \sqrt[3]{\frac{\rho_u}{\rho_{u0}}} \quad (26)$$

where the subscript  $0$  refers to the conditions at the instant of combustion start[57].

In a successive model development, the expressions defining the rates of change of mean-flow kinetic energy and turbulent kinetic energy have been modified by the addition of compression-related terms, which take into account the density variation in the cylinder throughout the compression and expansion strokes. With this introduction the K-k model equations have to be integrated also through the combustion phase[58]. Modified equations are written as:

$$\frac{dK}{dt} = \frac{1}{2} \dot{m}_i v_i^2 - P - K \frac{\dot{m}_e}{m} + K \frac{\dot{\rho}}{\rho} \quad (27)$$

$$\frac{dk}{dt} = P - m\varepsilon - k \frac{\dot{m}_e}{m} + k \frac{\dot{\rho}}{\rho} \quad (28)$$

### 3.4 Turbulent flame speed model

With reference to incorporation of new mass through the flame front involving the turbulence-flame interaction, present advanced model represents the laminar flamelets concept, in which the combustion is confined to asymptotically thin moving flamelets embedded in the turbulent flow[57]. The instantaneous behavior of these thin layers is equal to that of laminar flames; then appropriate correction for the effects of stretch and flame curvature can be applied to the product of flamelets surface area and laminar burning velocity in order to compute turbulent burning velocity[57]. Improvements towards the characterization of stretch and flame curvature have defined the estimation of the wrinkled flame surface area. The model describes the wrinkled flame front by means of the fractal geometry concept[57]. According to this theory, flamelets burn confined in a fractal surface of dimension  $D$  for a range of length scales between the so-called *inner*  $\varepsilon_i$  and *outer*  $\varepsilon_0$  cut-off scales. The expression correlating turbulent burning surface area and speed to the laminar ones is[57]:

$$\frac{A_T}{A_L} = \frac{S_b}{S_L} = \left( \frac{\varepsilon_0}{\varepsilon_i} \right)^{D-2} \quad (29)$$

where  $A_T$  and  $A_L$  are turbulent and laminar surface areas and  $S_b$  and  $S_L$  are turbulent and laminar burning speeds, respectively.

The outer cut-off scale  $\varepsilon_0$  can be assumed to be equal to the integral turbulence length scale  $L_I$ , which can be correlated as follows to chamber clearance at TDC  $h_{min}$ , to instantaneous piston shift with respect to TDC  $S_p$  and to a tuned coefficient  $C_L$ [57]:

$$\varepsilon_0 = L_I = C_L(h_{min} + S_p) \quad (30)$$

This definition of the integral turbulence length scale can be alternative to that of equation (23).

The inner cut-off scale  $\varepsilon_i$  can be taken equal to the turbulence microscale  $\eta$  according to the correlation:

$$\varepsilon_i = \eta = L_I \left( \frac{u' L_I}{\nu} \right)^{-\frac{3}{4}} \quad (31)$$

where  $\nu$  is the unburned gas kinematic viscosity[57].

Fractal dimension  $D$  can be expressed by a widely-applied correlation as a function of non-dimensional turbulence intensity  $u'/S_L$  as:

$$D = \frac{2}{1 + \frac{u'}{S_L}} + \frac{2.35}{1 + \frac{S_L}{u'}} \quad (32)$$

As  $u'/S_L$  increases,  $D$  approaches the value of 2.35, that is the fractal dimension of non reacting turbulent flows[57].

Therefore, the correlation which provides the turbulent burning speed can be written:

$$\frac{S_b}{S_L} = \left[ \frac{C_L(h_{min} + S_p)}{C_L(h_{min} + S_p) \left( \frac{u' C_L(h_{min} + S_p)}{\nu} \right)^{\frac{3}{4}}} \right]^{D-2} \quad (33)$$

More specifically, a model refinement is requested because the wrinkling turbulent effect on flame front should be a function of the ratio between flame front and eddies dimensions. Consequently, in equation (33) the integral turbulent length scale at the numerator can be replaced by a function of a characteristic linear dimension related to unwrinkled burned front area  $A_{bf}$ , represented by the  $\sqrt{A_{bf}}$ .

Moreover, equation (33) does not take into account the influence of charge density on the growth of the radical species concentration and of the heat transfer across the flame front. Thus, a modulating factor of  $S_b/S_L$  correlated to in-cylinder density was added[57,58].

The resulting turbulent burning velocity expression is therefore[49]:

$$\frac{S_b}{S_L} = \left( \frac{\rho}{\rho_0} \right)^n \left[ \frac{C_L \sqrt{A_{bf}}}{C_L(h_{min} + S_p) \left( \frac{u' C_L(h_{min} + S_p)}{\nu} \right)^{\frac{3}{4}}} \right]^{D-2} \quad (34)$$

where  $\rho$  is the instantaneous average charge density, while  $\rho_0$  represents the same parameters at a crank angle that varies from engine to another. A better fit between experimental and numerical data can be obtained if  $n = 1.25$ [58].

### 3.5 Laminar flame speed submodel

In order to calculate the absolute value of the turbulent burning velocity  $S_b$  starting from  $S_L$  and  $S_b/S_L$ , a laminar flame speed model is required[58]. The laminar burning velocity can be evaluated by means of the following power function:

$$S_L = S_{L,0} \left( \frac{T_u}{T_0} \right)^\alpha \left( \frac{p}{p_0} \right)^\beta (1 - 1.5x_{res}) \quad (35)$$

where  $T_0 = 298\text{K}$  and  $p_0 = 1\text{atm}$  are reference temperature and pressure;  $S_{L,0}$ ,  $\alpha$ ,  $\beta$  are constant values for a given fuel and  $RAFR$  (Relative Air/Fuel Ratio).  $x_{res}$  is the residual burned gas fraction in the unburned cylinder charge[58].

In detail,  $\alpha$  and  $\beta$  are defined as:

$$\alpha = 2.18 - 0.8 \left( \frac{1}{RAFR} - 1 \right) \quad (36)$$

$$\beta = -0.16 + 0.22 \left( \frac{1}{RAFR} - 1 \right) \quad (37)$$

With reference to CNG operation, the following correlation for constant  $S_{L,0}$  can be used:

$$S_{L,0} = 0.369 - 2.10 \left( \frac{1}{RAFR} - 1.12 \right)^2 - 3.35 \left( \frac{1}{RAFR} - 1.13 \right)^3 \quad (38)$$

### 3.6 Flame kernel growth

During initial flame kernel phase, the energy release is so small that the combustion effect on pressure rise is negligible. Then, the global effect can be considered by means of a lumped parameter represented by the crank angle interval between spark timing and the angle at which the 1% of cylinder mass has burned, namely  $\Delta\theta_{0-1\%}$  [58]. More specifically,  $\Delta\theta_{0-1\%}$  is determined by the following expression:

$$\Delta\theta_{0-1\%} = a[1 + b(RAFR - RAFR_0)^2] p_{SA}^{-c} \exp\left(\frac{d}{T_{u,SA}}\right) \quad (39)$$

where  $a$ ,  $b$ ,  $c$  and  $d$  are experimentally evaluated for each fuel;  $RAFR_0$  corresponds to relative air/fuel ratio at which  $S_L$  has a peak,  $p_{SA}$  and  $T_{u,SA}$  are pressure and unburned gas temperature, respectively, at spark timing[58].

In the range  $SA \div \Delta\theta_{0-1\%}$  a parabolic function is then used to describe the distribution of  $x_b$  versus crank angle; by means of such a parabola one can evaluate the ignited mass at the first computational step[56].

### 3.7 Combustion termination phase

At the combustion completion, the flame front reaches the combustion chamber walls (*wall combustion phase*). During this period a different combustion rate can be specified. In detail the burning rate expression can be written as weighted mean of two contributions[59]:

$$\left(\frac{dm_b}{dt}\right) = w_2 \left(\frac{dm_b}{dt}\right)_{fractals} + (1 - w_2) \left(\frac{dm_b}{dt}\right)_{wall-combustion} \quad (40)$$

where  $\left(\frac{dm_b}{dt}\right)_{fractals}$  is derived from the presented turbulent flame-speed fractal model; the second contribution  $\left(\frac{dm_b}{dt}\right)_{wall-combustion}$  representing wall-combustion burning rate can be specified as follows[59]:

$$\left(\frac{dm_b}{dt}\right)_{wall-combustion} = \frac{m - m_b}{\tau} \quad (41)$$

The switch between the two combustion modes gradually starts when a threshold value of burned mass fraction is reached, namely  $c_{wc}$  (at the transition time  $t_{wc}$ ).  $\tau$  is a characteristic time scale of the process, that is kept constant during the wall combustion phase after the instant  $t_{wc}$ . In particular, its expression is[59]:

$$\tau = \frac{(m - m_b)_{t_{wc}}}{(\rho_u A_T S_L)_{t_{wc}}} \quad (42)$$

The weight factor  $w_2$  can be obtained from the relation:

$$w_2 = \frac{m - m_b}{(m - m_b)_{t_{wc}}} \quad (43)$$

# 4. Numerical engine combustion model calibration

---

Experimental combustion model calibration requires the analysis of engine behavior with respect to relevant combustion and functional parameters, usually named *objective* or *target parameters*, such as in-cylinder pressure  $p$ , mass burned fraction  $x_b$  or heat release rate  $HRR$ , when changing specific model variables, called *output parameters*, which have to be fitted, in most cases, to each specific engine map working point[60].

In the present work the calibration of combustion model comprising the flame - turbulence interaction submodel based on fractal approach is carried out. In particular those variables that has to be tuned throughout the engine map are: 1) the mass burned fraction at which the switch to wall-combustion submodel begins:  $cwc$  and 2) the parameter defining the integral length scale  $L_I$  in turbulence submodel which in first formulation constitutes the outer cutoff length scale of fractal approach:  $C_L$ . The target variables with respect to which the calibration is developed are the *in-cylinder pressure*  $p$  and the *mass burned fraction*  $x_b$  referred to crank angle during a working cycle.

In detail, the tuning process is worked out in two main phases. In the first phase relevant engine map working points are chosen, for which the calibration is selectively elaborated with a trial and error method. In fact a computational simulation is set up for each single parameter value tested; in particular the two parameters  $cwc$  and  $C_L$  are imposed in each simulation as a couple of values and they show an interaction on the main in-cylinder pressure and mass burned fraction trends. Then, changing one parameter can require to fit again in a optimal manner the other parameter.

In the second phase, first step results expansion to the whole engine map is developed, by the research of two mathematical functions which would provide  $cwc$  and  $C_L$  values for whatever working point, given thermodynamical and functional conditions at the combustion start.

## 4.1 Calibration first phase (simulation phase)

In Figure 37 it is reported the overall engine map scheme in which the 14 working points chosen for the first part of calibration are highlighted. On the  $x$ -axis the variables  $n_{min}$  and  $n_{max}$  refer to the minimum and maximum engine speed tested; on the  $y$ -axis it is reported the engine load in percentage. In Table 5 the detailed working points description is shown.

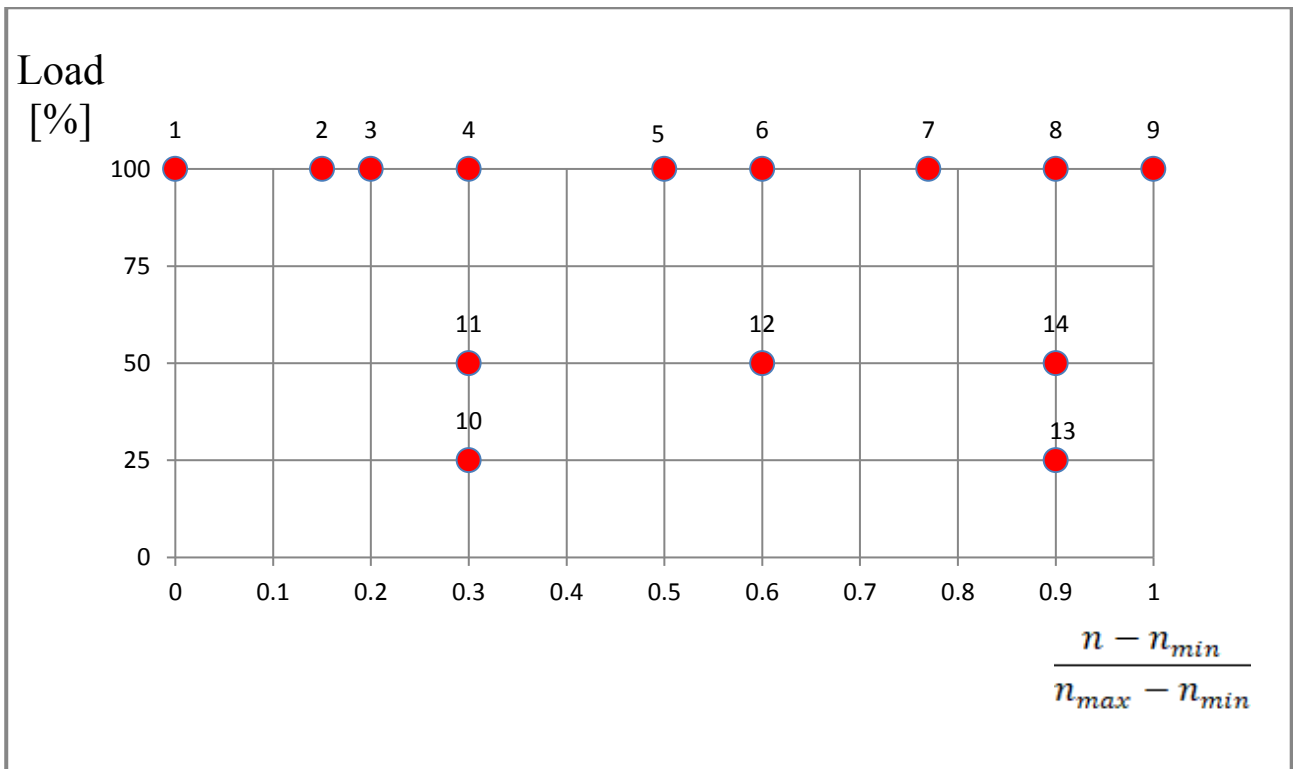


Figure 37. Engine map selected working points for the first phase of calibration.

| Workingpoint | Engine speed [rpm] | Load [%] |
|--------------|--------------------|----------|
| 1            | 802                | 100      |
| 2            | 1001               | 100      |
| 3            | 1100               | 100      |
| 4            | 1204               | 100      |
| 5            | 1404               | 100      |
| 6            | 1605               | 100      |
| 7            | 1804               | 100      |
| 8            | 2000               | 100      |
| 9            | 2106               | 100      |
| 10           | 1189               | 25       |
| 11           | 1189               | 50       |
| 12           | 1591               | 50       |
| 13           | 2000               | 25       |
| 14           | 2000               | 50       |

Table 5. Detailed operative conditions of 14 selected working points.

For each working point, a set of couples of  $cwc$  and  $C_L$  values is entered in computational simulations and for each of them engine combustion model provides predicted in-cylinder pressure  $p$  and the mass burned fraction  $x_b$  in function of crank angle  $\theta$ . Thus the calibration is worked out by means of experimental real pressure and mass burned fraction data, which are compared to predicted ones. In particular, the comparison is elaborated both qualitatively and in terms of relevant curve points quantities.

In fact, from the quality point of view, the choice of optimal  $cwc$  would give the  $x_b$  prediction the gradual switch from the fractal approach to the wall-combustion one, that graphically can be seen in the gradual change of curve gradient: from steep fractal submodel curve to the gentler wall-combustion phase one, which actually experimental data show.

In terms of calibration relevant quantities, each simulation provides maximum in-cylinder pressure  $p_{max}$  and the crank angle at which the mass burned fraction reaches its 50%  $MFB50$ ; by comparison to experimental values, in the tuning tests, maximum target error on maximum pressure is estimated as 3% and on  $MFB50$  as 2 crank angle degrees.

In Figure 39 it is shown the flow-chart representing first phase steps of combustion model calibration. Starting from working point  $i$ , GT-Power engine model which embeds the advanced combustion model is entered with the couple of  $cwc$  and  $C_L$  values and a steady-state computational simulation is run. The procedure core consists on the experimental and simulated data comparison within the assumed maximum errors referring to in-cylinder pressure curve and mass burned fraction trend. If the experimental-predicted matching is not optimal, it will be iteratively necessary to change  $cwc$ ,  $C_L$  or both together values, until most favorable combination of two parameters for that working point will be found. First phase terminates when all the operative points are associated to a couple of  $cwc$  and  $C_L$  values and the correlative final table is created.

Referring to  $cwc$  influence on the mass burned fraction  $x_b$  trend, in Figure 38 it is reported the  $x_b$  curve resulting from imposing  $cwc$  equal to 1, that avoids the application of wall-combustion model, in comparison to experimental curve (working point n.3, 1100rpm, full load,  $C_L = 0.022$ ).

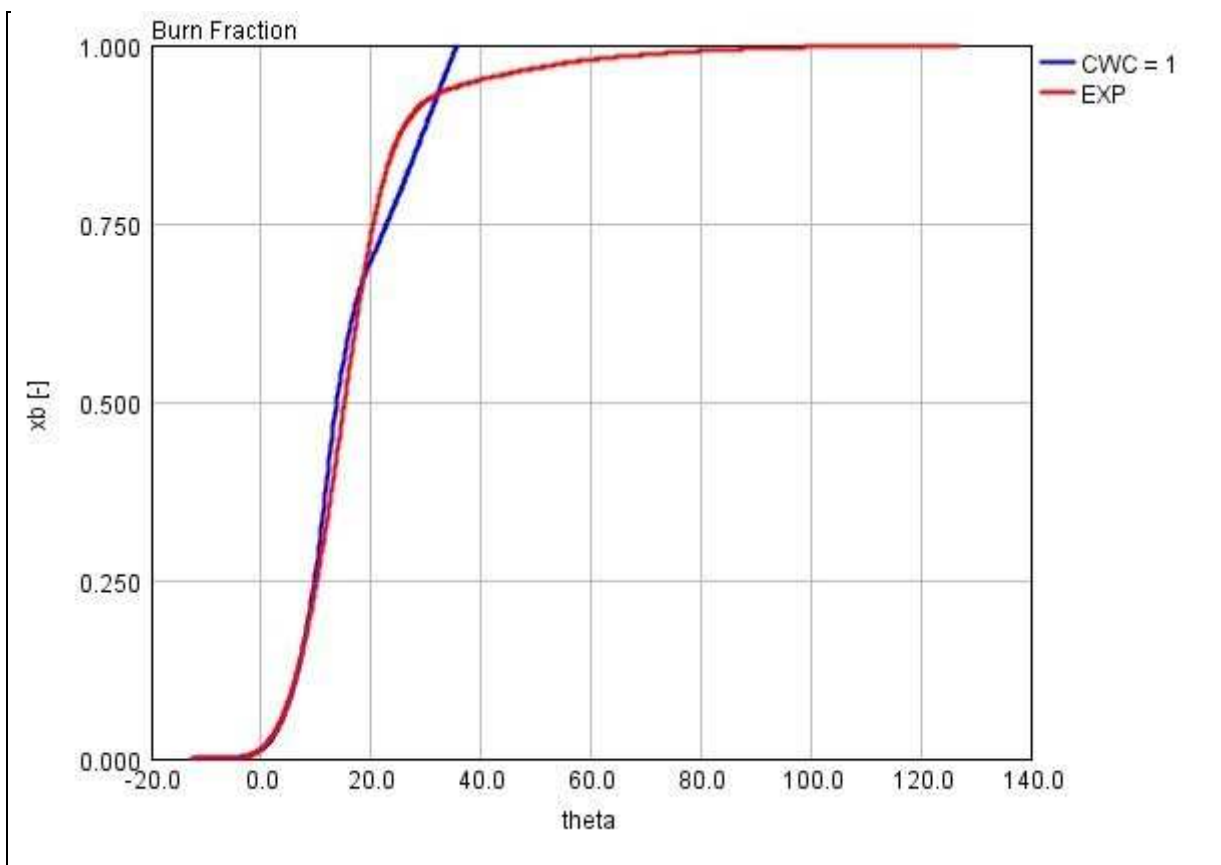


Figure 38.  $x_b$  curve limit condition  $cwc = 1$  for the application of wall-combustion model (1100 rpm, full load)

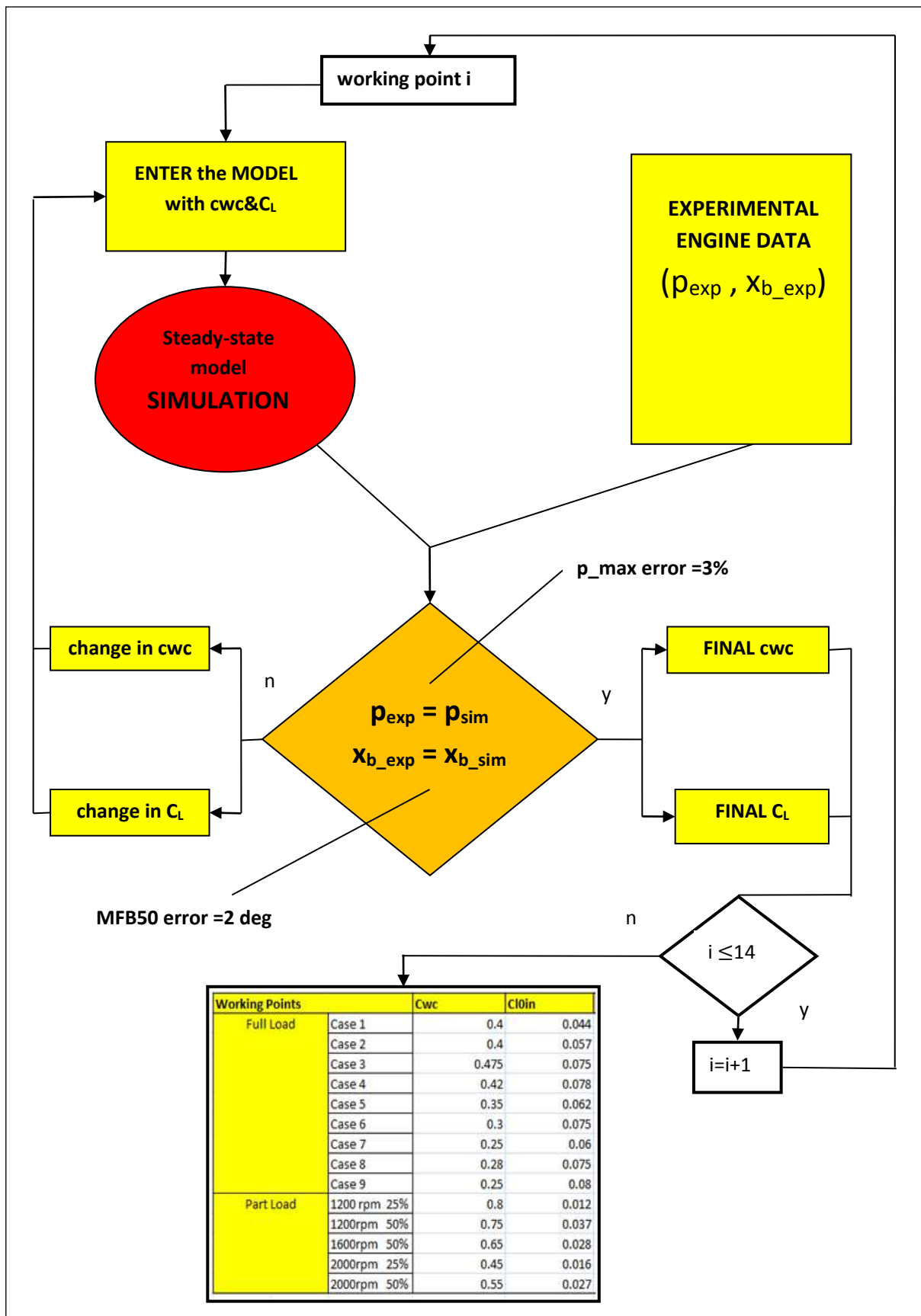


Figure 39. Flow-chart of combustion model calibration first phase.

From a theoretical point of view [47,59], the fractal approach is well suitable for the combustion rapid burning phase, but it would become contradictory if applied in the termination phase after the flame impact on the cylinder wall, as can be seen in Figure 38. In fact, the combustion termination phase requires a gradually decreasing mass burning rate[11,59].

As described in Chapter 3, new modern model supposes the termination phase characterized by the fractal approach fade along the period in which the wall-combustion overture gradually amplifies; thus, the last combustion phase can be optimized by changing the  $x_b$  value ( $cwc$ ) at which this switching period begins[50]. In Figure 40, for the same previous working point, the  $cwc$  value of 0.35 is applied in the combustion model and the gradual curve gradient decrease is shown ( $C_L=0.08$ ).

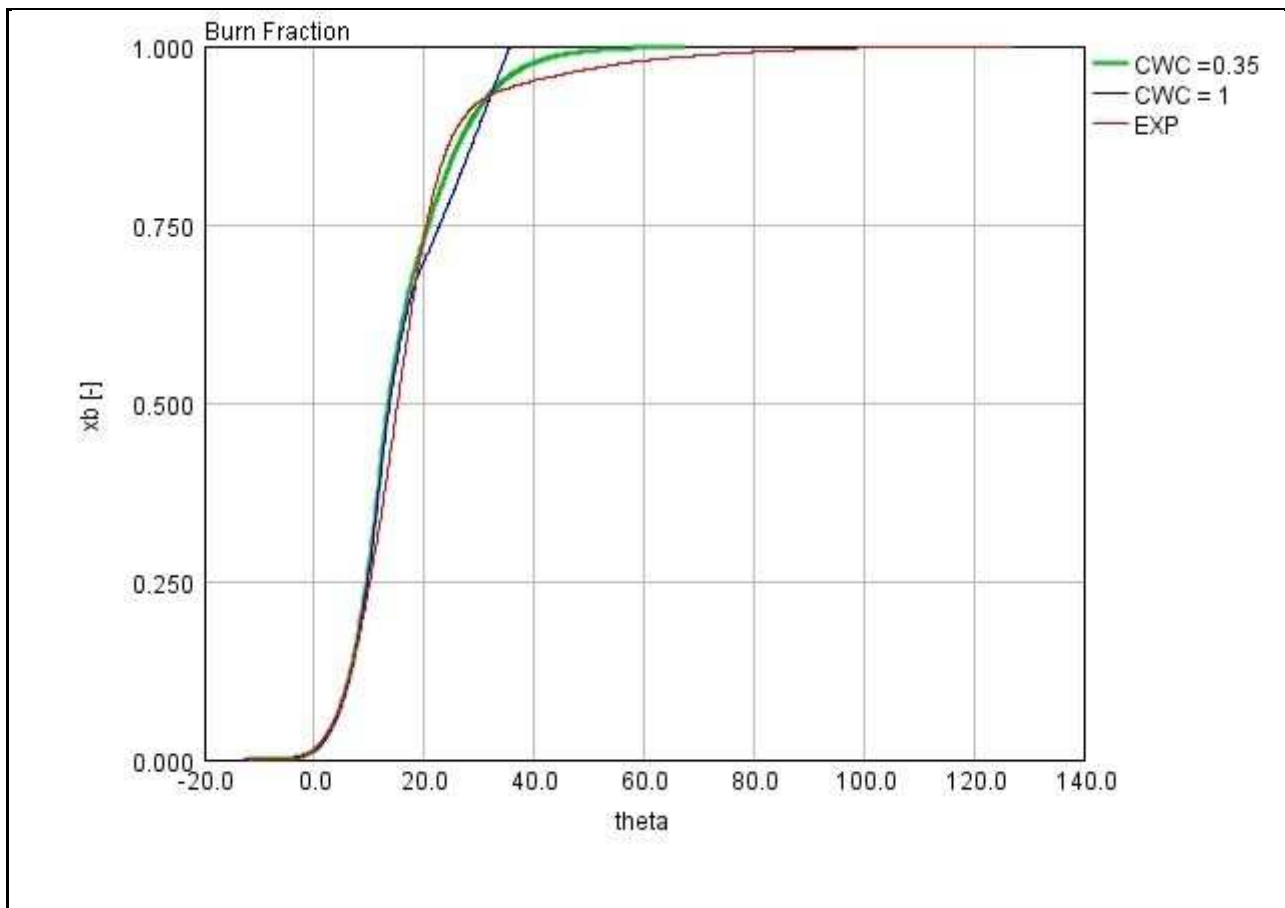


Figure 40. Gradual change in  $x_b$  curve gradient due to  $cwc$  parameter set to 0.35 (1100 rpm, full load)

Moreover, the  $cwc$  influence on mass burned fraction and in-cylinder pressure curves can be different by changing the specific  $cwc$  value; in detail, provided that rapid burning phase ends at about  $x_b$  equal to 0.9 in experimental data, the corresponding angle can be named  $\theta_{90\%}$ . In some predicted curves, a particular  $cwc$  value, proximal to 0.5, determines the minimum possible predicted  $\theta_{90\%}$ , while other

curves are relatively retarded. In Figures 41 and 42, the experimental and simulated mass burned fraction curves are shown for working points n.5 (1404 rpm, full load) and n.6 (1605 rpm, full load), with reference to three selected  $cwc$  values, which highlight the presence of a minimum  $\theta_{90\%}$ . For both the figures,  $C_L$  value is equal to 0.06.

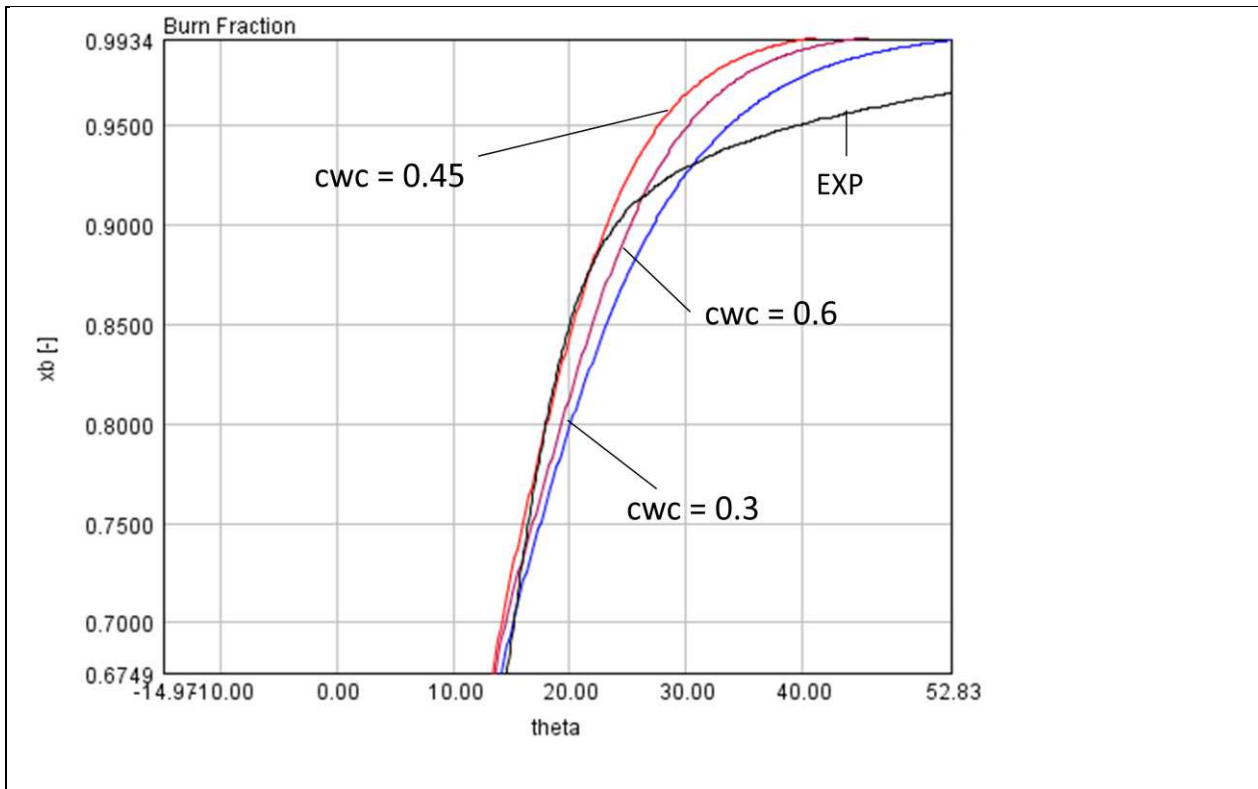


Figure 41. Predicted  $x_b$  curves for different  $cwc$  values ( $C_L=0.06$ ); working point n.5, engine speed 1404 rpm, full load.

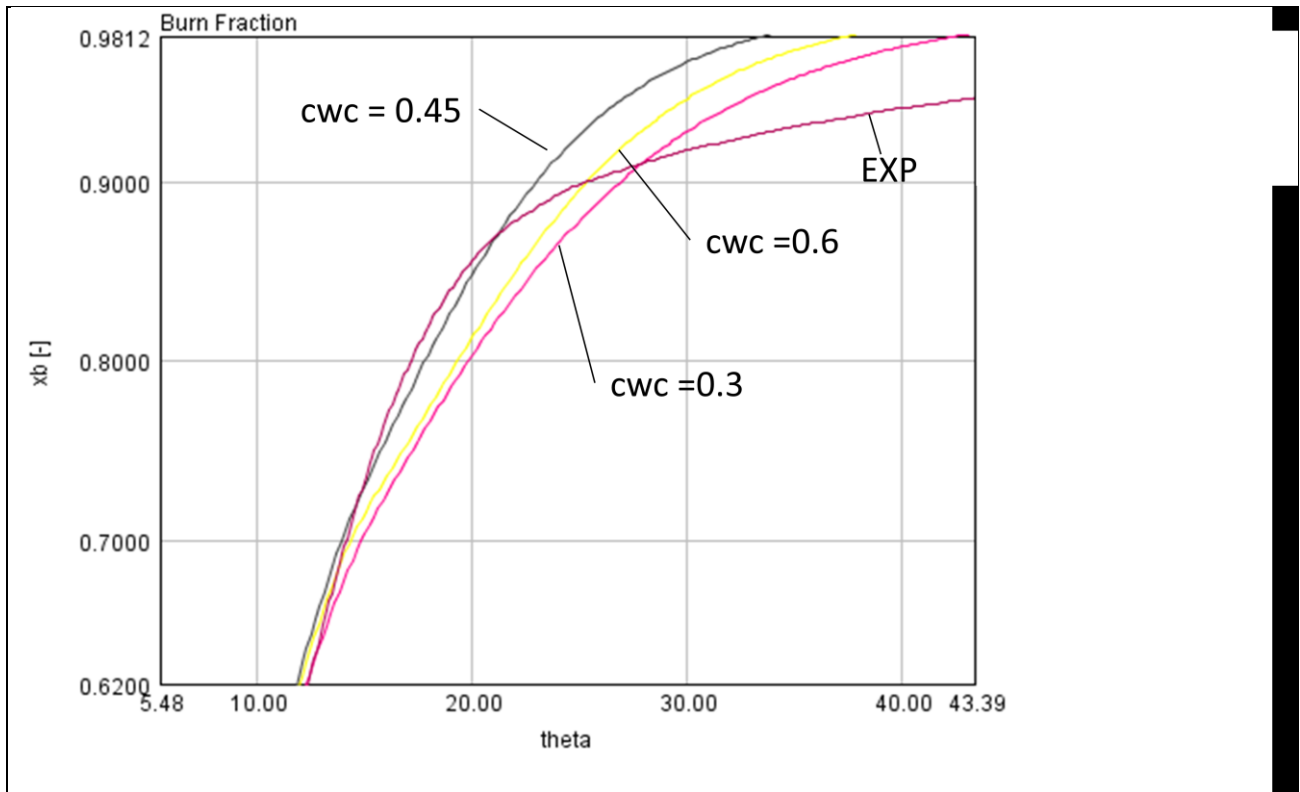


Figure 42. Predicted  $x_b$  curves for different  $cwc$  values ( $C_L = 0.06$ ); working point n.6, engine speed 1605 rpm, full load.

Referring to  $cwc$  value influence on in-cylinder pressure, for those cases in which  $cwc$  promotes earlier  $\theta_{90\%}$  in the mass burned fraction curve, the maximum pressure is correspondingly higher than other cases. In Figure 43 the comparison referred to predicted maximum pressures for working point n.5 (1404 rpm, full load) provided by the same different  $cwc$  values of Figure 41 is reported; in this figure, the maximum deviation between maximum pressures is about 2.4%.

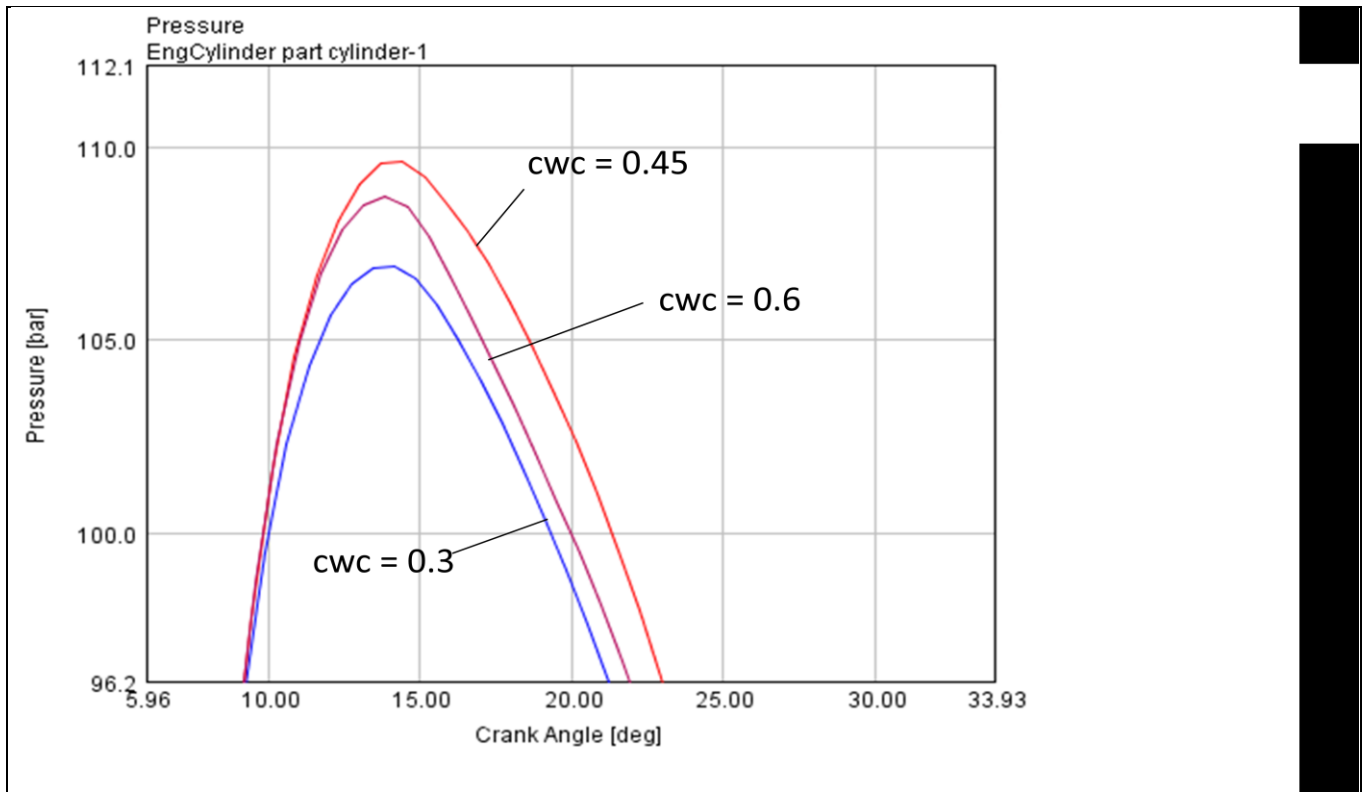


Figure 43. Predicted pressure curves for different  $cwc$  values ( $C_L = 0.06$ ); working point n.5, engine speed 1404 rpm, full load.

For what concerns the  $C_L$  influence on mass burned fraction and in-cylinder pressure curves, increasing  $C_L$  value causes the rapid burning phase  $x_b$  curve to become steeper and consequently enhances the correlative predicted maximum pressure value. In Figures 44 and 45, the  $C_L$  variation effects on  $x_b$  and  $p$  curves are shown for working point n.2 (1001 rpm, full load), at constant  $cwc$  value equal to 0.3.

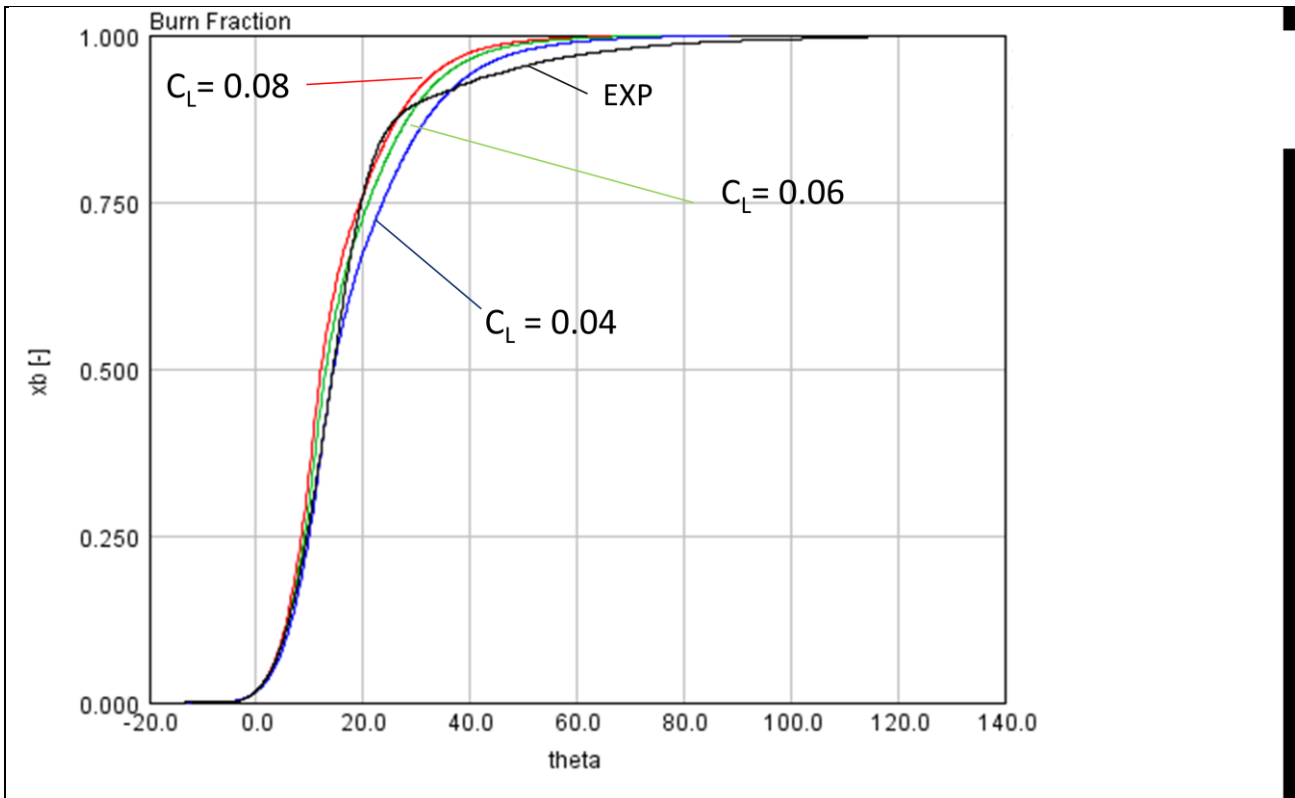


Figure 44. Predicted  $x_b$  curves for different  $C_L$  values ( $cwc = 0.3$ ); working point n.2, 1001 rpm, full load.

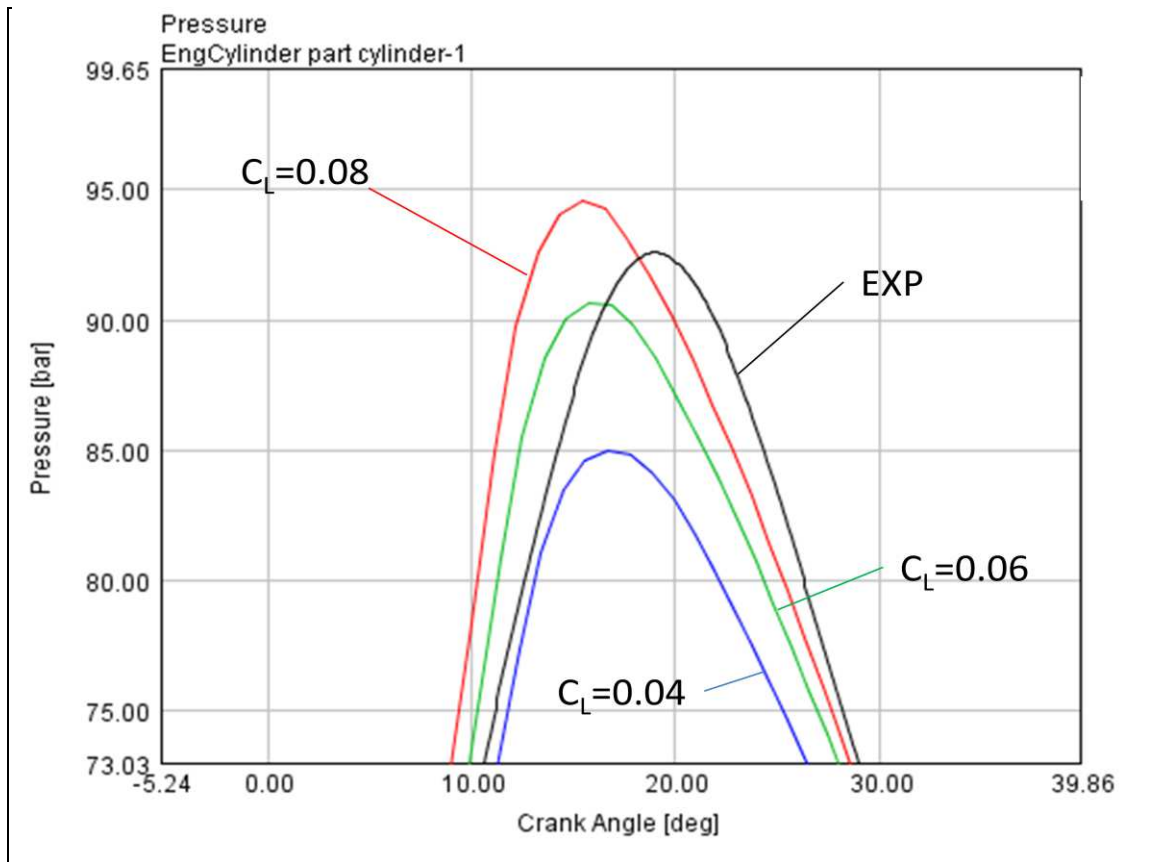


Figure 45. Predicted pressure curves for different  $C_L$  values ( $cwc = 0.3$ ); working point n.2, 1001 rpm, full load.

In Table 6 first phase final  $cwc$  and  $C_L$  values are reported, which have been calibrated over about 200 simulations, in average about 15 simulations for operative point. Predicted mass burned fraction and in-cylinder pressure curves relative to final  $cwc$  and  $C_L$  values for working points n.5, 6 and 11 are shown in Figure 46; in Table 7, MFB50 and maximum pressure deviations from experimental data for all working points at the end of first calibration phase are reported. In Figures 47 and 48 histograms referring to Table 7 data are presented.

| <b>FIRST PHASE</b>    |           |                         |                         |
|-----------------------|-----------|-------------------------|-------------------------|
| <b>Working points</b> |           | <b><math>cwc</math></b> | <b><math>C_L</math></b> |
| <i>Full Load</i>      | <b>1</b>  | 0.4                     | 0.044                   |
|                       | <b>2</b>  | 0.4                     | 0.057                   |
|                       | <b>3</b>  | 0.475                   | 0.075                   |
|                       | <b>4</b>  | 0.42                    | 0.078                   |
|                       | <b>5</b>  | 0.35                    | 0.062                   |
|                       | <b>6</b>  | 0.3                     | 0.075                   |
|                       | <b>7</b>  | 0.25                    | 0.06                    |
|                       | <b>8</b>  | 0.28                    | 0.075                   |
|                       | <b>9</b>  | 0.25                    | 0.08                    |
| <i>Partial Load</i>   | <b>10</b> | 0.8                     | 0.012                   |
|                       | <b>11</b> | 0.75                    | 0.037                   |
|                       | <b>12</b> | 0.65                    | 0.028                   |
|                       | <b>13</b> | 0.45                    | 0.016                   |
|                       | <b>14</b> | 0.55                    | 0.027                   |

Table 6. Optimal  $cwc$  and  $C_L$  values resulting from first phase results.

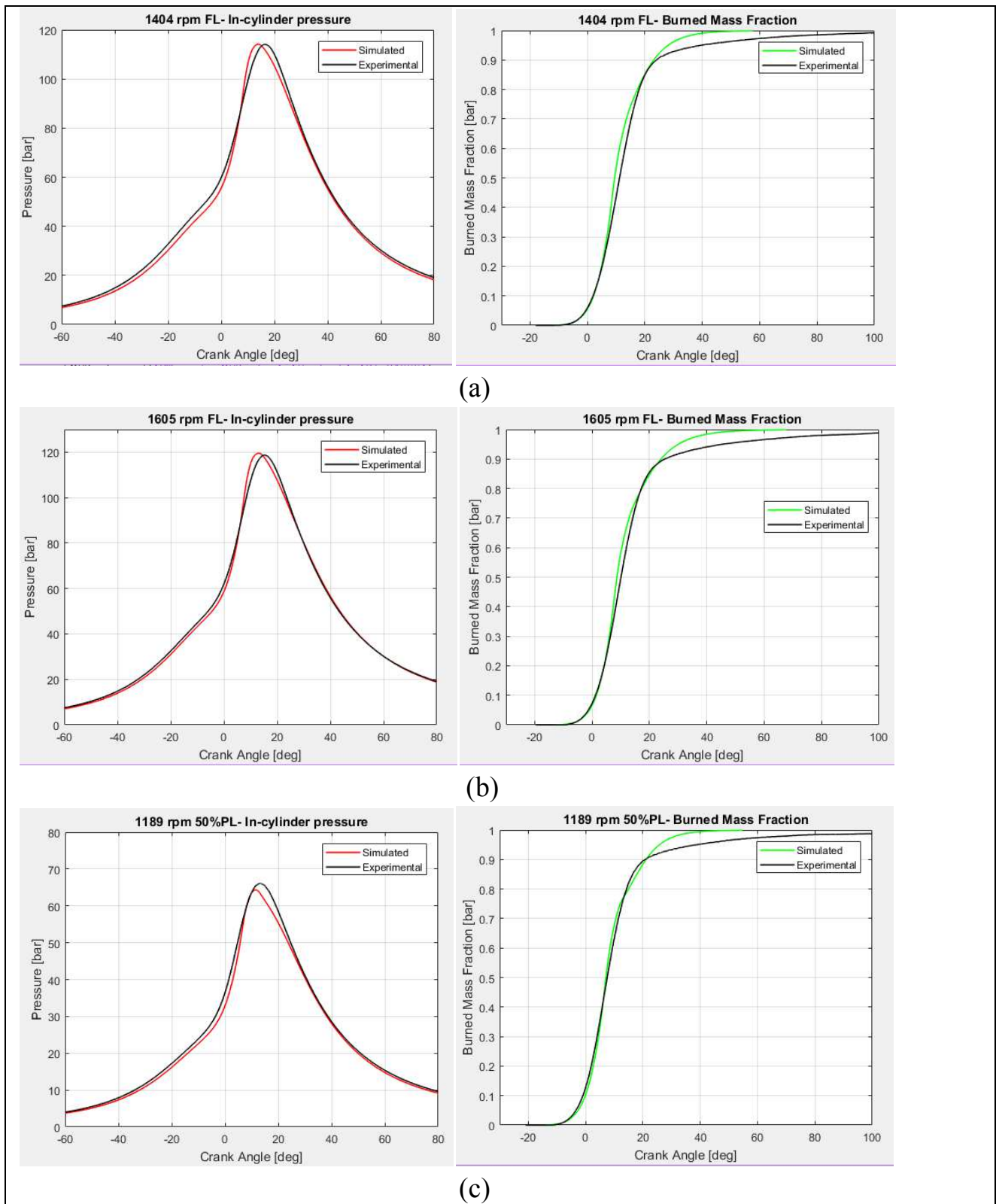


Figure 46. Predicted mass burned fraction and in-cylinder pressure curves correlative to calibrated  $c_{wc}$  and  $C_L$  values for a) working point n.5; engine speed 1404 rpm, full load, b) working point n.6; engine speed 1605 rpm, full load, c) working point n.11; engine speed 1189 rpm, 50% load.

| <i>Calibration First Phase</i> |           |                          |                          |                           |                           |                           |                          |
|--------------------------------|-----------|--------------------------|--------------------------|---------------------------|---------------------------|---------------------------|--------------------------|
| <b>Working points</b>          |           | <i>p_maxexp</i><br>[bar] | <i>p_maxsim</i><br>[bar] | <i>p_max error</i><br>[%] | <i>MFB50 exp</i><br>[deg] | <i>MFB50 sim</i><br>[deg] | <i>MFB50 error</i> [deg] |
| <i>Full Load</i>               | <b>1</b>  | 70.9404                  | <b>71.7775</b>           | 1.18                      | 13.7776                   | <b>12.2664</b>            | -1.5112                  |
|                                | <b>2</b>  | 92.5842                  | <b>95.2137</b>           | 2.84                      | 14.394                    | <b>12.6721</b>            | -1.7219                  |
|                                | <b>3</b>  | 102.701                  | <b>104.119</b>           | 1.38                      | 15.1866                   | <b>13.3818</b>            | -1.8048                  |
|                                | <b>4</b>  | 112.979                  | <b>112.578</b>           | -0.35                     | 12.1608                   | <b>10.6321</b>            | -1.5287                  |
|                                | <b>5</b>  | 114.138                  | <b>114.219</b>           | 0.07                      | 11.1635                   | <b>9.46171</b>            | -1.70179                 |
|                                | <b>6</b>  | 118.729                  | <b>119.591</b>           | 0.73                      | 10.0733                   | <b>8.66002</b>            | -1.41328                 |
|                                | <b>7</b>  | 123.54                   | <b>127.735</b>           | 3.40                      | 8.76845                   | <b>6.08127</b>            | -2.68718                 |
|                                | <b>8</b>  | 116.659                  | <b>110.518</b>           | -5.26                     | 6.77405                   | <b>5.7736</b>             | -1.00045                 |
|                                | <b>9</b>  | 112.693                  | <b>113.399</b>           | 0.63                      | 6.73023                   | <b>4.07535</b>            | -2.65488                 |
| <i>Partial Load</i>            | <b>10</b> | 37.7181                  | <b>37.8695</b>           | 0.40                      | 5.78687                   | <b>1.96835</b>            | -3.81852                 |
|                                | <b>11</b> | 66.185                   | <b>64.3924</b>           | -2.71                     | 7.52139                   | <b>7.07276</b>            | -0.44863                 |
|                                | <b>12</b> | 70.3894                  | <b>65.3268</b>           | -7.19                     | 5.44717                   | <b>5.73222</b>            | 0.28505                  |
|                                | <b>13</b> | 36.6559                  | <b>36.7253</b>           | 0.19                      | 6.46161                   | <b>4.31261</b>            | -2.149                   |
|                                | <b>14</b> | 65.136                   | <b>63.2506</b>           | -2.89                     | 5.90349                   | <b>5.13459</b>            | -0.7689                  |

Table 7. MFB50 and maximum pressure deviations from experimental data for final first phase cwc and  $C_L$  values.

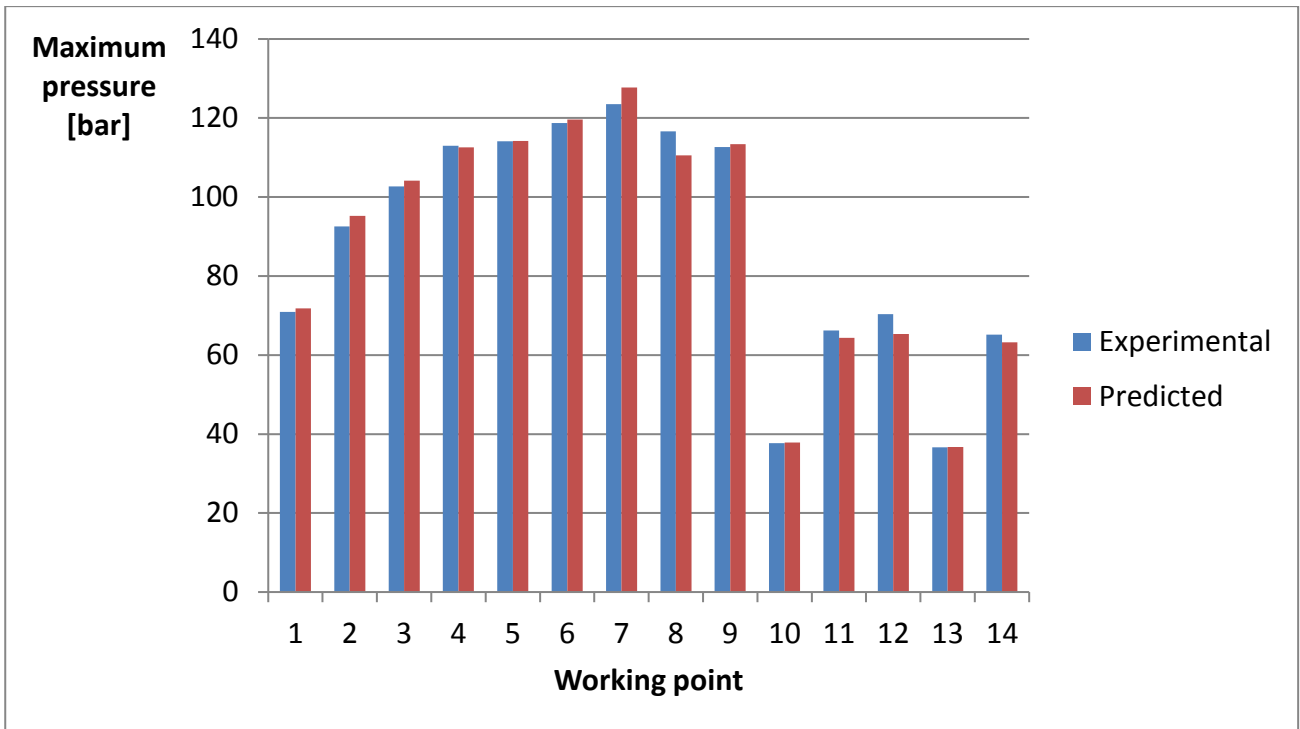


Figure 47. Maximum pressure deviations from experimental data for final  $c_{wc}$  and  $C_L$  values in form of histogram.

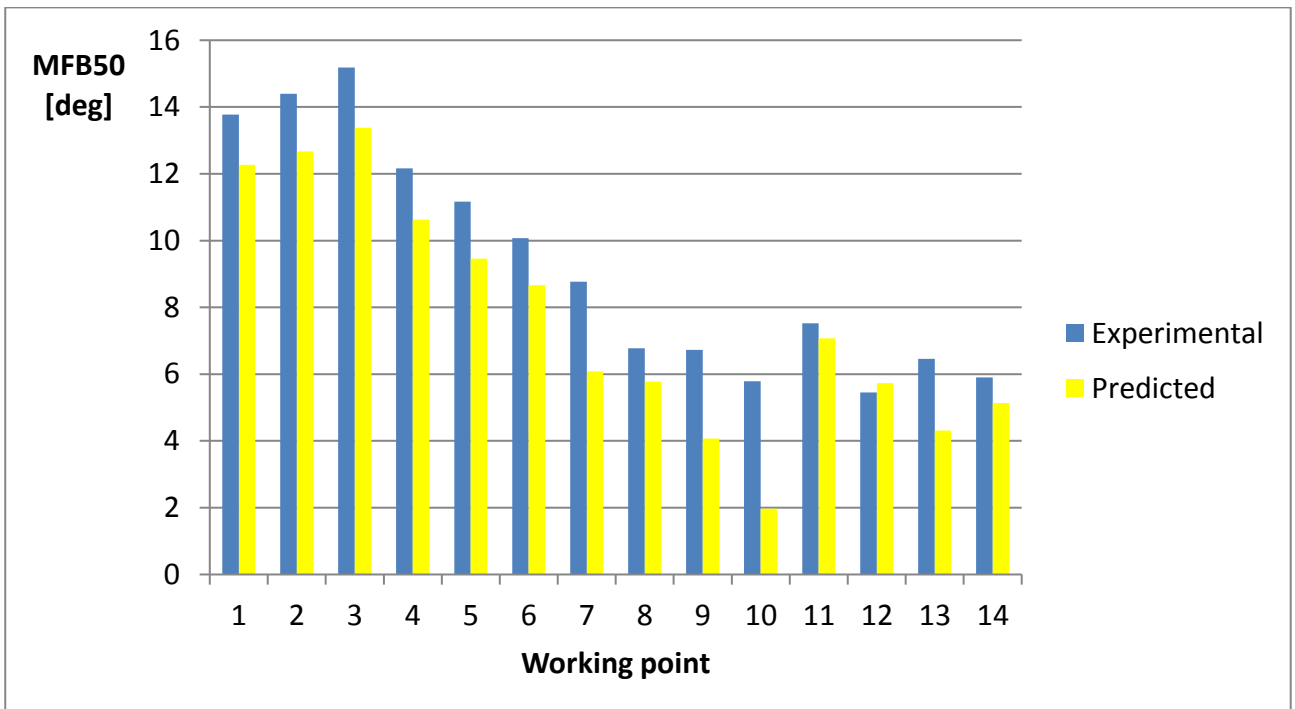


Figure 48. MFB50 deviations from experimental data for final  $c_{wc}$  and  $C_L$  values in form of histogram.

## 4.2 Calibration second phase (correlation phase)

In this phase, two mathematical functions which would give  $cwc$  and  $C_L$  values for whatever engine map working point are researched. Initial data for the investigation are five thermodynamical and functional parameters relative to the combustion start: in-cylinder pressure and unburned charge temperature at the spark timing  $p_{SA}$  and  $T_{SA}$ , engine speed  $n$ , burned residual mass fraction at cylinder cycle start  $x_{res}$  and relative air-to-fuel ratio  $RAFR$ . These factors are independent variables in the researched functions according to the following power laws:

$$cwc = a_1 \cdot p_{SA}^{a_2} \cdot T_{SA}^{a_3} \cdot n^{a_4} \cdot x_{res}^{a_5} \cdot RAFR^{a_6} \quad (44)$$

$$C_L = b_1 \cdot p_{SA}^{b_2} \cdot T_{SA}^{b_3} \cdot n^{b_4} \cdot x_{res}^{b_5} \cdot RAFR^{b_6} \quad (45)$$

where the arguments  $a_i$ ,  $b_i$  ( $i = 1 \div 6$ ) are the investigated parameters defining the inquired functions. The developed procedure to carry on this research is based on the least squares method; it finds  $a_i$ ,  $b_i$  factors, which allow to minimize the error between the projected power law results of (44) and (45) and the real  $cwc$  and  $C_L$  trends. In particular the Matlab function "*lsqcurvefit*" can be used for this purpose[61].

In Figure 49 the calibration second phase flow-chart is shown. Thermodynamical and functional parameters are collected for each working point from first phase simulation results correlated to final  $cwc$  and  $C_L$  values (Table 6). These input values (totally 70) together with their set of  $cwc$  (or  $C_L$ ) values are entered in Matlab code, which, as a calculation result, provides correlations (44) and (45) and automatically furnishes the *predicted* set of  $cwc$  (or  $C_L$ ) values. Matlab code elaborates also the comparison between input  $cwc$  vector (Table 6) with the predicted one, plotting a graph of the results and computing the correlation quality coefficients  $R$  and  $R^2$ .

Thus, at the end of Matlab run, it is possible to assess the correlation properties; in detail, when predicted values are too different from introduced ones (and consequently  $R^2$  is quite less than 1), the final correlation is not optimal.

There is the possibility to re-iterate the process by taking into account that, in some cases, a little variation in the value of  $cwc$  (or  $C_L$ ) can have great influence in mathematical calculation when introduced in Matlab code, but in GT-Power simulation it could not provide relevant impact on mass burned fraction and in-cylinder pressure curves. Therefore, the calibration first phase (*simulation phase*) is

re-started and new  $cwc$ (and/or  $C_L$ ) values are entered in GT-Power model; new  $cwc$  are chosen close to Matlab predicted ones, but still retaining a little difference from previous calibration resulting values of Table 6. If mass burned fraction and in-cylinder pressure curves computed by GT-Power still show a good match with experimental trends, the last new  $cwc$  and  $C_L$  vectors are then progressed to second phase into Matlab code.

Combined GT-Power and Matlab runs are worked out until the Matlab correlation quality coefficients  $R$  and  $R^2$  are close to 1 and at the same time input  $cwc$  and  $C_L$  vectors which have controlled as independent variables the least squares method, provide good fitting also in mass fraction burned and in-cylinder pressure trends with respect to experimental data. The whole procedure requires some re-iterations until overall targets are met.

In Table 8  $cwc$  and  $C_L$  vectors relative to first and last iterations are reported; the percentage variations on both parameters values are shown in last two columns. It is worth noticing that in some cases a decrease in  $cwc$  value can be compensated by an increase in  $C_L$  one and viceversa in order to best match mass fraction burned and in-cylinder pressure curves with experimental ones.

In Figure 50, experimental and predicted  $x_b$  and  $p$  curves for working points n.5, 6 and 11 (the same points of Figure 46) are illustrated with reference to last iteration of the calibration second phase. In Table 9 MFB50 and maximum pressure deviations from experimental data for all working points at the end of calibration second phase are reported.

In Table 10 final procedure results describing  $cwc$  and  $C_L$  correlations are indicated; in the same table, Matlab fitting quality coefficients  $R$  and  $R^2$  are also shown. In Figure 51 final correlation data can be visualized in graphs which compare input  $cwc$  values with predicted ones; in the ideal correlation case the graph should show a  $45^\circ$  line. In the same figure correlation results relative to first Matlab iteration are also reported in order to evaluate procedure overall evolution. In Figure 52 analogous correlation graphs are shown for parameter  $C_L$ .

Last calibration development phase is the GT-Power verification of correlations (44) and (45) described in Table 10. Therefore, Matlab predicted  $cwc$  and  $C_L$  values of last iteration in Figures 51 and 52 are tested into GT-Power model of the 14 selected working points; further, mass fraction burned and in-cylinder pressure trends are verified in comparison with experimental data. In Table 11 final Matlab predicted  $cwc$  and  $C_L$  vectors are listed; MFB50 and maximum pressure deviations are reported in the same table.

The verification provides good agreement with assumed targets as it can be visualized for working points n.5, 6 and 11 in Figure 53. Then, the whole calibration

is computed terminated. In the Annex A all simulations resulting plots for each calibration phase are reported.

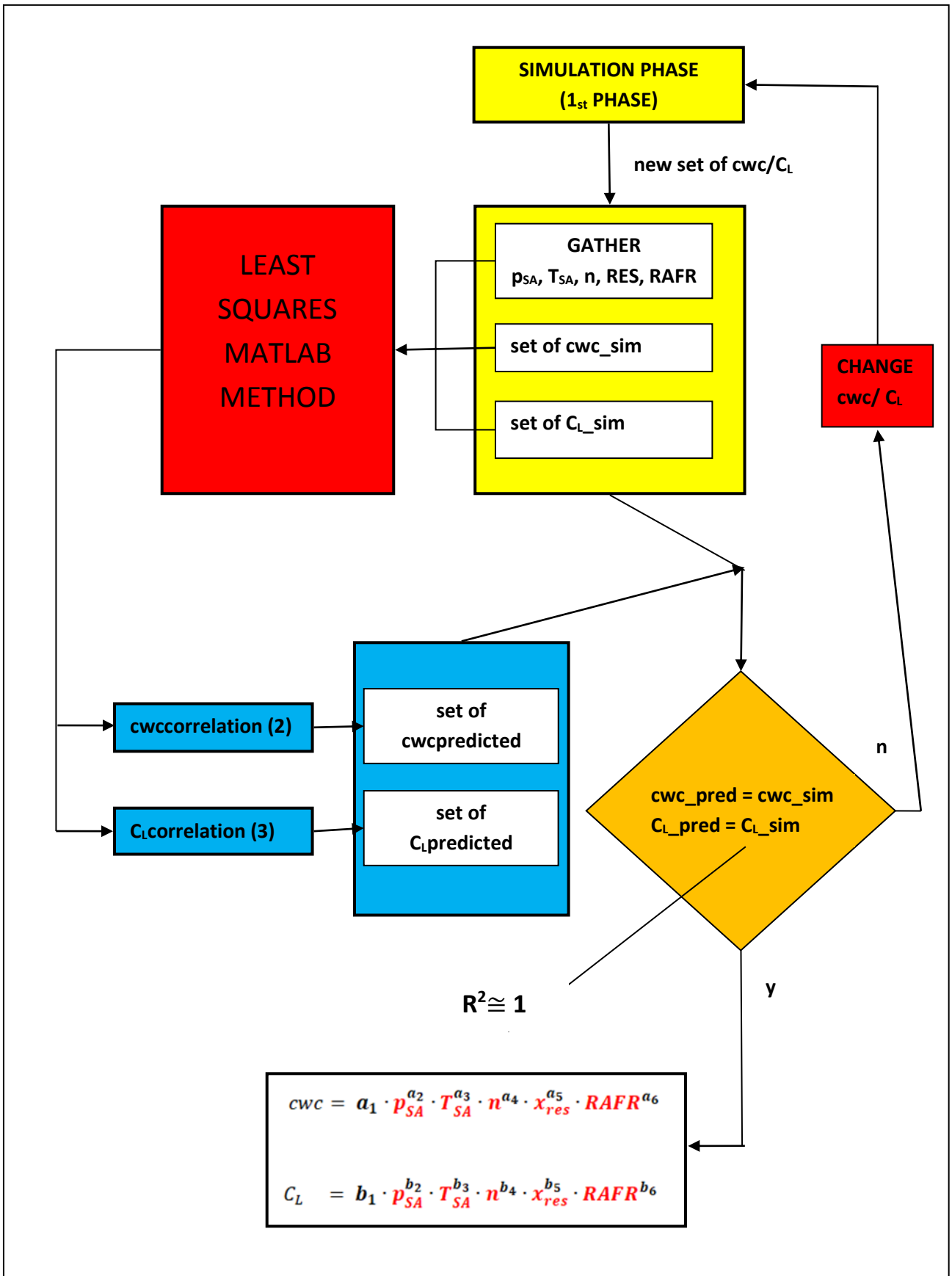


Figure 49. Calibration second phase flow-chart.

| <i>Working points</i> |           | <i>cwc</i><br><i>1<sup>st</sup> iteration</i> | <i>cwc</i><br><i>last iteration</i> | <i>C<sub>L</sub></i><br><i>1<sup>st</sup> iteration</i> | <i>C<sub>L</sub></i><br><i>last iteration</i> | <i>cwc</i><br><i>variation</i><br><i>[%]</i> | <i>C<sub>L</sub></i><br><i>variation</i><br><i>[%]</i> |
|-----------------------|-----------|---|-------------------------------------|---|---|--|--|
| <i>Full Load</i>      | <b>1</b>  | 0.4   | <b>0.36</b>                         | 0.044   | <b>0.044</b>                                  | -10.00                                       | 0.00   |
|                       | <b>2</b>  | 0.4   | <b>0.36</b>                         | 0.057   | <b>0.065</b>                                  | -10.00                                       | 14.04  |
|                       | <b>3</b>  | 0.475   | <b>0.38</b>                         | 0.075   | <b>0.073</b>                                  | -20.00                                       | -2.67  |
|                       | <b>4</b>  | 0.42  | <b>0.36</b>                         | 0.078   | <b>0.0725</b>                                 | -14.29                                       | -7.05  |
|                       | <b>5</b>  | 0.35  | <b>0.34</b>                         | 0.062   | <b>0.068</b>                                  | -2.86  | 9.68   |
|                       | <b>6</b>  | 0.3   | <b>0.31</b>                         | 0.075   | <b>0.0755</b>                                 | 3.33   | 0.67   |
|                       | <b>7</b>  | 0.25  | <b>0.282</b>                        | 0.06  | <b>0.065</b>                                  | 12.80  | 8.33   |
|                       | <b>8</b>  | 0.28  | <b>0.287</b>                        | 0.075   | <b>0.063</b>                                  | 2.50   | -16.00   |
|                       | <b>9</b>  | 0.25  | <b>0.257</b>                        | 0.08  | <b>0.069</b>                                  | 2.80   | -13.75   |
| <i>Partial Load</i>   | <b>10</b> | 0.8   | <b>0.82</b>                         | 0.012   | <b>0.012</b>                                  | 2.50   | 0.00   |
|                       | <b>11</b> | 0.75  | <b>0.6</b>                          | 0.037   | <b>0.033</b>                                  | -20.00                                       | -10.81   |
|                       | <b>12</b> | 0.65  | <b>0.5</b>                          | 0.028   | <b>0.026</b>                                  | -23.08                                       | -7.14  |
|                       | <b>13</b> | 0.45  | <b>0.37</b>                         | 0.016   | <b>0.015</b>                                  | -17.78                                       | -6.25  |
|                       | <b>14</b> | 0.55  | <b>0.4</b>                          | 0.027   | <b>0.026</b>                                  | -27.27                                       | -3.70  |

Table 8. Calibration second phase final *cwc* and *C<sub>L</sub>* values and relative difference with first phase.

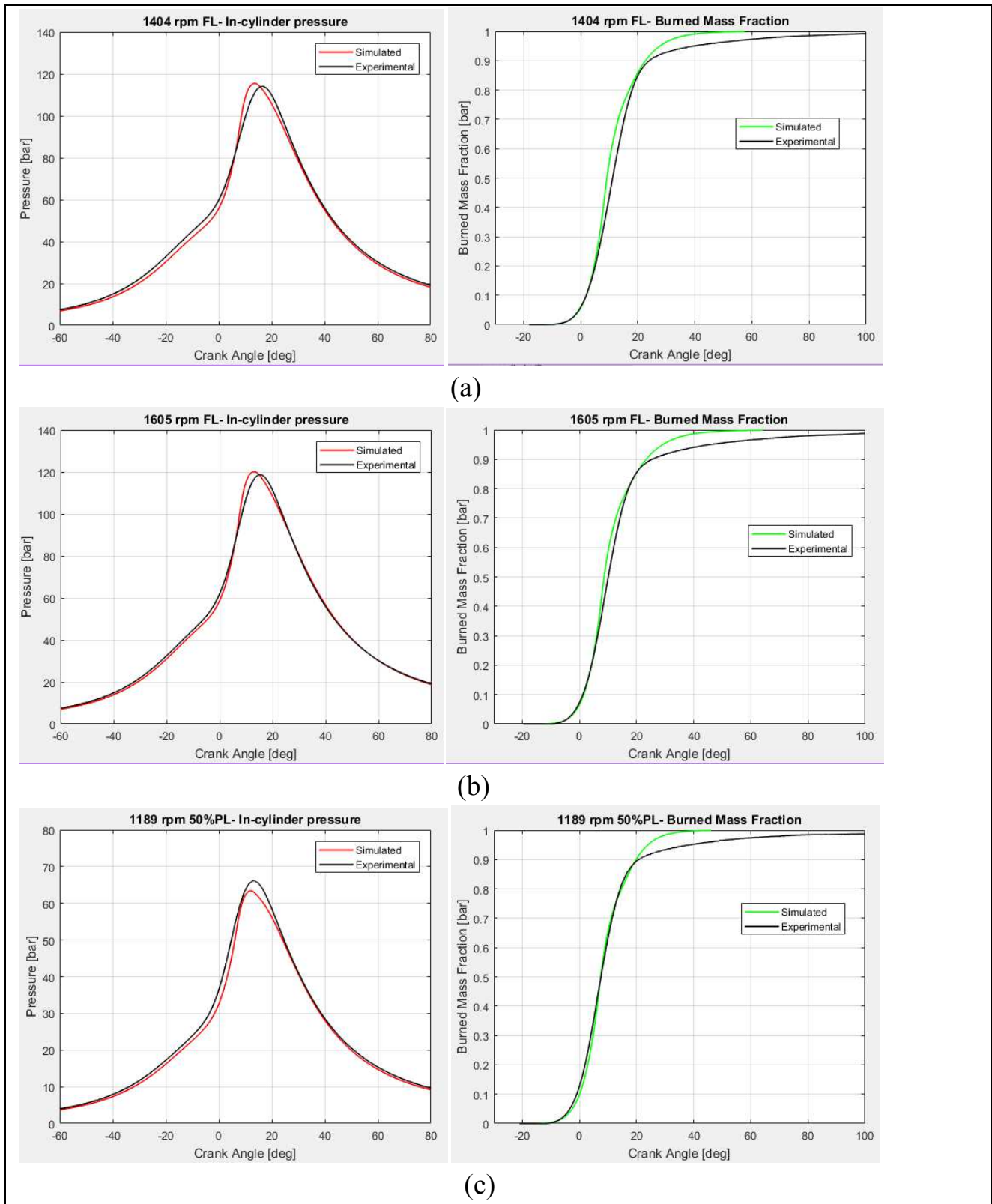


Figure 50. Predicted mass burned fraction and in-cylinder pressure curves correlative to second phase cwc and  $C_L$  values for a) working point n.5; engine speed 1404 rpm, full load ,b)working point n.6; engine speed 1605 rpm, full load, c) working point n.11; engine speed 1189 rpm, 50% load. In black line experimental data.

| <i>Calibration Second Phase</i> |           |                          |                          |                           |                           |                           |                          |
|---------------------------------|-----------|--------------------------|--------------------------|---------------------------|---------------------------|---------------------------|--------------------------|
| <b>Working points</b>           |           | <i>p_maxexp</i><br>[bar] | <i>p_maxsim</i><br>[bar] | <i>p_max error</i><br>[%] | <i>MFB50 exp</i><br>[deg] | <i>MFB50 sim</i><br>[deg] | <i>MFB50 error</i> [deg] |
| <i>Full Load</i>                | <b>1</b>  | 70.9404                  | <b>72.8375</b>           | 2.67                      | 13.7776                   | <b>12.332</b>             | -1.4456                  |
|                                 | <b>2</b>  | 92.5842                  | <b>96.8923</b>           | 4.65                      | 14.394                    | <b>12.2673</b>            | -2.1267                  |
|                                 | <b>3</b>  | 102.701                  | <b>103.871</b>           | 1.14                      | 15.1866                   | <b>13.4801</b>            | -1.7065                  |
|                                 | <b>4</b>  | 112.979                  | <b>110.45</b>            | -2.24                     | 12.1608                   | <b>10.8887</b>            | -1.2721                  |
|                                 | <b>5</b>  | 114.138                  | <b>115.567</b>           | 1.25                      | 11.1635                   | <b>9.16271</b>            | -2.00079                 |
|                                 | <b>6</b>  | 118.729                  | <b>120.205</b>           | 1.24                      | 10.0733                   | <b>8.6166</b>             | -1.4567                  |
|                                 | <b>7</b>  | 123.54                   | <b>131.533</b>           | 6.47                      | 8.76845                   | <b>5.74426</b>            | -3.02419                 |
|                                 | <b>8</b>  | 116.659                  | <b>108.207</b>           | -7.25                     | 6.77405                   | <b>6.34769</b>            | -0.42636                 |
|                                 | <b>9</b>  | 112.693                  | <b>112.553</b>           | -0.12                     | 6.73023                   | <b>4.54433</b>            | -2.1859                  |
| <i>Partial Load</i>             | <b>10</b> | 37.7181                  | <b>38.106</b>            | 1.03                      | 5.78687                   | <b>2.12777</b>            | -3.6591                  |
|                                 | <b>11</b> | 66.185                   | <b>63.4638</b>           | -4.11                     | 7.52139                   | <b>7.42011</b>            | -0.10128                 |
|                                 | <b>12</b> | 70.3894                  | <b>65.3996</b>           | -7.09                     | 5.44717                   | <b>6.00853</b>            | 0.56136                  |
|                                 | <b>13</b> | 36.6559                  | <b>35.4297</b>           | -3.35                     | 6.46161                   | <b>4.57368</b>            | -1.88793                 |
|                                 | <b>14</b> | 65.136                   | <b>61.7399</b>           | -5.21                     | 5.90349                   | <b>5.29738</b>            | -0.60611                 |

Table 9. MFB50 and maximum pressure deviations from experimental data for calibration final second phase cwc and  $C_L$  values.

|   |  |
|---|--|
| <b><i>cwc final correlation</i></b>   |  |
| $cwc = 2.58 \cdot 10^5 \cdot p_{SA}^{0.13} \cdot T_{SA}^{-1.72} \cdot n^{-0.46} \cdot x_{res}^{-0.51} \cdot RAFR^{-11.5} \quad (4)$ |  |
| <b>R = 0.9977      R<sup>2</sup> = 0.9955</b>   |  |
| <b><i>C<sub>L</sub> final correlation</i></b>   |  |
| $C_L = 2.2 \cdot 10^{-10} \cdot p_{SA}^{1.55} \cdot T_{SA}^{1.27} \cdot n^{0.63} \cdot x_{res}^{1.3} \cdot RAFR^{-1.34} \quad (5)$  |  |
| <b>R = 0.9984      R<sup>2</sup> = 0.9968</b>   |  |

Table 10. Calibration second phase final cwc and C<sub>L</sub> correlations.

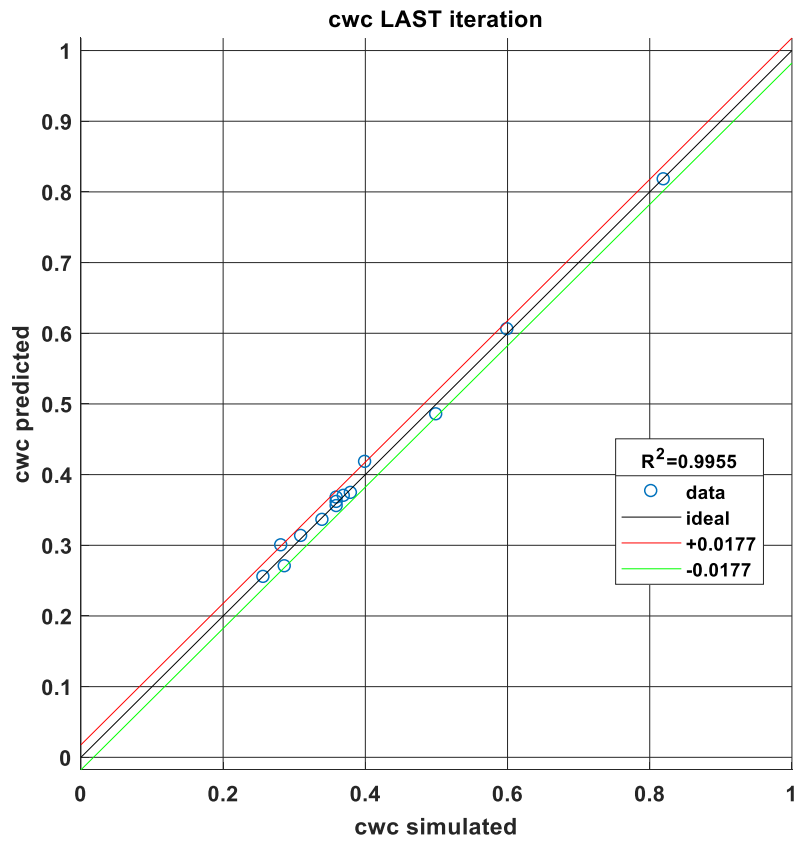
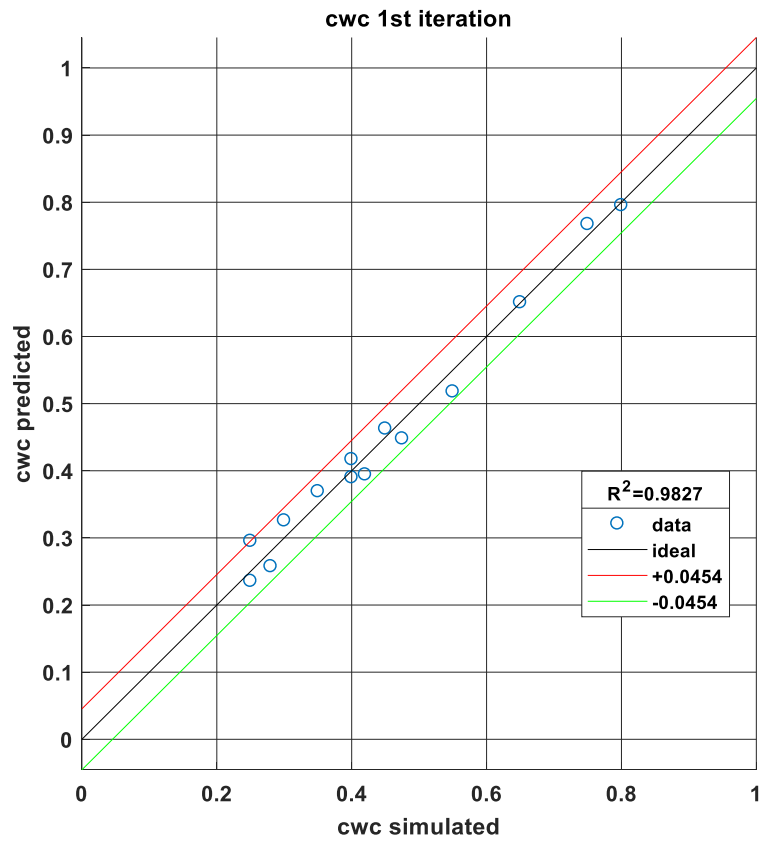


Figure 51. cwc first and last correlation graphs.

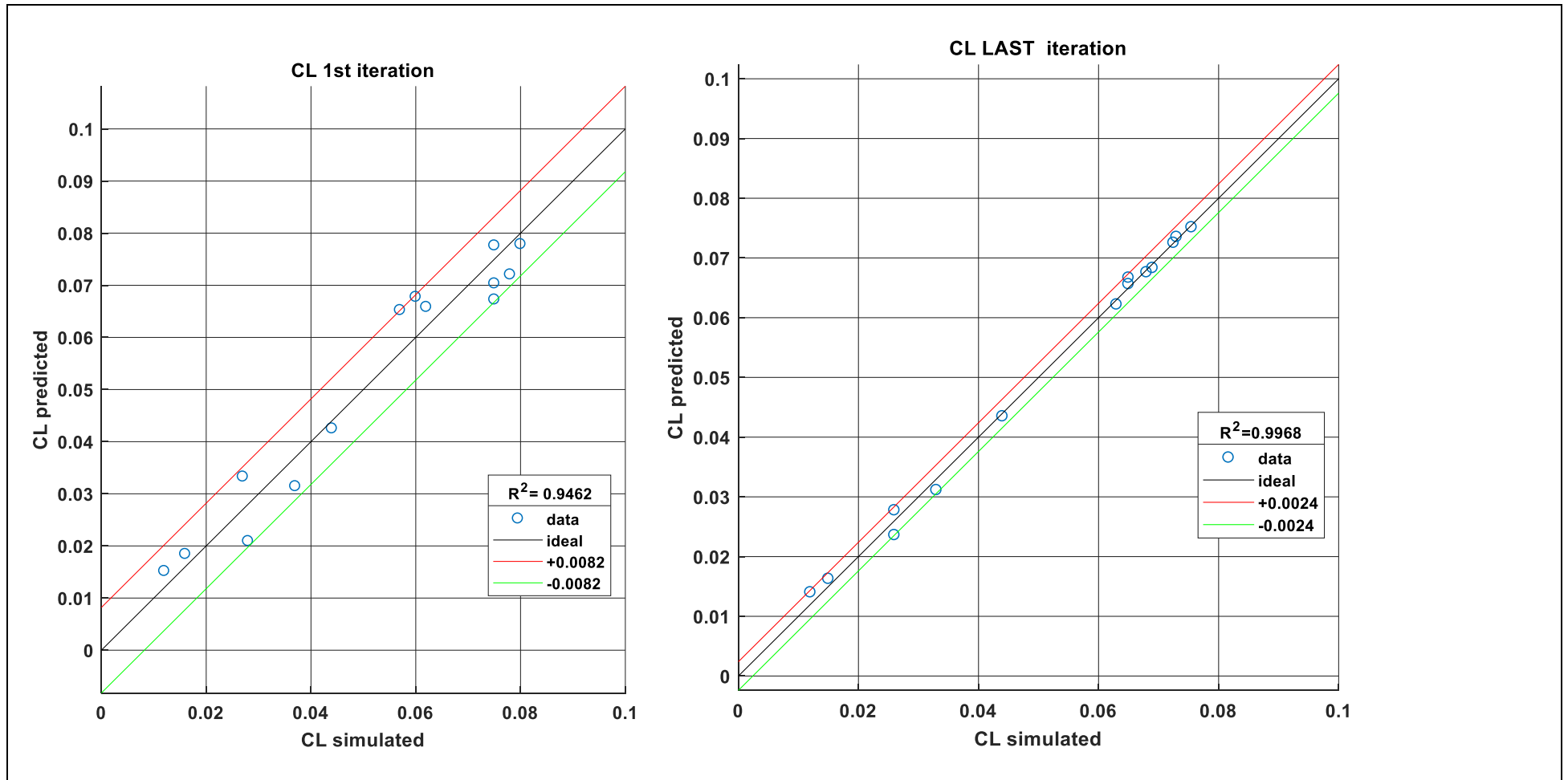


Figure 52.  $C_L$  first and last correlation graphs.

| <b>Calibration last verification</b> |           |                |                              |  |  |  |                            |                            |                              |
|--------------------------------------|-----------|----------------|------------------------------|--|--|--|----------------------------|----------------------------|------------------------------|
| <b>Working points</b>                |           | <b>predcwc</b> | <b>pred <math>C_L</math></b> | <b><math>p_{maxexp}</math><br/>[bar]</b> | <b><math>p_{maxsim}</math><br/>[bar]</b> | <b><math>p_{max}</math><br/>error[%]</b> | <b>MFB50 exp<br/>[deg]</b> | <b>MFB50 sim<br/>[deg]</b> | <b>MFB50<br/>error [deg]</b> |
| <b>Full load</b>                     | <b>1</b>  | 0.3672         | 0.0435                       | 70.9404                                  | <b>72.0212</b>                           | 1.52                                     | 13.7776                    | <b>12.4316</b>             | -1.346                       |
|                                      | <b>2</b>  | 0.3611         | 0.0656                       | 92.5842                                  | <b>97.0212</b>                           | 4.79                                     | 14.394                     | <b>12.2401</b>             | -2.1539                      |
|                                      | <b>3</b>  | 0.3739         | 0.0735                       | 102.701                                  | <b>103.922</b>                           | 1.19                                     | 15.1866                    | <b>13.4588</b>             | -1.7278                      |
|                                      | <b>4</b>  | 0.3552         | 0.0725                       | 112.979                                  | <b>110.393</b>                           | -2.29                                    | 12.1608                    | <b>10.8912</b>             | -1.2696                      |
|                                      | <b>5</b>  | 0.3357         | 0.0676                       | 114.138                                  | <b>115.031</b>                           | 0.78                                     | 11.1635                    | <b>9.20562</b>             | -1.95788                     |
|                                      | <b>6</b>  | 0.313          | 0.0751                       | 118.729                                  | <b>120.15</b>                            | 1.20                                     | 10.0733                    | <b>8.63207</b>             | -1.44123                     |
|                                      | <b>7</b>  | 0.2997         | 0.0667                       | 123.54                                   | <b>132.196</b>                           | 7.01                                     | 8.76845                    | <b>5.61571</b>             | -3.15274                     |
|                                      | <b>8</b>  | 0.27           | 0.0622                       | 116.659                                  | <b>107.414</b>                           | -7.92                                    | 6.77405                    | <b>6.42303</b>             | -0.35102                     |
|                                      | <b>9</b>  | 0.255          | 0.0683                       | 112.693                                  | <b>112.52</b>                            | -0.15                                    | 6.73023                    | <b>4.57915</b>             | -2.15108                     |
| <b>Partial load</b>                  | <b>10</b> | 0.8175         | 0.014                        | 37.7181                                  | <b>38.8789</b>                           | 3.08                                     | 5.78687                    | <b>1.53545</b>             | -4.25142                     |
|                                      | <b>11</b> | 0.6054         | 0.0311                       | 66.185                                   | <b>62.9542</b>                           | -4.88                                    | 7.52139                    | <b>7.60281</b>             | 0.08142                      |
|                                      | <b>12</b> | 0.485          | 0.0236                       | 70.3894                                  | <b>64.4083</b>                           | -8.50                                    | 5.44717                    | <b>6.36716</b>             | 0.91999                      |
|                                      | <b>13</b> | 0.3697         | 0.0163                       | 36.6559                                  | <b>36.3338</b>                           | -0.88                                    | 6.46161                    | <b>4.27368</b>             | -2.18793                     |
|                                      | <b>14</b> | 0.4177         | 0.0277                       | 65.136                                   | <b>62.6079</b>                           | -3.88                                    | 5.90349                    | <b>5.04427</b>             | -0.85922                     |

Table 11. Last iteration Matlab predicted cwc and  $C_L$  values with MFB50 and maximum pressure deviations from experimental data.

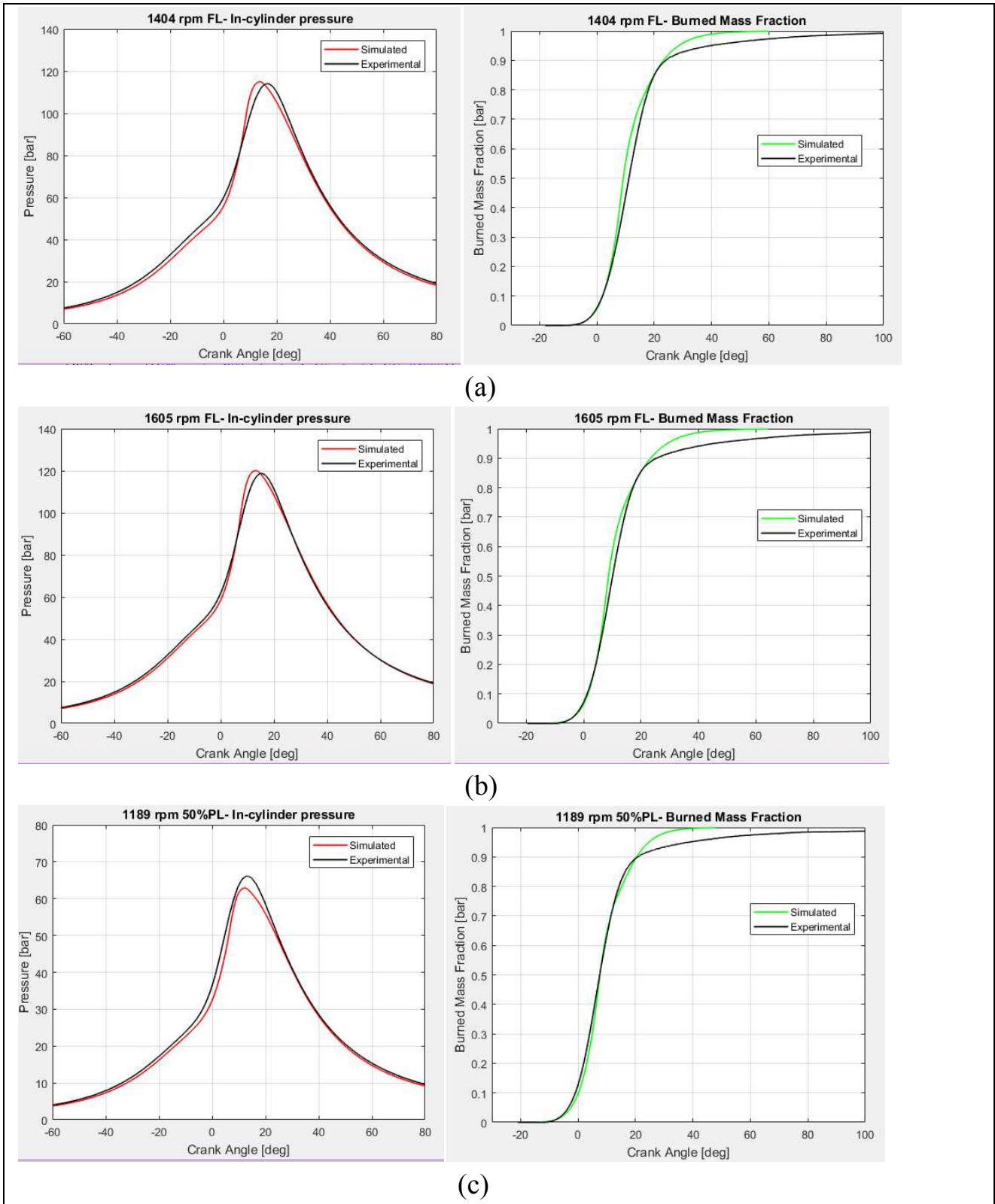


Figure 53. Predicted mass burned fraction and in-cylinder pressure curves correlative to last Matlab predicted  $c_w$  and  $C_v$  values for a) working point n.5; engine speed 1404 rpm, full load ,b)working point n.6; engine speed 1605 rpm, full load, c) working point n.11; engine speed 1189 rpm, 50% load. In black line experimental data.

# 5. Numerical prediction for exhaust temperature control

---

## 5.1 CORE Collaborative Project

In a period which lasted from 2012 and 2015, Fiat Research Center (CRF) and Politecnico di Torino carried out a research activity within the CORE Collaborative Project of the European Community (VII Framework Programme)[33]. The project title has been "CO<sub>2</sub> Reduction for long distance transport" and it involved 16 partners from truck manufacturers, automotive industries and universities[33,62].

The main objective has been the demonstration of a substantial reduction of CO<sub>2</sub> emissions through improved powertrain efficiency for long haul applications, with technologies having the potential to be implemented in production around 2020. The main focus areas are advanced engine concepts featuring turbocharger systems, Variable Valve Actuation (VVA), reduced friction, aftertreatment concerning low temperature range. In addition the project involved the use of hybridization and natural gas[62].

Cursor 8 NG engine prototype has been tested for the peculiar project of the integration of Variable Valve Actuation technology on HD engine platform realizing a support to experimental evaluation. It has been necessary to include in the valve kinematic chain the hydraulic control volume; valve lift strategy is controlled by a solenoid valve governed by dedicated electronic units and by hydraulic fluid that is lubricant oil. The solution was to adopt a single control unit for each cylinder[62]. The second part of the project consisted in performing experimental tests with innovative combustion approaches allowed by VVA system in order to measure the fuel consumption saving due to pumping friction reduction and the impact on thermal NG engine state[33,62].

Interestingly, first test bench activity result was CO<sub>2</sub> saving of about 2% at high load and high engine revolution and of about 10% at lower load and engine revolution[62]. In addition it was assessed that VVA affects exhaust pollutants amount, so that compromise between THC emission, performance and fuel consumption had to be found in successive calibration phase[33,62]. As a consequence, focus converged into the development of advanced air management and

dedicated combustion control strategies, whose investigation constitutes a relevant path for present research[33].

As an outcome, present numerical investigation develops a parametric study regarding a retarded combustion strategy for the optimization of the catalyst warm-up[33].

## 5.2 Numerical prediction for exhaust temperature control

As far as concerns the catalyst warm-up phase, it is suitable for NG fuel an exhaust gas temperature of above 850K to effectively oxidize methane[63].

The higher exhaust temperature can be obtained by retarding the spark timing and then the whole combustion phase. In particular the parameter that is analysed in this study to control combustion timing is 50% burned mass fraction angle, namely MFB50; it will be higher in value when combustion shifts towards in the engine cycle.

Such combustion management aims at correlating the MFB50 sweep to a simultaneous EIVC angle changing. Results are resumed in a iso-curve 2D graph, which represents different operating conditions of a working point by means of *x-axis* (EIVC angle) and *y-axis* (MFB50 angle); the *iso-curves* let evaluate a third engine parameter which, in a first approach, is the catalyst inlet temperature (outlet of the turbine)[33].

Each working point must maintain the same brake torque during condition parameters variation; then a change in the waste gate diameter is imposed so as to modify the boost pressure and adapting the engine inlet charge to the desired constant brake torque.

Operatively, for each specific couple of parameters ( EIVC angle about the reference one and MFB50 angle) a steady-state GT-Power simulation is run, simultaneously controlling the waste gate diameter in order to reach a reference brake torque value equal for all imposed conditions at a defined working point.

At this scope, two GT-Power tools are used, which are embedded into the simulation; the first is the Optimizer interface and the second is a computational PID controller added to the engine model. They have been described in the subparagraph in Chapter 2 ("GT-Power tested engine model").

Working points studied are reported in Table 12, in which strategic MFB50 and EIVC angle values are also illustrated.

|  | MFB50 sweep [deg]                | relative EIVC angle sweep [deg] |
|--|----------------------------------|---------------------------------|
| Load= 50%FL (600Nm)<br>Speed= 1200 rpm | 2.04/ 4.44/ 6.7/ 11.07           | 40/ 45/ 50/ 55                  |
| Load= 50%FL (615Nm)<br>Speed=1600 rpm  | 1.73/ 4.65/ 7.51/10.63/<br>13.45 | 20/ 25/ 30/ 35                  |

Table 12. Operative parameters of numerical analysis[30]

Iso-curves graphs are determined in order to analyse the temperatures at the outlet and inlet of the turbine, the boost pressure and the fuel consumption. In Figures 54 and 55 the graphs relative to temperature at the outlet of the turbine for both the working points are reported, while in Figures 56 and 57 the fuel consumption iso-curves are shown. All resulting graphs are illustrated in Annex B.

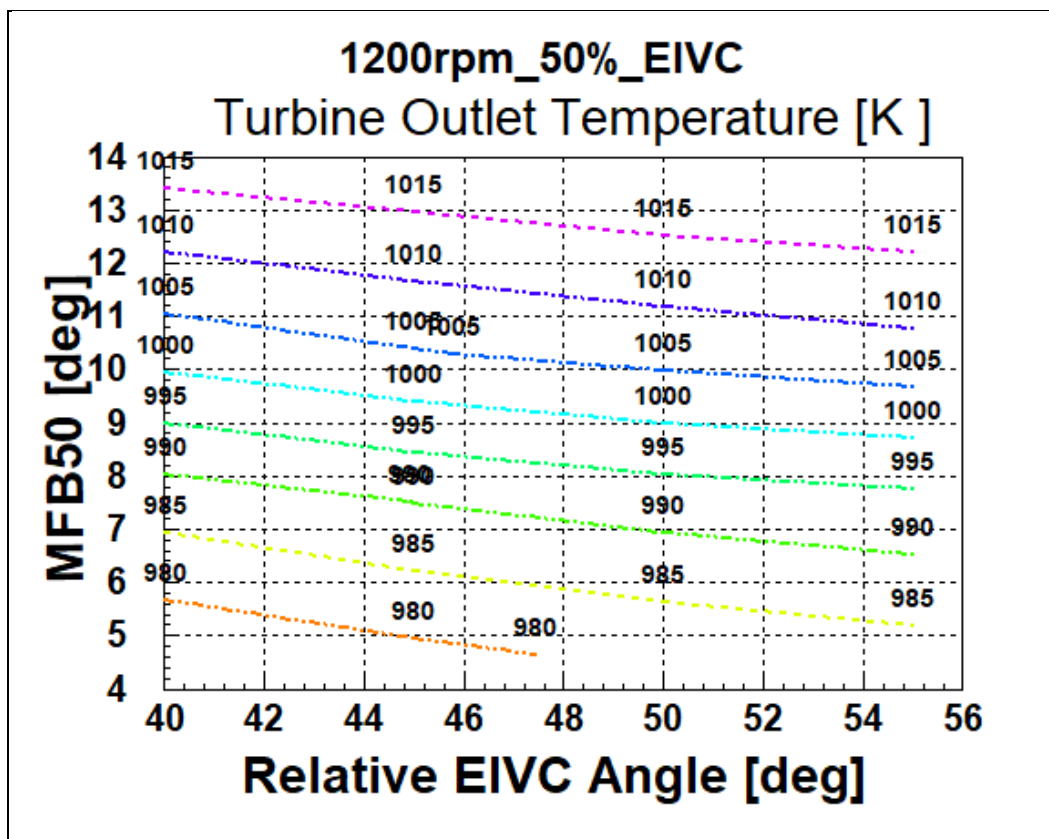


Figure 54. Iso-curves of temperature at the turbine outlet for 1200 rpm and 50% load.

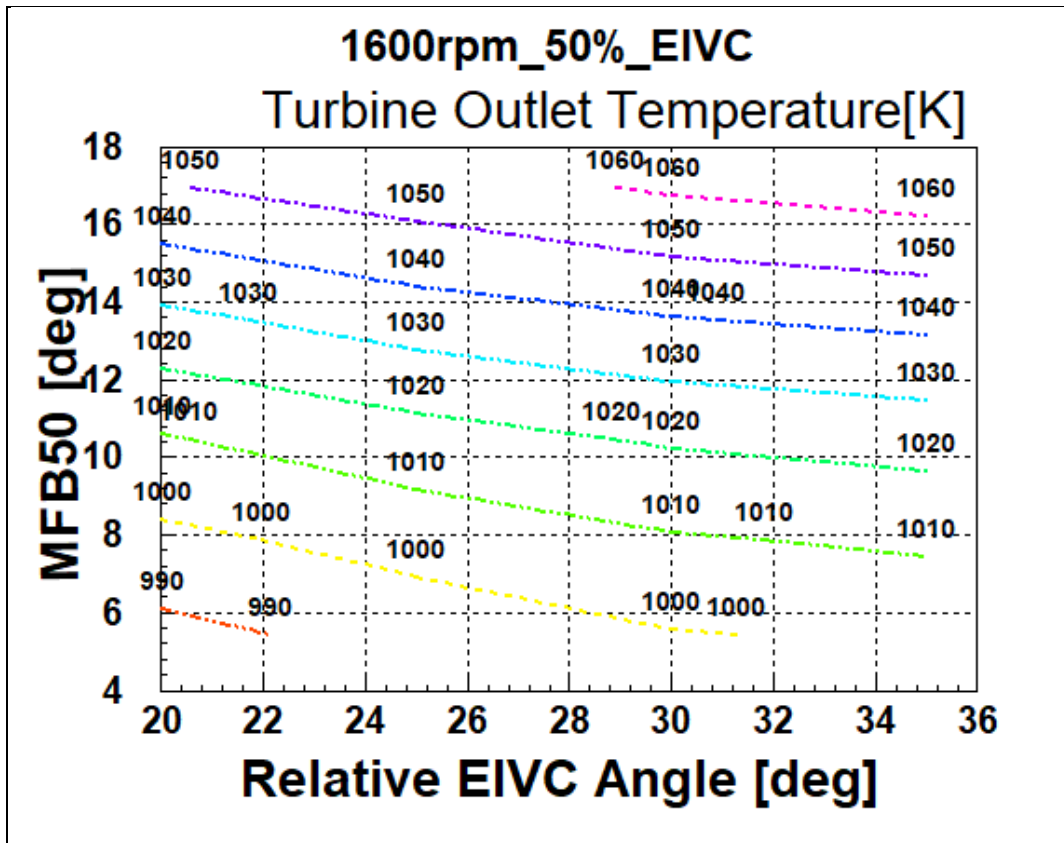


Figure 55. Iso-curves of temperature at the turbine outlet for 1600 rpm and 50% load.

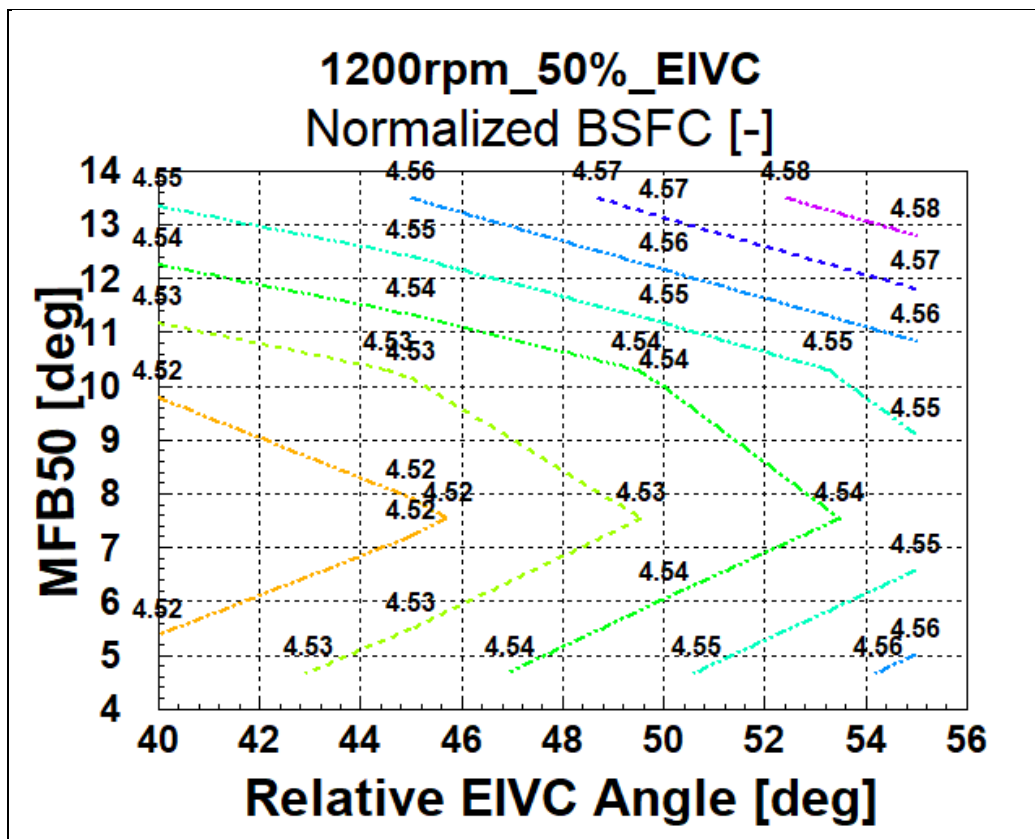


Figure 56. Fuel consumption iso-curves for 1200 rpm and 50% load.

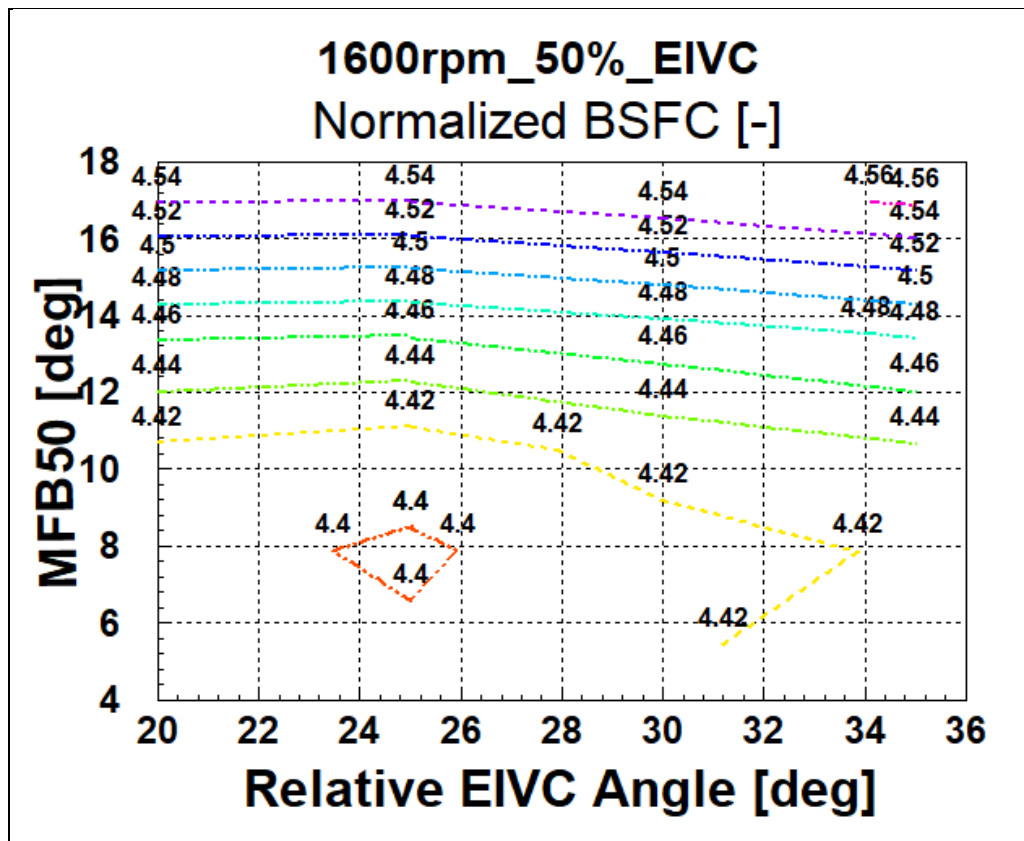


Figure 57. Fuel consumption iso-curves for 1600 rpm and 50% load.

As combustion is retarded, exhaust gas temperatures increase. As an outcome from the charts, also the retard of EIVC angle provides a rise in the exhaust temperature. While the brake torque is kept constant inside any chart, when the EIVC angle is posticipated, the boost pressure correspondingly decreases; this fact can give rise to a lower turbine back pressure and hence to a faster combustion diminishing the effect of exhaust gas temperature augmentation[33].

The turbine outlet temperature is directly related to the one at the catalyst inlet, affecting its thermal regime. Taking into account that the optimal temperature for catalyst to oxidize methane is above 850K, as it is shown from the chart at 1200 rpm minimum exhaust temperature is about 975K for advanced EIVC and combustion timings. On the other hand increasing EIVC angles and MFB50 values allows a gas temperature of about 1020K[33,63].

Correspondingly, when maximum temperatures are reached, the fuel consumption is higher; for a constant EIVC angle the BSFC trend with respect to MFB50 follows the pattern of the torque as function of the spark timing. As a consequence, the MBT (Maximum Brake Torque) timing is characterized by the minimum BSFC.

A compromise may be possible by considering specific strategies of temporary operation, in which EIVC and MFB50 timings are retarded, with minor penalties in terms of fuel consumption[33].

### 5.3 Results about other HD NG engines for combustion retardation

Shu et al.(2018,[64]) have referred that in heavy-duty CNG engine ignited by means of diesel pilot (dual fuel and originally only diesel engine with compression ratio of 17) retarded combustion has been tested by varying the APID (Advance Pilot Injection Degree) and brake specific emissions have been evaluated[64]. NG is injected into the intake port of engine at the pressure of about 8 bar on lean operation. In Table 13 main engine parameters are reported. Turbocharger features the waste gate valve and intercooler between compressor and intake manifold[64].

| <b>NG Dual Fuel Engine parameters</b> |                |
|---------------------------------------|----------------|
| <b>Displacement(L)</b>                | 9,726          |
| <b>Bore[mm]</b>                       | 126            |
| <b>Stroke[mm]</b>                     | 130            |
| <b>Maximum Power[kW@rpm]</b>          | 247@1900       |
| <b>Maximum Torque[Nm@rpm]</b>         | 1550@1200-1500 |

Table 13 . Main dual fuel engine parameters in [64].

The study has involved low engine speed (1000 rpm) and low load (25% partial load) with a APID variation between 6°CA to 16°CA.

Retarded combustion has revealed the possibility to complete THC oxidation into the exhaust pipe becoming the post-combustion serious. Thus brake specific THC are lower in the case of 6° CA APID in comparison to more advanced pilot injection timings. In Figure 58 the mean in-cylinder temperature at different APID is shown in function of crank angle degrees[64].

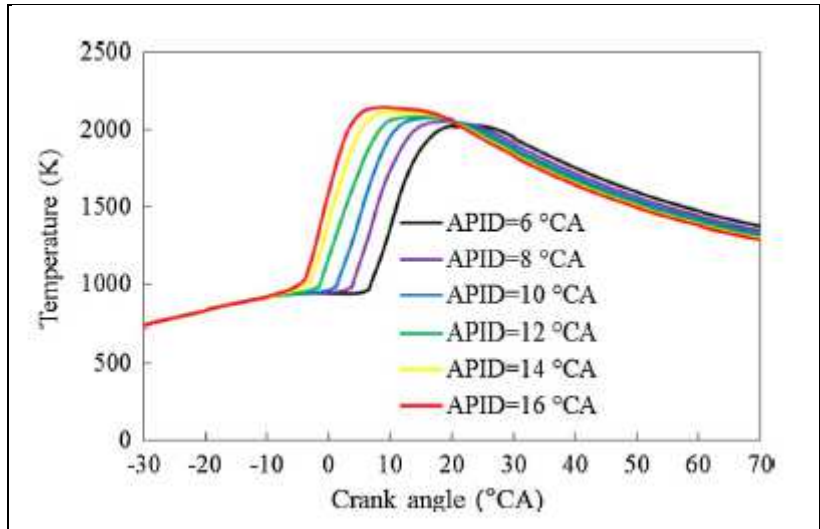


Figure 58. Mean in-cylinder temperature at different APID (CFD results)in [64].

In Figure 59 the temperature enhancement in the combustion chamber after pilot injection timing (API) is shown for different injection degrees; in the case of retarded combustion higher temperatures characterize expansion phase[64].

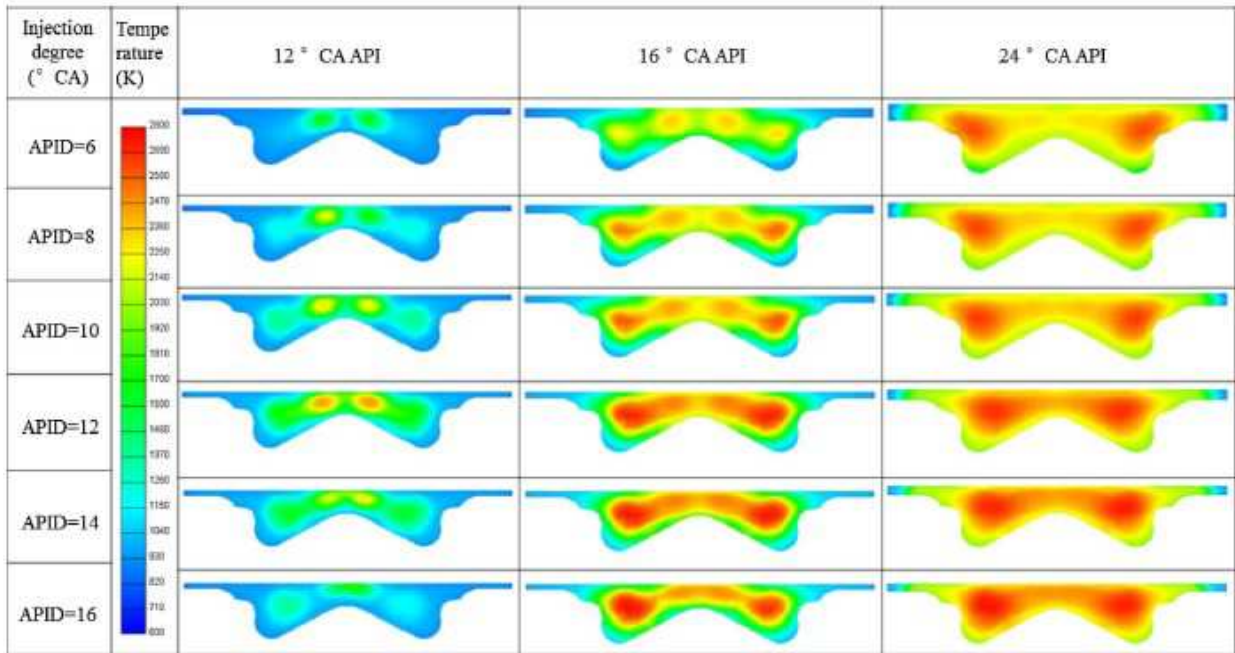


Figure 59. Combustion chamber temperature distribution for different APID after pilot injection timing (CFD results)in [64].

In Figure 60 brake specific THC emissions, which primarily are composed of methane (about 90%), are reported in relation to the combustion retardation[64]

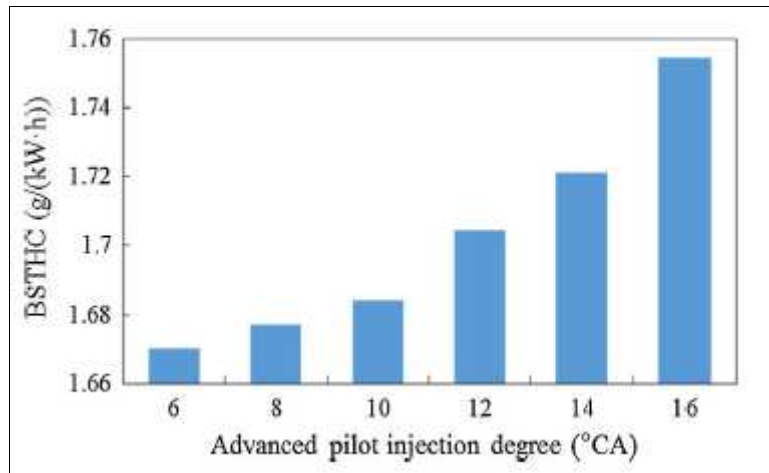


Figure 60. Brake specific THC emissions versus pilot injection timing (tested data)in [64]

Moreover, due to lower average in-cylinder temperature in the combustion phase (Figure 58), a lower APID allows to reduce brake specific NO<sub>x</sub> emissions, as it is illustrated in Figure 61[64].

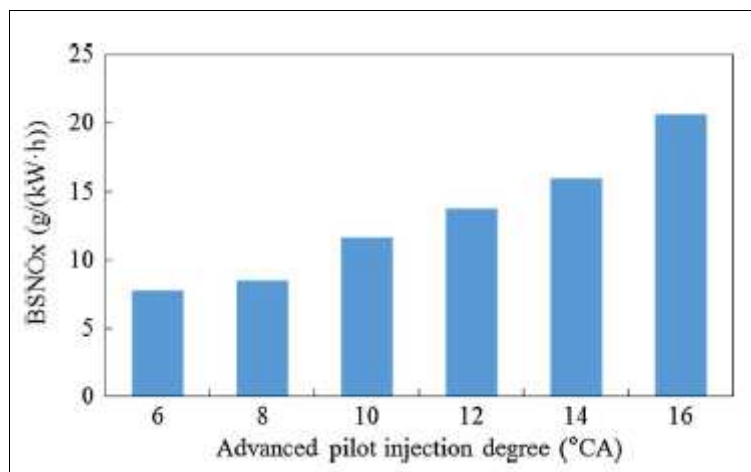


Figure 61. Brake specific NO<sub>x</sub> emissions versus APID (tested data)[64]

Zhang et al.(2016,[65]) have investigated a heavy-duty CNG engine which operates in stoichiometric conditions referring to combustion and emissions analysis. Their study has highlighted the adoption of retarded combustion at lower engine speeds and loads in order to enhance conversion efficiency of TWC. Main engine parameters are reported in Table 14[65].

| Engine Parameters             | Specifications                                |
|-------------------------------|---|
| Engine type                   | Spark-ignition, 6-cylinder, in line, 4-stroke |
| Charged method                | Turbocharged and intercooled                  |
| Bore/Stroke                   | 126 mm/155 mm                                 |
| Displacement                  | 11.6 L  |
| Rated speed                   | 1800 rpm                                      |
| Rated power                   | 260 kW  |
| Idle speed                    | 700 rpm                                       |
| Valve number of each cylinder | 4   |
| Compression ratio             | 11.5:1  |
| Piston cavity shape           | Re-entrant type                               |
| After-treatment               | TWC   |

Table 14. Specifications of tested engine in [65].

In Figure 62 contour map of spark timing over the engine map tested field is reported; in the region of low engine speed and low loads, minimum spark advance is set up such as to warm-up exhaust gases and correspondingly the inlet catalyst temperature. In fact, Figure 63 illustrates inlet TWC temperatures over the whole engine map, in which the coldest condition is about 413°C[65].

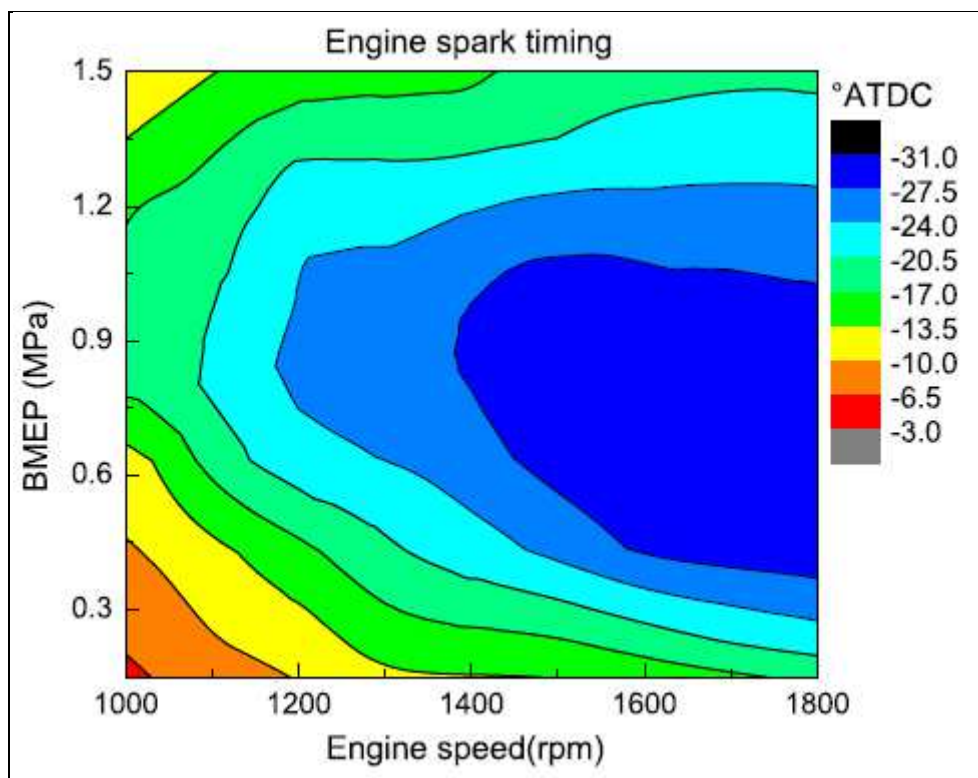


Figure 62. Contour map of spark timing in [65].

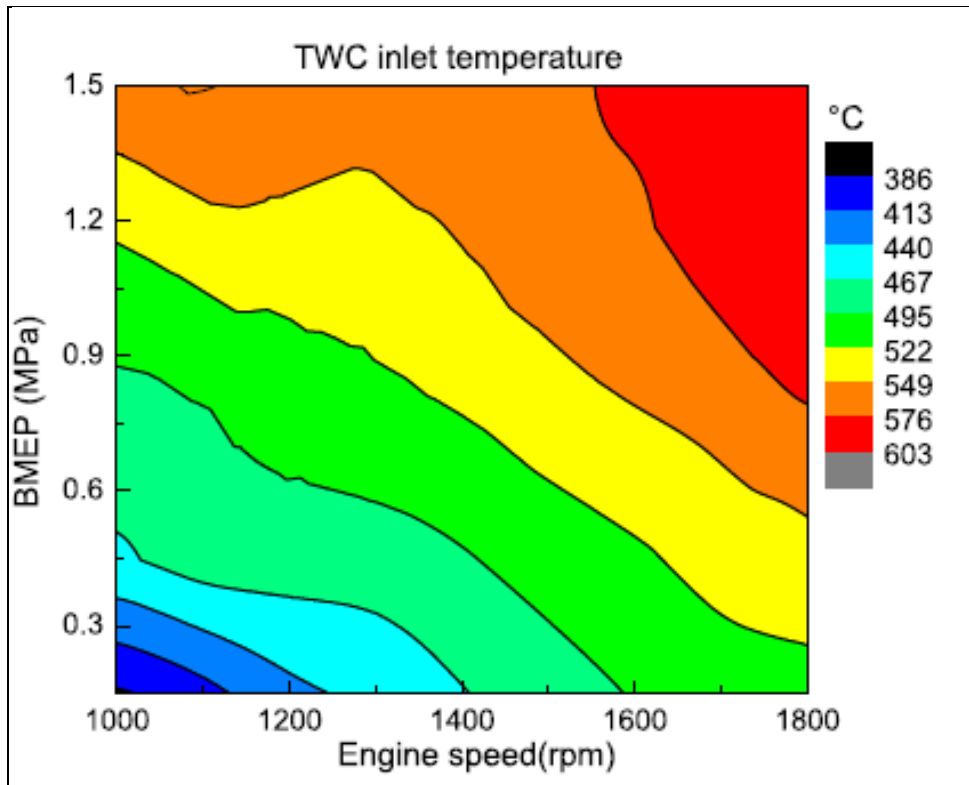


Figure 63. Contour map of TWC inlet temperature in [65].

With the combustion retardation, total HC conversion efficiency is kept higher in engine map regions in which exhaust gases temperatures are lower, as it can be seen in Figure 64 [65].

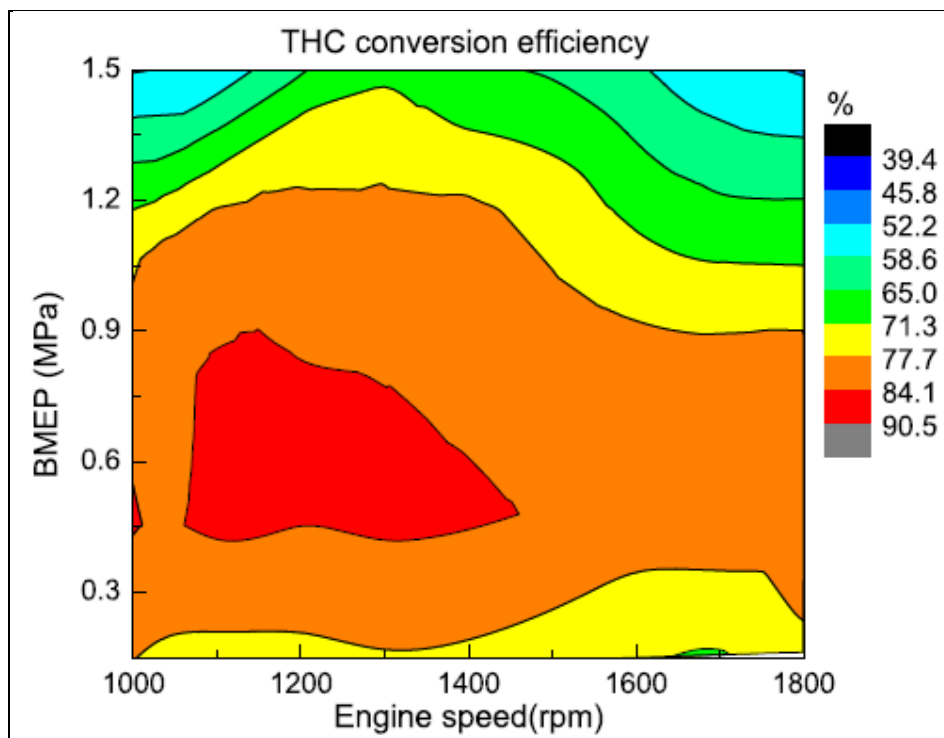


Figure 64. Contour map of THC conversion efficiency in [65].

## 6. Conclusions

---

Natural gas as Low Carbon Alternative fuel can allow to meet requirements about CO<sub>2</sub> emissions within 2020; in this contest Horizon 2020 EU Research and Innovation programme supports GASON Project (May 2015-October 2018) with the aim to develop advanced CNG only, mono fuel engines able to comply with the 2025-2030 emission targets.

The project claims 20% CO<sub>2</sub> emissions reduction with regard to current best in class CNG vehicle segment by segment. It aims also to guarantee a low fuel consumption in real driving conditions[66].

In Figure 65 GasOn CNG Project target is illustrated in comparison with engine conventional fuels, in which the reference condition is indicated by gasoline engine. It can be seen that advanced CNG technology is highlighted as relevant part of the project development[66].

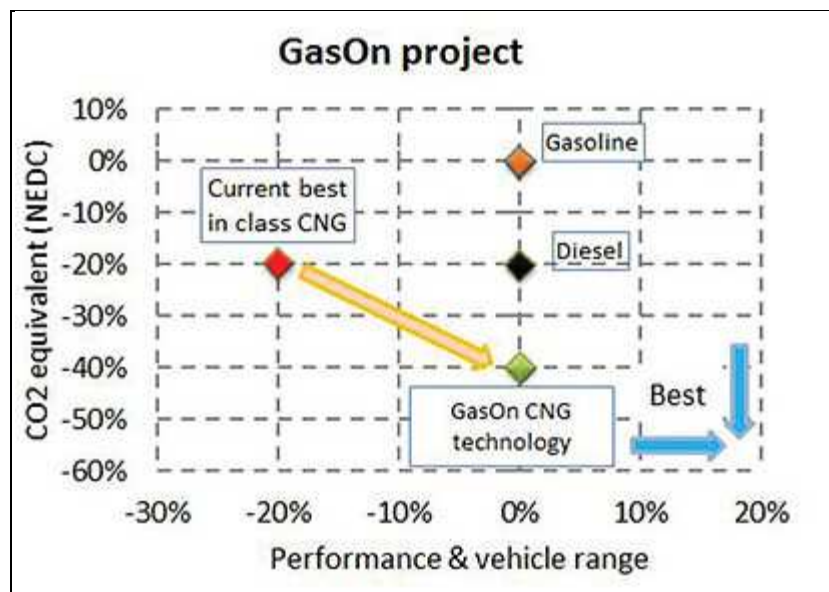


Figure 65. Gason Project target illustration[66].

In particular, first important step is the implementation of CNG Direct Injection (DI) in demonstrator engines integrated with other parallel technology ways as variable valve actuation (VVA), advanced boosting, variable compression ratio and related improved aftertreatment systems. Moreover, relevant concept is constituted by combustion pre-chamber coupled with lean burn operation [66,67].

NG chemical composition variations will be accounted for by suitable on board sensors which will allow to adjust ignition timing, injection strategy and boost pressure. In Figure 66 a schematic of advanced CNG technology is shown[66].

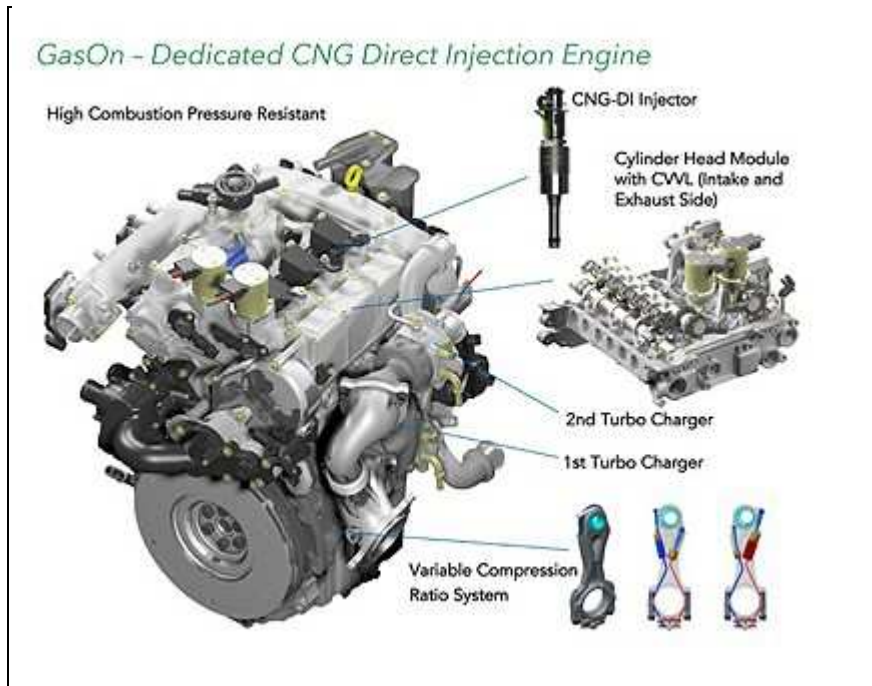


Figure 66. GasOn DI CNG engine illustration[66]

NG engine computational studies will hold on advanced combustion models based as previously discussed on the fractal geometry approach; NG direct injection will be developed in numerical analysis by adding to the presented model the NG contribution in terms of gaseous fluid flows during the injection, which will affect the turbulence zero-dimensional model[68].

All technologies improvements about natural gas adoption will set a path to a potential transformation of passenger cars, truck and buses transportation[69], even from an economic and societal standpoint.

## 7. Bibliography

---

- [1]-- <http://www.iveco.com/ivecobus/it-it/prodotti/pages/iveco-bus-cng.aspx>
- [2]--[http://www.mit.gov.it/mit/site.php?p=normativa&o=vd&id=1&id\\_dett=49](http://www.mit.gov.it/mit/site.php?p=normativa&o=vd&id=1&id_dett=49)  
Art.47 Codice della Strada
- [3]-- <http://acea.be/automobile-industry/buses>
- [4]-- Civitas,"Smart choices for cities- Clean buses for your city",Policy Note,2013, pdf.
- [5]-- European Union Road Federation,"Road Statistics Yearbook 2016",2016,pdf.
- [6]-- ACEA,"Buses",Fact Sheet, 2017, pdf.
- [7]-- NGVA Europe,"Vehicle catalogue June 2016",2016,pdf.
- [8]-- 49 Code of Federal Regulation, US Law, Ch.V(10-1-13 Edition) Part 523-  
Vehicle Classification
- [9]--<http://www.npc.org/reports/FTF-report-080112/>  
Chapter 3-Heavy-Duty Vehicles.pdf
- [10]--D.Giacosa,"Motori endotermici",Hoepli, 2000
- [11]--J.B.Heywood,"Internal Combustion Engine Fundamentals",Indian Edition,  
McGraw Hill Education, 2011
- [12]--G.Wright,"Fundamentals of Medium/Heavy Duty Diesel Engines",Jones  
&Bartlett Publishers, 2015
- [13]--<http://www.np.co.tt/our-brands/cng/>
- [14]-- Holmberg, Andersson, Nylund, Mäkelä, Erdemir," Global energy consumption  
due to friction in trucks and buses", Tribology International 78(2014),94-114
- [15]-- Duffy,Wright,"Fundamentals of Medium/Heavy-Duty Commercial Vehicle  
Systems",Jones&Bartlett Learning,2015
- [16] -- Grigoratos, Fontaras, Martini, Peletto, "A study of regulated and green house  
gas emissions from a prototype heavy-duty compressed natural gas engine  
under transient and real life conditions", Energy 103 (2016), 340-355
- [17]-- Semin, Ismail, Bakar,"Diesel Engine Convert to Port Injection CNG Engine  
Using Gaseous Injector Nozzle Multi Holes Geometries Improvement: A  
Review", American J. of Engineering and Applied Sciences 2 (2): 268-278,  
2009
- [18]--<http://www.ucsusa.org/clean-energy/coal-and-other-fossil-fuels>
- [19]-- <https://www.uniongas.com/about-us/about-natural-gas>
- [20]-- Gallagher,"Natural Gas Measurement Handbook", Elsevier, 2013
- [21]-- <http://www.metauto.it/i-serbatoi-per-veicoli-a-cng-aspetti-operativi>

- [22] -- Beroun, Martins, "The Development of Gas (CNG, LPG and H<sub>2</sub>) Engines for Buses and Trucks and their Emission and Cycle Variability Characteristics ", SAE Technical Paper Series, 2001- 01-0144
- [23]-- Sher, "Handbook of Air Pollution from Internal Combustion Engines: Pollutant Formation and Control" , Academic Press, 1998
- [24]-- <https://www.afdc.energy.gov/fuels/prices.html>
- [25]-- Bakar, Kadirgama, Rahman, Sharma, Semin "Application of Natural Gas for Internal Combustion Engines, Advances in Natural Gas Technology", Ed.Al-Megren, 2012
- [26]-- [https://www.dieselnet.com/tech/air\\_vva.php](https://www.dieselnet.com/tech/air_vva.php)
- [27] -- J.Törmänen, "Variable Valve Actuation and Dual-Fuel Combustion", Master's Thesis, Aalto University School of Engineering, 2015
- [28]-- M.Haas, "Uniair -The first fully-variable electro-hydraulic valve control system", Schaeffler Symposium 2010
- [29]--D.K.Srivastava, A.K.Agarwal,A.Datta, R.K.Maurya," Advances in Internal Combustion Engine Research", Springer, 2017
- [30]--"Encyclopedia of Automotive Engineering- Engines: fundamentals", Wiley & Sons , 2015
- [31]-- Ferrari, "Motori a Combustione Interna", Il Capitello,2008
- [32]--Baratta, Finesso, Misul, Spessa, Tong, Peletto," Potential of the Variable Valve Actuation (VVA) Strategy on a Heavy Duty CNG Engine" , Proceeding of the 12th Biennial Conference on Engineering Systems Design and Analysis, 2014
- [33]--Baratta, Finesso, Misul, Spessa, Tong, Peletto,"Optimization of a User-Defined Fractal Combustion Model and its Application to the Assessment of the Behaviour of a Heavy-Duty NG Engine Equipped with VVA under Steady-State and Transient Conditions", International Journal of Mechanics and Control, Vol.18, No.01, 2017
- [34]-- Musculus, "Direct-Injection CNG Combustion Research in a Heavy Duty Optical Engine", Sandia National Laboratories,USA, Natural Gas Vehicle Technology Forum, 2015 Meeting
- [35]--Santini,""FPT Natural Gas Engines. The way to high performances and low emissions",5th NGVA Europe International Show & Workshops, 2014
- [36]-- [www.gdtech.eu/en/2016/10/17](http://www.gdtech.eu/en/2016/10/17)
- [37]--<https://www.autobusweb.com>
- [38]--Pielecha, Bueschke,Cieślik, Skowron,"Turbulent spark-jet ignition in SI gas fuelled engine",MATEC Web of Conferences,118 00010(2017)

- [39]-- Dunn, "Optimised Natural Gas Engines for Phase II GHG Compliance", Westport, 2016
- [40]-- <https://www.arb.ca.gov/regact/cng-lpg/appd.pdf>
- [41]--Parks,"Emissions Control for Natural Gas Fueled Trucks",Natural Gas Workshop at NREL,2017
- [42]-- Fortunato, Gotta, Caroca, Russo ,Fino,Saracco, Specchia,"Catalytic Converter for CNG-engines aftertreatment",Politecnico di Torino,2007
- [43]--Nevalainen, Kinnunen, Kirveslahti, Kallinen, Maunula, Keenan, Suvanto, "Formation of NH<sub>3</sub> and N<sub>2</sub>O in a modern natural gas three-way catalyst designed for heavy-duty vehicles:the effects of simulated exhaust-gas composition and ageing", Applied Catalysis A,General 552(2018) 30-37
- [44]--Amin, Abedi, Hayes, Votsmeier, Epling,"Methane oxidation hysteresis over Pt/Al<sub>2</sub>O<sub>3</sub>", Applied Catalysis A: General 478 (2014)91-97
- [45]-- <http://www.firmgreen.com/pdf/cng101.pdf>
- [46]--<http://www.automotive-technology.co.uk/?p=1344>
- [47]--A.K.Oppenheim," Combustion in Piston Engines: Technology, Evolution, Diagnosis and Control", Springer Science & Business Media,2013
- [48]-- G.Zakis," Alternative Ignition Systems for CNG in Diesel Applications", Master of Engineering Science Thesis, University of Melbourne,2003
- [49]--V.Sharma," Laser Spark Ignition in lean burn CNG engine",IOSR, Journal of Mechanical and Civil Engineering, Vol X, Issue X, Ver I, (Jan.2014)
- [50]-- [www.fptindustrial.com/global/it/motori/on-road/bus/cursor8-ng](http://www.fptindustrial.com/global/it/motori/on-road/bus/cursor8-ng)
- [51]--<http://www.reactiondesign.com/news/40/95>
- [52]--<http://ilin.asee.org/Conference2009/FinalPapers/Paper1A2.pdf>
- [53]--Gamma Technologies (2012), GT-Power V7.3 User's Manual and Tutorial
- [54]--Baratta, Spessa,"Numerical Simulation Techniques for the Prediction of Fluid-Dynamics, Combustion and Performance in IC Engines Fuelled by CNG", Book Chapter, InTech
- [55]-- GT-Power v7.3Navigator Guida GT-ISE Help
- [56]-- Baratta, Catania, Spessa, Vassallo," Development and Assessment of a Multizone Combustion Simulation Code for SI Engines Based on a Novel Fractal Model", SAE Technical Paper Series, 2006-01-0048
- [57]--Baratta, Catania, Spessa, Vassallo, "Flame Propagation Speed in SI Engines: Modeling and Experimental Assessment", Proceeding of the ASME 2005 Internal Combustion Engine Division Fall Technical Conference, ICEF2005

- [58]-- Baratta, Catania, d'Ambrosio, Spessa, "Prediction of Combustion Parameters, Performance, and Emissions in Compressed Natural Gas and Gasoline SI Engines", Journal of Engineering for Gas Turbines and Power, 062805-1, November 2008, Vol.130
- [59]--De Bellis, Severi, Fontanesi, Bozza, "Hierarchical 1D/3D approach for the development of a turbulent combustion model applied to a VVA turbocharged engine. Part II: combustion model ", Energy Procedia 45(2014), 1027-1036
- [60]--Shi, Wen Ge, Reitz "Computational Optimization of Internal Combustion Engine", Springer-Verlag, 2011
- [61]-- "Matlab Documentation", Matlab R2017a Software, Mathworks
- [62]-- CORE- Project Final Report, <http://co2re.eu>
- [63]-- ChE-400, Reactive Process Engineering, pdf
- [64]--Shu, Fu, Liu, Zhang, Zhao,"Experimental and computational study on the effects of injection timing on thermodynamics, combustion and emission characteristics of a natural gas (NG)-diesel dual fuel engine at low speed and low load", Energy Conversion and Management 160 (2018) 426-438
- [65]-- Zhang, Xu, Li, Shao,"Combustion and emissions of a EURO VI heavy-duty natural gas engine using EGR and TWC", Journal of Natural Gas Science and Engineering 28 (2016), 660-671
- [66]-- <http://www.europeanenergyinnovation.eu/Latest-Research/Autumn-2017>
- [67]-- <http://www.gason.eu/page/index/project>
- [68]-- L.Casale,"Sviluppo di un modello dedicato per motore ad iniezione diretta di gas naturale per la simulazione del processo di combustione", Tesi di Laurea Magistrale, Politecnico di Torino, 2017
- [69]-- [https://cordis.europa.eu/result/rcn/198142\\_en.html](https://cordis.europa.eu/result/rcn/198142_en.html)